ADVANCED INSTRUMENTED STAMPS FOR MICRO TRANSFER PRINTING AND NOVEL APPLICATIONS AREAS

BY

NUMAIR AHMED

DISSERTATION

Submitted in partial fulfilment of the requirements
for the degree of Doctor of Philosophy in Mechanical Engineering
In the Graduate College of the
University of Illinois at Urbana-Champaign, 2015

Urbana, Illinois

Doctoral Committee:

Professor Placid M. Ferreira, Chair, Director of Research
Professor John A. Rogers
Professor Shiv G. Kapoor
Assistant Professor Seok Kim

ABSTRACT

Transfer printing refers to a set of techniques for deterministic assembly of functional micro/nano scale devices into two and three dimensional spatial arrangements. It provides a versatile route for realizing multifunctional heterogeneously integrated systems such as flexible electronics, biocompatible sensing and therapeutic devices, transparent and curved optoelectronic systems etc. Micro-transfer printing is an automated process that implements deterministic micro scale assembly using a molded viscoelastic stamp typically made out of PDMS. The process relies upon the control of adhesion and fracture at the interfaces between the stamp and the devices being assembled to pick up and release them. A widely exploited strategy to achieve variable adhesion from the stamp is to use the rate dependent effects of the viscoelastic stamp material. It is a very versatile process and has been used in the realization of many novel heterogeneously integrated systems. The process has been implemented industrially to assemble ultra-high concentration photovoltaic panels. This body of work presents the development of new stamp technologies to address the challenges associated with increasing parallelism and shortcomings associated with fixed geometry stamps. Starting from the concept of an active composite material with distributed sensing, actuation and compliance tuning, new stamp architectures are developed. These novel stamps replace the compliance of a bulk PDMS stamp with active functional structures with tunable stiffness; without effecting the ability of the stamps to be used for transfer printing. The new stamp architecture enables active monitoring and control of the micro transfer printing process. Using instrumentation to sense deflections/forces at each post allows detection, measurement and compensation of misalignments between the stamp and donor/receiving substrates. Furthermore this information is used to detect pick up and printing errors at individual

posts, allowing for error handling to increase process robustness. Moreover the ability to selectively actuate allows to engage/disengage individual posts. This enables new transfer printing modes such as collect and place. Finally results of pilot experiments conducted to test the feasibility of using micro transfer printing in novel application areas are presented.

To all my loved ones

ACKNOWLEDGEMENT

No words can ever describe my gratitude towards everyone who has supported and encouraged me throughout my years of study. I am deeply indebted to my advisor, Professor Placid M. Ferreira, for his unwavering support, supervision and guidance. His patience, dedication knowledge, curiosity and creativity made my graduate studies at University of Illinois extremely rewarding and memorable. I am also indebted to Dr. Glennys A. Mensing for all her support, encouragement and ever availability to discuss many research and micro fabrication related problems and for their solutions.

It has been a great student experience for me at UIUC; made possible by all the people I had the pleasure of knowing and working with. I would like to extend special thanks to many members of Ferreira research group and Rogers research group. I would like to thank Kyle Jacobs, Paulius Elvikis, Alaa Al-okaily, Bonjin Koo, Jorge Correa, Bruno Azeredo, Shama Barna, Nick Tombs, Miki Takagi, Nishana Ismail, Dr. Keng Hsu, Dr. Johnson Samuels, Dr. Andrew Carlson, Dr. Tae-Il Kim, Dr. Sang Yoon Yang, Dr. Canan Dagdeviren, Dr. Hyun-joong Chung and Dr. Seok Kim for their friendship, cooperation, motivation and support.

I must thank all the staff at the Mechanical Science and Engineering Micro-Nano-Mechanical Systems cleanroom and the Frederick Seitz Materials Research Laboratory cleanroom, without their tireless support for the facilities, none of my work would have been possible. I would like to specially thank Dr. Edward Chainani for his support. I must also thank Kathryn A. Smith, Ruthie Lubkeman and Laurie Macadam for their help and cooperation.

I would like to acknowledge the support of the local Muslim community and especially the Central Illinois Mosque and Islamic Center. It would like to acknowledge the financial support I

received from the National Science Foundation while being a part of the Nano-CEMMS center at UIUC.

Last but not least I would like to thank my friends and family for their support during the course of my graduate studies. I am forever grateful to my parents Imtiaz Ahmed and Asima Imtiaz, without their sacrifice and support none of this would have been possible. They have always been a source of inspiration, love and encouragement for me. My brother Haris Ahmed has been my counsel and support during this whole time. I would also like to thank my now wife; Sahar Ansar, for being my rock. She has been a source of comfort and love, and has been by my side during the course of my graduate studies.

While I have tried my best to acknowledge the support and favors of the people who have been a part of this journey, I present my sincere apologies to those whom I may have missed.

At the end I would like to humbly acknowledge all the favors Allah (God) has bestowed upon me. I thank him for the opportunity to pursue graduate studies at an institution as prestigious as UIUC and blessing me with great company. I do not have the words, nor do I even know how to thank him for all his blessings that I had never imagined, nor deserved. Indeed he is the one, the most benevolent and most merciful.

Table of Contents

LIST OF SYMBOLS

G	Energy release rate
$\Delta \boldsymbol{R_s}$	Change in resistance of the sensing element
$\boldsymbol{\varepsilon}$	The induced strain
$\boldsymbol{G}$	The gauge factor
$\boldsymbol{R_s}$	The nominal resistance of the sensing element under no strain
$\boldsymbol{V_o}$	Measured output voltage from the Wheatstone bridge
$\boldsymbol{A}$	The amplification factor of the instrumentation amplifier
$\boldsymbol{R}$	The resistance of the Wheatstone bridge resistors
$\boldsymbol{V_e}$	Bridge excitation voltage
$\boldsymbol{F}$	Force applied to the post
$\boldsymbol{S}$	Sensitivity of the sensor
X	The delamination force signal obtained during an event
ω_i	The class representing an events where the interface fails.
M_i	Mean of Gaussian distribution
σ_i	Standard deviation of Gaussian distribution

$N(M_i, \sigma_i)$	Gaussian distribution
$P(\omega_i / X)$	The a posteriori probabilities of the signal X implying that an event belonging to class ω_i has occurred.
$P(\omega_i)$	The a priori probabilities of an event occurring
V_m	Measured voltage output from the strain sensor of the active composite stamp
V_d	Driving voltage for actuating the post of the active composite stamp
d	Deflection of the post of the active composite stamp
d_m	Measured deflection of the post of the active composite stamp
d_{ij}	Piezoelectric coefficient
E_3	Applied electric field
Δ	Geometric constant
$\boldsymbol{Y_i}$	Young's modulus
$\boldsymbol{h_i}$	Layer thickness
r	Reference input to the control system
e	Error between reference and actual value
X_m	Measured deflection of the post
V_c	Output voltage from the control system

$\boldsymbol{G(s)}$	Plant transfer function
K_p	Proportional gain
K_i	Integral gain
$\boldsymbol{T_s}$	Sampling time
T_g	Glass transition temperature

CHAPTER 1: INTRODUCTION

Reliable manufacturability of complex heterogeneous microsystems is a big challenge. Though conventional surface micromachining has proven successful for simple and monolithic micro-devices, it is not sufficient to address the manufacturing of today's wide range of microsystem designs. To address these challenges micro-assembly has emerged as an alternative and enabling technology which can allow the building of complex systems by assembling simpler heterogeneous micro-parts [1].This chapter gives a brief literature review of the field of micro-assembly, special focus is given to a subset of micro assembly; the micro transfer printing process. Micro-assembly systems can be broadly divided into two classes based on their principle of operation; 1) Serial assembly and 2) Parallel assembly [2].

1.1 Serial micro-assembly

Serial micro-assembly follows the traditional pick and place technique to assemble objects one part at a time. Typically each part to be assembled is sequentially picked up from a known location, manipulated and then placed into its final position. Serial micro assembly systems consist of three main elements; a part handling tool, a high precision positioning system and sensory feedback (vision feedback is used in most cases). The throughput of serial micro-assembly is determined by the number of micro manipulators used and the bandwidth of the individual tool and is generally smaller compared to its parallel counterpart. One advantage of serial micro-assembly is the ability to orient parts in N degrees of freedom; allowing creation of more complex parts compared with parallel micro-assembly.

Serial micro-assembly systems can be further sub divided into the following sub types:

1.1.1 Tele-operated or master-slave systems

This is the most basic micro-assembly system. It allows semi-automatic or manual control with or without haptic feedback, to perform micro-structure assembly. Commands from the operator are read and applied to the system. Platforms are composed of a macro-side; the master which interfaces with the operator, and a micro-side slave; which operates in the assembly environment [3]. The system architecture consists of an end effector such as a micro-gripper or a probe, motion stages and visual feedback system [4, 5].

1.1.2 Automated micro-assembly Systems

In cases of high volume manufacture of micro products fully automatic assembly is often the preferred option. In order to achieve a certain level of automation in serial assembly, typically visual feedback is used to track the position of end effector relative to the parts.

A vision based system to perform automated grasping of micro parts in two dimensions has been demonstrated by Len *et al.* [6, 7] . A three dimensional micro-assembly system using vision feedback with sub-micron accuracy has been demonstrated by Wang *et al.* [8]. The use of force feedback to perform micro-assembly has also been demonstrated by Thompson *et al.* and Lu *et al.* [9, 10]. A flexible micro-assembly system that combines vision and force feedback for assembly of MEMS sensors has been demonstrated by Xie *et al.* [11].

There is a large body of work available related to micro-assembly tasks using micro-grasping techniques and strategies [12, 13, 14, 15, 16, 17].

1.2 Parallel micro-assembly

As stated above, serial assembly allows for the creation of complex microstructures at the expense of throughput; using serial production. However some applications require high throughput rates where the individual objects have low complexity, and this is where parallel assembly with limited object manipulation ability can be used. Parallel micro-assembly can be broadly divided into the following two classes namely; deterministic and stochastic parallel assembly.

1.2.1 Deterministic parallel micro-assembly

Deterministic parallel micro-assembly refers to the direct assembly of microstructures from a donor substrate to a target substrate. The positioning of the individual microstructures is determined by their layout on the donor substrate.

A deterministic parallel micro-assembly process using sacrificial layer etching and flip chip bonding has been demonstrated by Singh *et al.* [18]. The transfer is achieved by cold welding electroplated indium solder bumps to electroplated copper pads. Harsh *et al.* [19] have also demonstrated the use of flip-chip bonding to assemble Silicon based RF MEMS. They use post assembly release of the structures, which avoids the use of tethers [18] and thus results in better RF performance.

Lin *et al.* [20] have demonstrated three-dimensional parallel micro-assembly of solder balls. The solder balls are first self-assembled into a ball trap using shape matching. After the balls are held in the traps, a PDMS film is brought into contact with the balls; attaching the balls onto the PDMS. A UV curable adhesive is them applied to the bottom of the balls; which are then

aligned and assembled onto the target substrate. After assembly the UV adhesive is cured securing the solder balls in place. The process is then repeated to get three dimensionally assembled layers of solder balls by successive assembly.

Another three dimensionally assembled micro structure has been demonstrated by Chu *et al.* [21]. They have demonstrated the fabrication of micro coils using parallel micro-assembly. An array of micro-grippers- with the aid of vision based algorithm- is used to grasp and assemble micro coil windings into specially designed slots. The use of multiple grippers allows for the parallel assembly of multiple coils at the same time thus improving throughput.

1.2.2 Stochastic parallel micro-assembly

Stochastic parallel micro-assembly also referred to as self-assembly - in the meso or macroscopic scales - uses different type of forces such as electrostatic, magnetic, surface tension; vibration etc. to agitate specially shaped parts into known locations [22]. Using magnetic fields, thin chips have been assembled onto a UV curable polymer to demonstrate semiconductor packaging using self-assembly [23, 24]. Self-assembly of multiple classes of materials (dielectrics, metals, semiconductors etc.) with varying length scales using DC electric fields has recently been demonstrated with high yields (97%) [25]. Microfabricated single crystal silicon devices have been assembled onto a flexible polymer substrate [26] and silicon micro-mirrors have been attached to prefabricated micro-actuators [27] with the help of capillary forces through fluidic based self-assembly. In both cases specially shaped traps are used to first capture the devices being attached. Afterwards the system is heated to melt an adhesive material pre-patterned in the traps to bond the device to the final assembly location.

1.3 Micro transfer printing

Transfer printing refers to a set of techniques for deterministic assembly of ‘inks’ - functional micro/nano scale devices from a diverse class of materials and having a wide range of geometries and configurations - into two and three dimensional spatial arrangements. It provides a versatile route for realizing multifunctional heterogeneously integrated systems such as flexible electronics, biocompatible sensing and therapeutic devices, transparent and curved optoelectronic systems etc. Transfer printing can be divided into three distinct categories [28]:

- *Additive Transfer:* Utilizes stamps that have been ‘inked’ with the material of interest using various deposition techniques such as spin coating, vapor deposition etc.

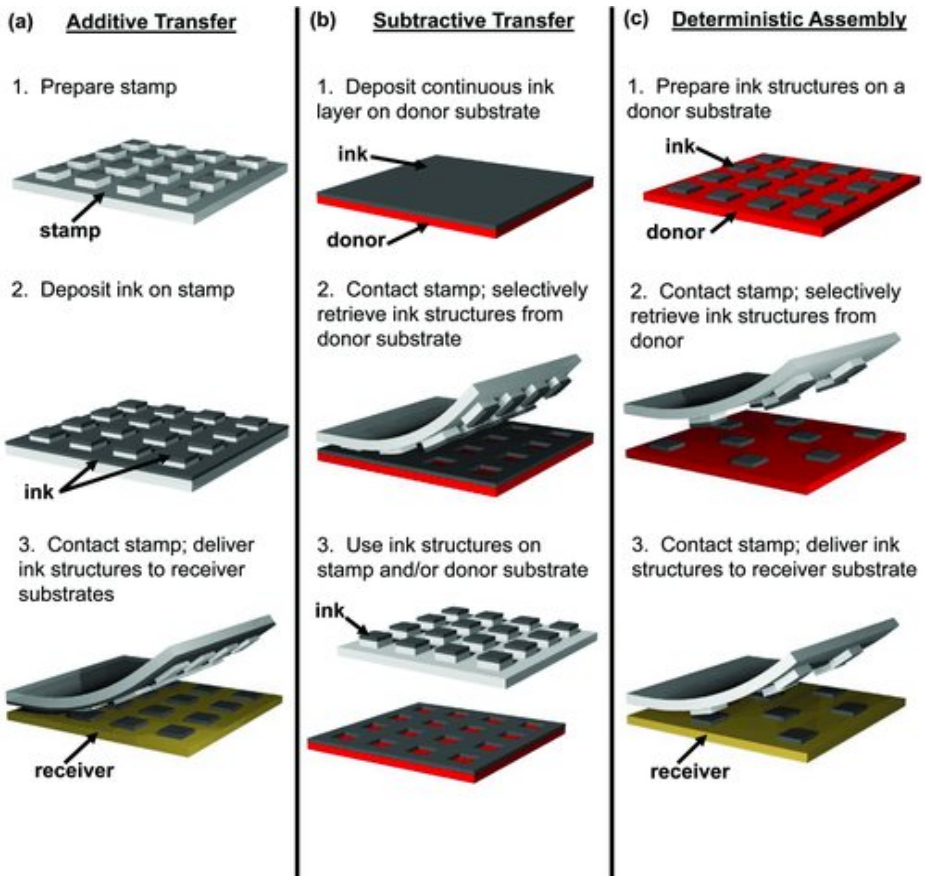

Figure 1: Schematic illustration of the three different types of transfer printing. Taken from [28]

- *Subtractive Transfer:* Selectively removes material using a patterned stamp through contact with a continuous film.
- *Deterministic Assembly:* Uses a patterned stamp to retrieve prefabricated micro structures from donor substrates and deposit them onto receiving substrates.

These three categories are shown schematically in figure 1**.**

Micro-transfer printing is a standalone automated process that implements *deterministic parallel assembly* using a molded PDMS stamp. The stamp is patterned with posts which locally make contact with the functional microstructures on the donor and acceptor substrates. The use of PDMS as the stamp material and the molding process creates a very versatile and low cost process. Since PDMS is transparent to visible light, PDMS based stamps allow visual feedback, ease of

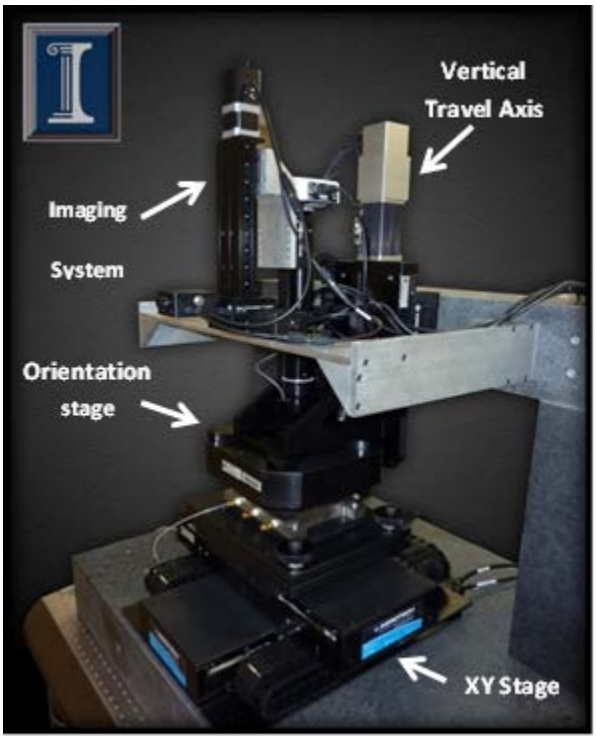

Figure 2: Automated Transfer Printing Machine, showing the four motion axes and integrated optics.

alignment and process monitoring. The PDMS can be molded with multiple posts to permit parallel assembly of multiple microstructures. Figure 2 shows an automated micro-transfer printing machine developed at the University of Illinois [29]. The major components of the system include (a) a CNC XY-stage for positioning, (b) a Z-stage for mounting and moving the stamp up and down and controlling the separation speed and force, (c) an orientation/rotation stage that assists in obtaining parallel alignment between stamp and the donor and receiving substrates and (d) imaging system that is used for alignment and monitoring of the printing process.

It is a very versatile process and has been used in the realization of many novel heterogeneously integrated systems [30, 31, 32, 33, 34, 35]. The process has been implemented industrially [32, 36] to assemble ultra-high concentration photovoltaic panels.

1.3.1 Micro transfer printing mechanism

Stamps used for ink manipulation in micro transfer printing are usually composed of a viscoelastic material. One salient feature of viscoelastic materials is that their interface adhesion strength depends upon the speed at which the interface broken. The transfer in micro transfer printing relies upon the control of adhesion and fracture at the interfaces between ink/donor, ink/stamp and ink/receiver. As the stamp makes contact with the Ink, two interfaces are formed; one between ink and the stamp and the other between the ink and the substrate, as depicted in figure 3. The ink retrieval and release process can be modeled as the initiation and propagation of

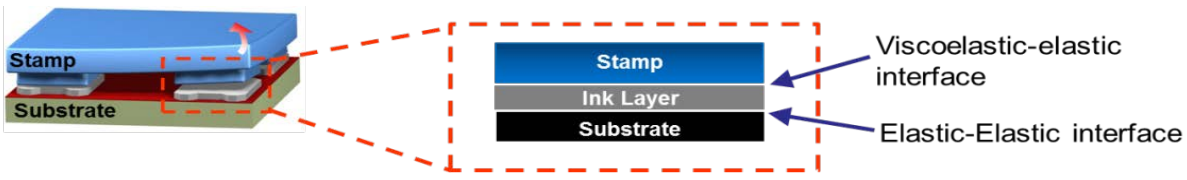

Figure 3: Schematic depiction of the different interfaces formed during ink retrieval. The same scheme exists for ink release

interfacial cracks [37] based on a characteristic energy release rate G. Transfer printing exploits the rate dependent effects of the viscoelastic stamp material; typically PDMS [28, 38]. Ink retrieval takes place when the adhesion energy at the ink/stamp interface $G^{stamp/ink}$ becomes greater than the ink/substrate interface $G^{ink/substrate}$ at the delamination velocity; conversely ink release takes place when the adhesion between the ink/receiver interface $G^{ink/substrate}$ becomes greater than the ink/stamp interface $G^{stamp/ink}$ at the delamination velocity. The process mechanics are shown schematically in figure 4.

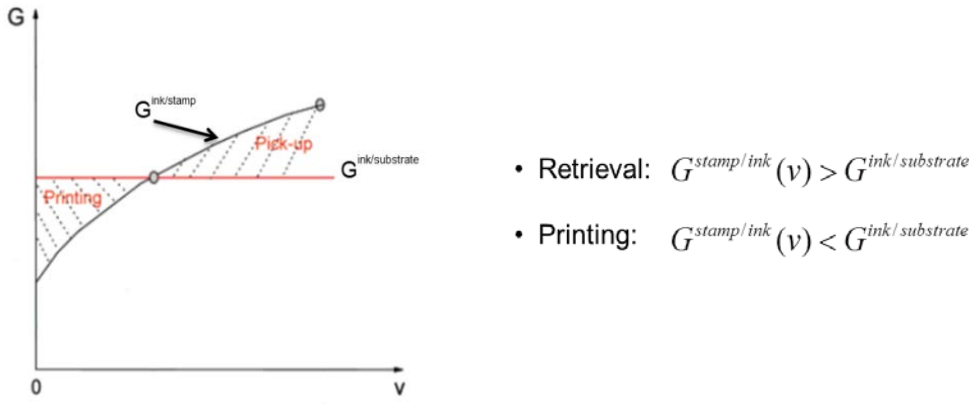

Figure 4: Schematic representation of variation of adhesion energy of a transfer printing stamp as a function of delamination velocity.

1.3.2 Recent developments in micro transfer printing

Besides the kinetically-assisted [39] approach to transfer printing that relies on accurate control of separation velocity to controllably induce failure at the stamp/ink interface, Kim et al [40] use patterning and relieving of the stamp surface to engineer collapse and recovery of relief features on the stamp. This changes the contact area of the stamp-ink interface; modulating the force required for its failure from high to low, to enable ink pick up and printing onto low adhesion surfaces and without the presence of any adhesive materials. Figure 5 shows a SEM image of a representative stamp. A theoretical model for these stamps has been developed by Wu *et al.* [41]

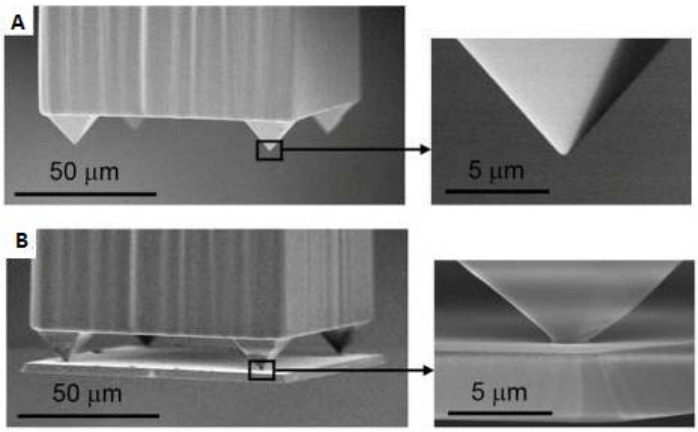

Figure 5**:** (A) SEM image of a representative transfer printing stamp with micro tips. (B) Stamp with an attached silicon platelet. Images take from [40].

In contrast to controlling the stamp area by molding the stamp surface, Carlson et al [42] have introduced the idea of using pneumatically actuated stamp to achieve both, preferential failure of the stamp-ink interface (by introducing additional bending and shear when the stamp is pneumatically pressurized) and programmability to selectively print at different sites or posts on the stamp. Figure 6 shows the image of a single pneumatically actuated stamp taken from [42].

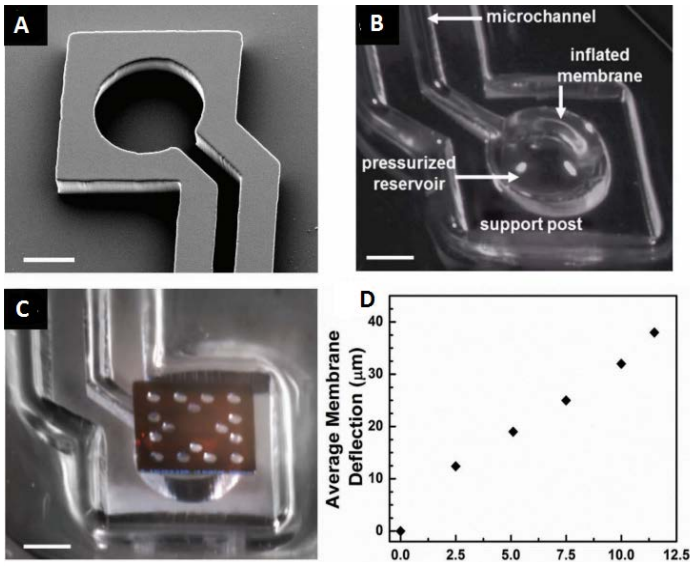

Figure 6: SEM images of the pneumatically actuated stamp. (A) Image of the stamp without the top PDMS membrane showing the micro channel. (B) Optical image of the stamp without and (C) with a silicon plate on the inflated membrane. (D) Average deflection of the membrane.

Besides the use of PDMS as the stamp material, Eisenhaure *et al.* [43] have demonstrated the use of shape memory polymer as the stamp material for transfer printing.

Along with the development of stamp technology, recent developments have also been made in the processing technique. Carlson et al [44] have developed the idea of introducing shear during the printing step to cause preferential failure of the stamp-ink interface during printing. This allows reducing the force required to break the stamp/ink interface. Figure 7 shows the effect of shear on the reduction in the pull-off force measured experimentally taken from [44].

Another recent process development has been demonstrated by Saeidpourazar et al [45]. They have introduced a new release mechanism where laser heating is used to generate a thermal mismatch strain at the stamp-ink interface that leads to delamination and printing of the ink. The new process is named laser-micro transfer printing. The salient feature of this process is non-contact device release. This allows for printing onto low adhesion surfaces. The process has been

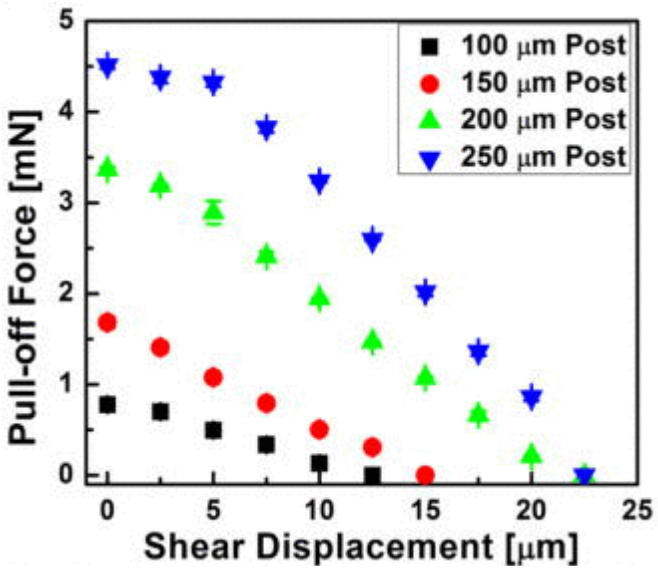

Figure 7: Experimentally measured pull-off force required to delaminate the stamp from a flat silicon substrate as a function of shear displacement taken from [44]

modeled by Rui *et al.* [46, 47]. The process has been extensively characterized using multiphysics modeling supported by experimental results and further developed by Alaa *et al.* [48, 49].

1.4 Overview and organization of work

This thesis describes a set of advanced stamp technologies based on a novel active composite material that enables the development of new transfer printing protocols and improve process robustness. The active composite affords the integration of distributed actuation, sensing and stiffness tuning; allowing the creation of stamps that can sense force, contact and actively modulate their geometry. We start by addressing the efficacy of using sensing and actuation within the transfer printing process. We address the simpler problem of adding sensing into the stamp first by conducting a pilot study to gauge the feasibility of such a system. After successfully demonstrating the feasibility of using sensing within transfer printing the thesis then addresses the creation of more precise stamps using micro fabrication. Next the use of sensing to perform transfer printing and detect process errors is demonstrated. After the integration of sensing into the stamp, actuation capabilities are integrated, a single architecture capable of providing multi actuation modes is presented. After design, fabrication and characterization of the stamps new modes of transfer printing are presented. We end by conducting pilot experiments to study the use of transfer printing in new application areas.

Chapter 2 describes the opportunities that exist for micro transfer printing stamps with regards to detecting and measuring process errors and modulating stamp geometry. The general architecture of the active composite material is introduced that allows for the integration of distributed sensing and actuation into a single bulk material. Finally the active composite is specialized into a transfer printing stamp.

Chapter 3 presents the integration of sensing into the stamp. First the pilot study conducted to gauge the feasibility of integrating sensing into the micro transfer printing process is described and its results presented. After proving feasibility a more precise stamp architecture is presented and the fabrication process developed. After fabrication, stamp testing and characterization is described. Finally the stamp integration into the transfer printing process is presented along with demonstration of new printing modes based on event and contact detection, error detection using measurement of interaction forces is shown.

Chapter 4 presents the extension of the functional integration by developing a micro transfer printing stamp based on the active composite material architecture that allows for the distributed integration of sensing, actuation and compliance tuning. FEA based design of the stamp is presented followed by the development of a facile fabrication process. Following fabrication and system integration, the newly developed stamps are characterized and calibration is performed. Using the added actuation functionality novel collect and place based transfer printing is demonstrated. Finally a dynamical model of the system is developed and using the model a closed loop control system in developed. The closed loop control is implemented and system performance is measured experimentally.

Chapter 5 presents the results of a second mode that exists in the active composite stamps, namely thermo-mechanical actuation and piezoelectric sensing. FEA based simulation is used to calculate the actuation magnitude. System characterization based on PZT based sensing and thermo-mechanical actuation is performed. Using frequency domain system identification techniques a dynamical model of the system is developed. Closed loop position control is

implemented and system performance is experimentally measured. Using the integrated functionality collect and place printing including selective device retrieval is demonstrated.

Chapter 6 presents results of pilot experiments conducted to assess the application of transfer printing in new application areas. Using laser based localized heating a process of three dimensional assembly of silicon on polymers is presented. Experiments are conducted to demonstrate the use of transfer printing to assemble thin silicon dies as a primer for three dimensional integrated circuit integration.

CHAPTER 2: ADVANCING STAMP TECHNOLOGY

Micro transfer printing stamps are typically made from viscoelastic materials. One of the most commonly used material is poly(dimethylsiloxane) (PDMS). PDMS lends itself well for a stamp material because it is chemically and thermally stable, has good optical transparency (down to ~230 nm), is chemically inert, has low modulus (ranging from ~1 – 10 MPa) and low surface energy (21.6×10^{-3} Jm^{-2}).

A typical PDMS bulk stamp fabrication follows well established micro-molding and curing protocols. The fabrication process begins by creating a master mold with relief features using photolithography and surface micromachining. The mold goes through a surface treatment process by which a thin anti stiction coating such as a flouroalkyl trichlorosilane or polytetraflouroethylene (PTFE) is deposited. Liquid pre polymer is then poured onto the mold surface and allowed to cure.

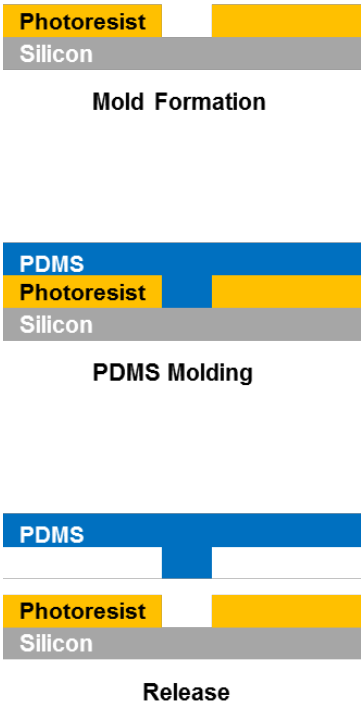

Figure 8: Schematic of a PDMS bulk stamp fabrication process

After being fully cured the PDMS is carefully demolded from the master mold. A simplified schematic of the process is shown figure 8.

One of the most attractive features of this process is its simplicity. However, where the bulk stamps are easy and quick to manufacture, this is also an area where most of the opportunity lies. Being able to add novel functionality such a sensing and actuation into the stamp can create interesting routes to monitor and control the micro transfer printing process using the most critical part of the whole process; the stamp itself.

2.1 Addressing opportunities for adding functionality

Looking at some of the typical sources of errors encountered during the micro transfer printing process such as during device retrieval, failure is caused by a device that has been completely released and thus is missing, or a device has not been properly released and thus cannot be picked up. Errors introduced by the setup process or by the stamp include angular misalignment

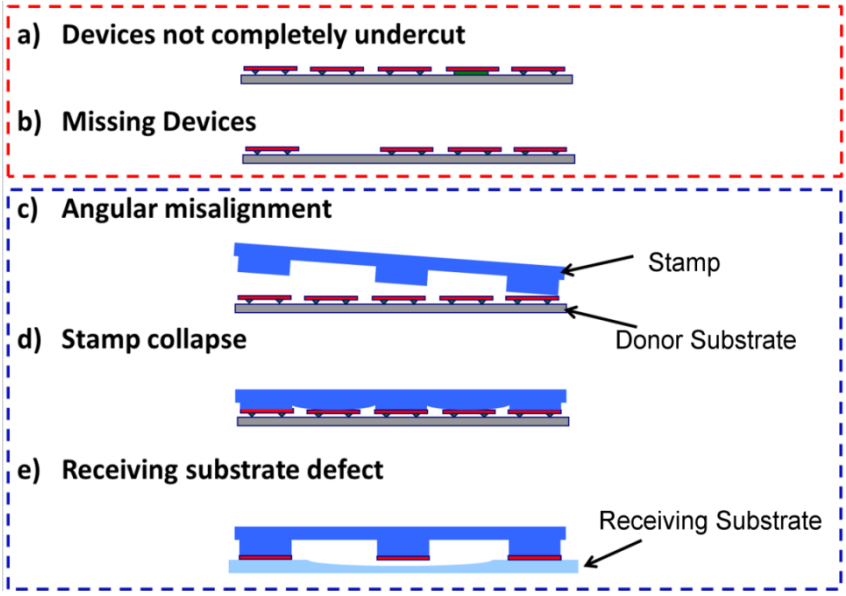

Figure 9: Schematic of some typical sources of errors encountered during the micro transfer printing process

in which the stamp is not perfectly parallel to the substrate and thus all areas of the stamp will not make contact with the substrate uniformly. Another source of error is stamp collapse in which the whole stamp ends up touching the substrate, this causes erroneous pickup of devices when it occurs on the donor thus depleting the donor quickly, it is especially a cause for concern when large area printing is required using stamps with a large pitch between post [50, 51]. On the device release side of things errors in the substrate such as waviness or bowing and foreign debris such as dust can cause failure to release devices. The above mentioned typical sources of errors are shown schematically in figure 9. Being able to sense when some of these errors occur can be advantageous to improve overall robustness of the process. This leads to the idea of adding sensing functionality into the stamp at the scale of individual posts where stamp/substrate interactions can be measured and meaningful inferences can be drawn.

Bulk stamps used for micro transfer printing have a fixed geometry of the posts, thus the pickup and printing geometry is dictated by the geometry of the stamp. This means that devices can be printed in only one pattern, whenever a new geometry is needed, a new stamp will need to be created to match the desired geometry. Also, since the stamp makes contact with the substrate uniformly, it limits the process to retrieve devices from a single substrate. The operation of a fixed geometry stamp is shown schematically in figure 10.

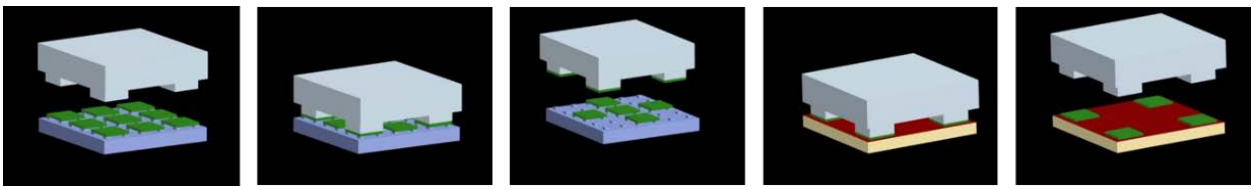

Figure 10: Schematic representation of micro transfer printing using a fixed geometry bulk stamp. The printing pattern is dictated by the stamp geometry, pickup is limited to a single substrate. (left to right) Alignment with the donor wafer, contact with the devices, device retrieval, alignment and contact with acceptor substrate, release of devices onto acceptor substrate.

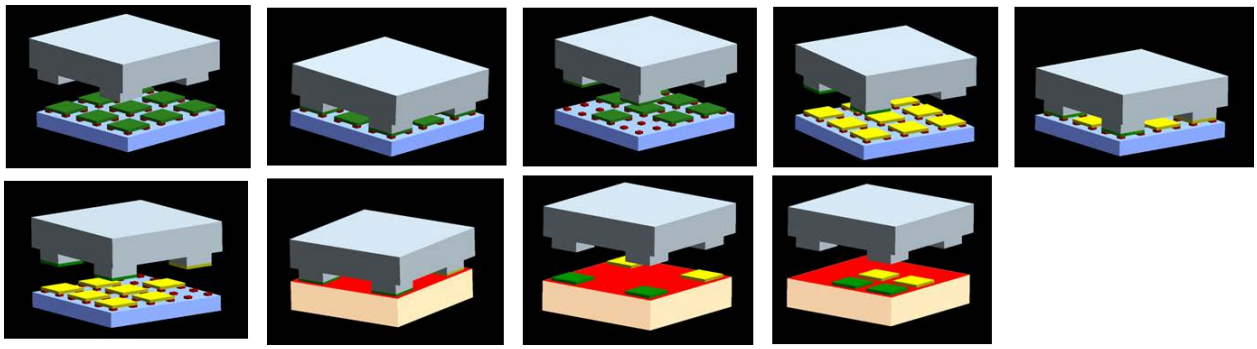

Figure 11**:** Schematic representation of micro transfer printing using a stamp that can modulate its geometry. Having the ability to control when posts make contact with a substrate can allow for device retrieval from multiple substrates. It also allows for printing devices in patterns that are independent of stamp geometry and also allows for printing in a collect and place regime rather than a pick and place regime.

Having the ability to modulate the stamp geometry to control which post on the stamp makes contact with the substrate can eliminate the shortcomings of a fixed geometry stamp. The ability to modulate contact provides features such as device retrieval from multiple substrates by modulating contact. It allows printing independent of the geometry of the stamp. Another improvement is the use of a collect and place regime in which a large number of devices and be picked up in a single retrieval step and then printed, this eliminates the back and forth travel required using simple pick and place. These modes are shown schematically in figure 11. Thus the functionality of actuating the stamp at the scale of individual posts; allowing the stamp to modulate its geometry and control when a post makes contact with a substrate is a transformative imporvement.

2.2 Active composite material based stamps

To add the desired functionality into the micro transfer printing stamps we propose a general architecture of a multilayer active composite material. Each required function is assigned to a separate layer of the composite. Figure 12 shows the general architecture of the active composite materical. It is composed of four basic layers, a functional layer, an actuation layer, a

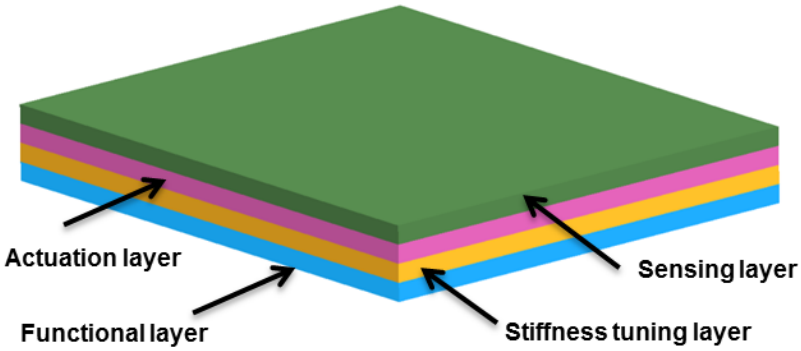

Figure 12: General architecture of the active composite material

stiffness tuning layer and a sensing layer. Each layer is patterned according to design requirements. Additional layers needed for operation can be added to the composite structure as and when needed.

Using the active composite material, stamps with desired functionality are formed by replacing the compliance of the bulk stamp by a mechanical system that can emulate the behavior of a bulk stamp from a process stand pint. We propose an architecture whereby cantilever beams composed of the active composite are embedded into the stamp. The cantilever beams allow us to

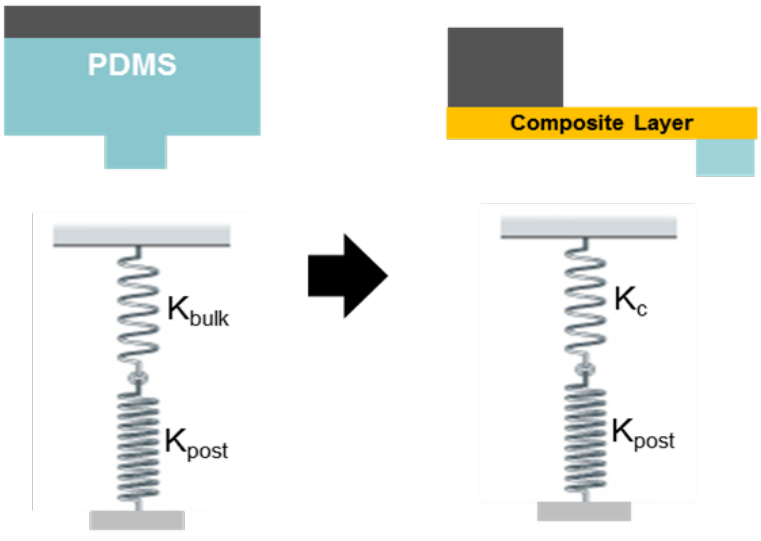

Figure 13: Schematic representation of the design concept. The compliance of the bulk PDMS (K_{bulk}) is replaced by the compliance of the cantilever beam (K_c) made from the active composite material.

tune the compliance locally to match the compliance of a bulk stamp. The cantilevers being made up from the active composite matrial enables the local integration of the required functionality. The concept is shown schematically in figure 13.

CHAPTER 3: INSTRUMENTED COMPOSITE STAMPS

During transfer printing, the extraction of the ink from the donor substrate or its embedding into the receiving substrate generates interaction forces that result in a proportional local elastic strain at and around each post. By embedding a suitable sensor in the vicinity of the post, this local strain can be transduced into an electrical signal that is proportional to the printing forces acting on the posts that can be used for process monitoring and control. This chapter addresses the development of the framework to add sensing into the stamps, their design, fabrication, experimental testing and final use in the micro transfer printing process.

3.1 Instrumented composite stamp concept

The instrumented composite stamps are based on the active composite material. Since only integration of sensing is required the actuation layer is not included in the system.

To start developing the stamp, the first step was to select the material for the individual layers. Since the stamps are used for micro transfer printing, the functional material was selected to be a thin layer of PDMS; the same material as the bulk stamp. The PDMS will have posts patterned on it. The stiffness tuning layer was chosen to be made from a permanent photoresist; to enable fabrication using standard microfabrication techniques. SU-8 a negative tone permanent photoresist was chosen for its good mechanical and chemical properties. The sensing layer was selected to be composed of metal strain gages. The stamp is composed of cantilevers made from the composite material embedded into the stamp. A thick handle layer with windows patterned into it – to allow free deflection of the cantilever – is added to the stamp to provide mechanical

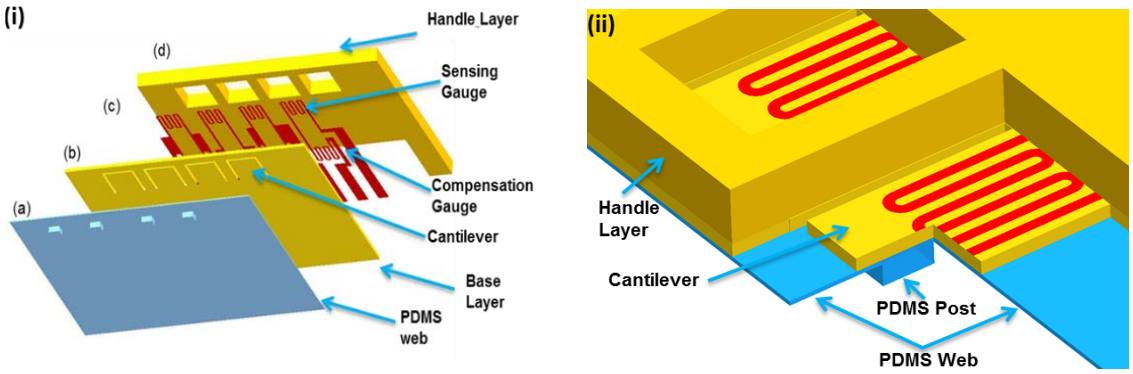

Figure 14: Solid model of the instrumented composite stamp. (i) Exploded view of the individual layers. (a) PDMS web with posts. (b) SU-8 layer that forms the cantilevers. (c) Metal layer with the sensing strain gauge along with the compensation resistors and contact pads. (d) SU-8 handle layer with windows to allow free movement of the cantilever and optical feedback. (ii) Cut out of a stamp showing how the various layers are integrated into the final stack and what the cantilever looks like.

stability and allow for stamp attachment. Figure 14 shows a solid model of the instrumented stamp concept, showing how the individual layers are integrated to form the stamp.

3.2 Assessing feasibility of instrumented composite stamps

After the conceptual design of the instrumented composite stamp, we first conducted a set of experiments to test the feasibility of using such a system within micro transfer printing. The aim of the experiment was to test whether such a system could be used to perform transfer printing, will the signal resolution be sufficient to measure the miniscule forces encountered during the process and how will such stamps be integrated into the micro transfer printing process. This pilot study allowed us to test a simple system without investing the effort of developing and optimizing a previously untested fabrication process.

We developed the test stamps using commercial off the shelf strain gages. The strain gages were bonded to a glass slide to form a cantilever beam, a small PDMS post was manually attached to the free end of the strain gage. Following the fabrication of the cantilevered stamp it was attached onto the transfer printer. This system qualitatively represents a single post of the

conceptual instrumented composite stamp and was used for testing the feasibility. Figure 15 shows the image of a single cantilever stamp used for the pilot experiments. Using these cantilevered stamps helped us in developing the testing and calibration protocols and develop system integration techniques.

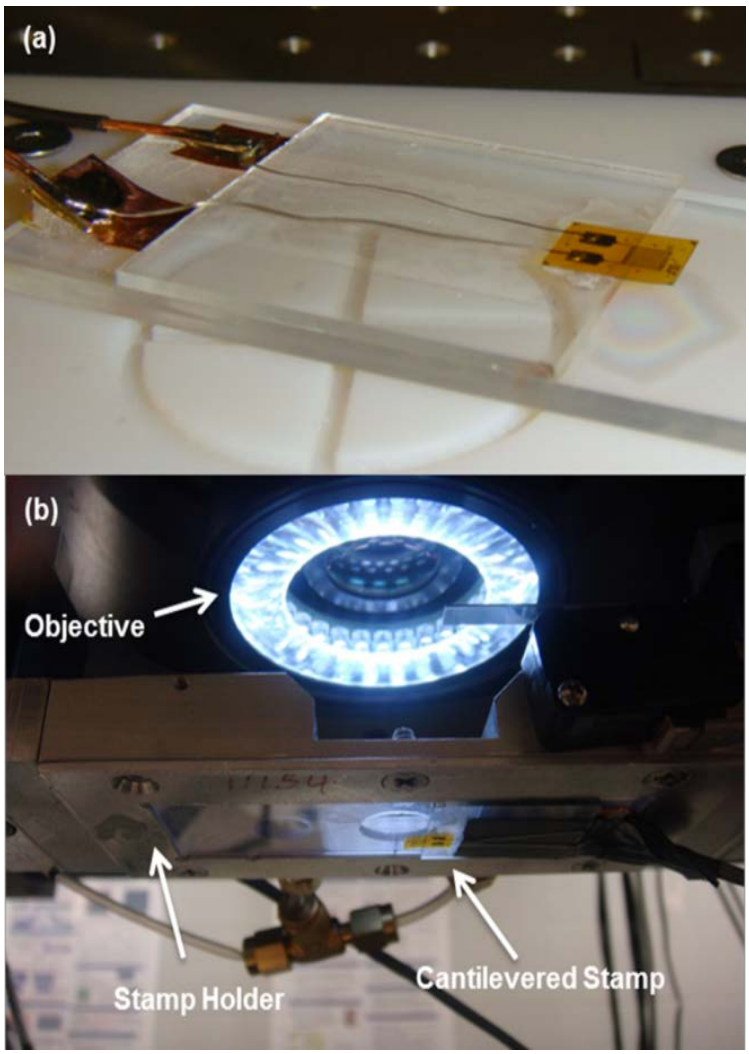

Figure 15: Cantilevered stamps formed using commercial off the shelf strain gage. (a) Strain gage attached to a glass slide forming a cantilever. (b) Image of the cantilever stamp counted onto the transfer printer for experimental testing.

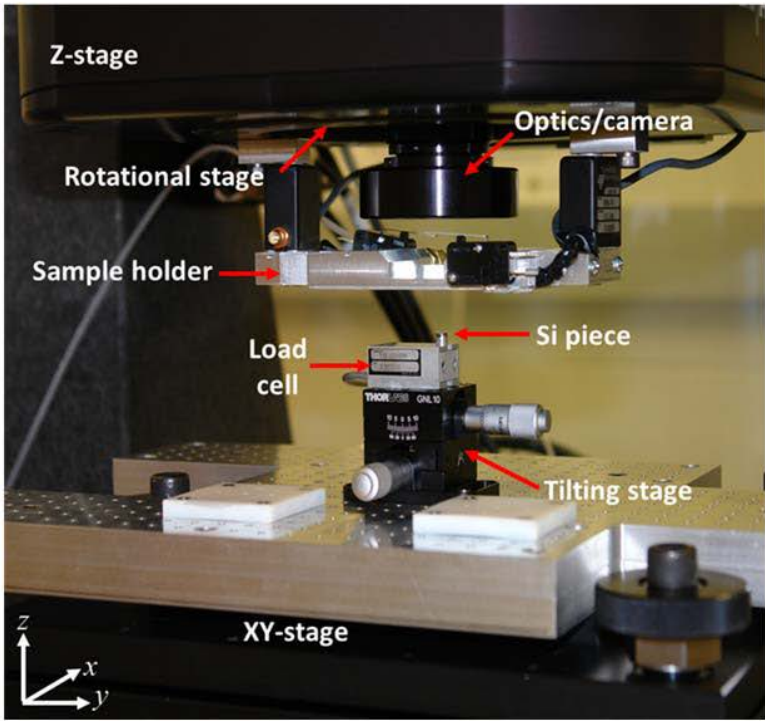

Figure 16**:** Image of the custom calibration and testing system integrated into the transfer printing tool. Work done in collaboration with John A. Rogers' group. Taken from A. Carlson's Ph.D. dissertation.

3.2.1 Custom calibration and testing setup

To measure and test the cantilevered stamps a custom calibration and testing system was developed. The setup was designed to be easily integrated into the micro transfer printing tool. The system is shown in figure 16. It consists of a precision loadcell (GSO-10, Transducer Techniques) that attaches on top of a two axis goniometer stage (GNL-20, Thor Labs), mounted onto the X-Y stage of the transfer printing tool. A measuring post with a Silicon piece bonded to it is inserted into the loadcell. During testing the PDMS posts on the stamp make contact with this piece of Silicon. The stamps are mounted onto the Stamp holder mounted to the Z-stage of the transfer printing tool, which is used to move the stamp during testing.

3.2.2 System integration scheme

Using the pilot setup the system integration scheme along with the interface electronics were developed and tested. The cantilevered stamp is interfaced with the micro transfer printing tool by connecting its strain gage to a Wheatstone bridge. The output from the Wheatstone bridge is amplified using an instrumentation amplifier (AD622, Analog Devices). The amplified signal is then sent into a data acquisition system with an integrated analog-to-digital converter (USB-6009, 14-bit ADC, National Instruments). The acquired signal is then fed into the transfer printing tool software. Figure 17 shows a schematic of the system connection diagram.

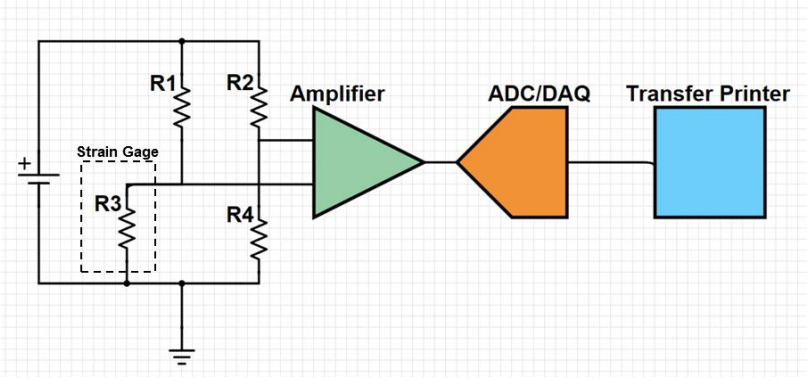

Figure 17: Schematic representation of the cantilevered stamp system integration setup.

3.2.3 Cantilevered stamp experimental testing

To test the cantilevered stamp first the stiffness of the stamp is measured. The cantilever stamp has a 250 µm x 250 µm, 100 µm tall PDMS post attached to its free end. For comparison, the stiffness of a bulk PDMS stamp with the same sized post was also measured. To measure the stiffness; the post on the stamp is brought into contact with the silicon piece attached to the loadcell of the testing and calibration system of figure 16. After contact the Z-axis of the transfer printer is moved downwards by known distances. With the stamp being the only compliant part, any

movement of the Z-axis results in the deformation of the stamp and post, as the Z-axis is moved downward a reaction force is also registered using the loadcell. Using this method the force versus deflection relationship of both the bulk PDMS stamp and the cantilevered stamp were recorded. From these experiments the stiffness of the bulk PDMS stamp and the cantilevered stamp was measured to be 600 N/m and 70 N/m respectively.

After measuring stiffness of the cantilevered stamp, the next step was to verify whether the rate dependent adhesion effect seen in the bulk PDMS is preserved (the behavior schematically shown in figure 4). To measure this, the stamp was brought into contact with the silicon piece attached to the loadcell. This time maintaining a constant preload the Silicon/PDMS interface created by the PDMS post making contact with the Silicon, was broken. The peak force at which the interface is broken as a function of stage velocity was recorded. The typical trace that is measured from the loadcell as the stamp is brought into contact and then delaminated from the silicon is showin in figure 18 (a). Figure 18 (b) shows the rate dependent behavior measured for a bulk stamp and a cantilevered stamp. We observed a much smaller rate dependent adhesion response for the cantilevered stamp compared to the bulk stamp. The reduction in the delamination

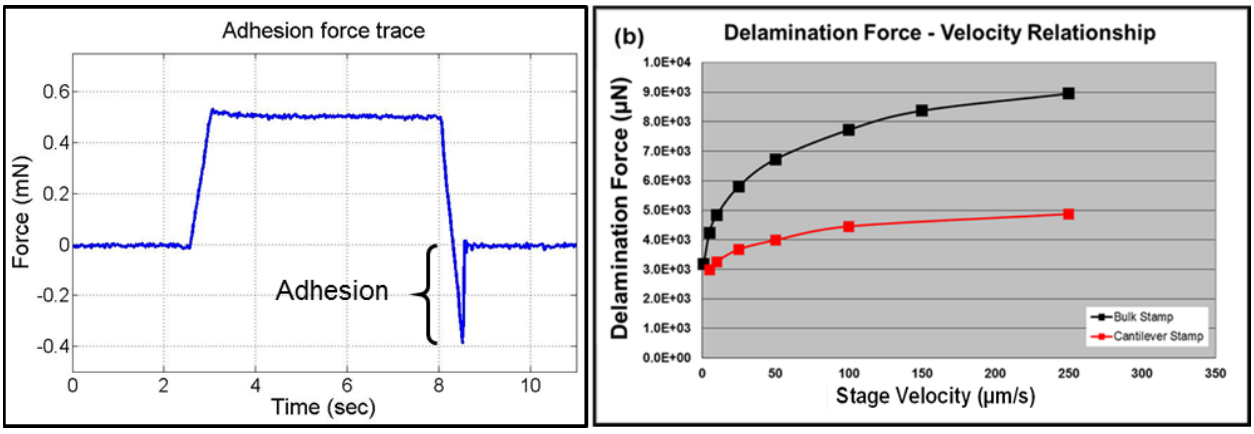

Figure 18: (a) A typical trace captured during the rate dependent adhesion measurement experiments. (b) Measured rate dependent adhesion effect for a bulk stamp and a cantilevered stamp.

force between the two systems can be explanied by the difference in stiffness of the two systems as explained in appendix A. The experiment successfully verified that the rate dependent adhesion effect is preserved by the cantilevered stamp.

After measuring and verifying that the rate dependent adhesion effects – the essential component to enable transfer printing – are preserved by the cantilevered stamp the ability of the stamps to perform transfer printing and signals generated during the process were experimentally measured.

Using 250 µm x 250 µm silicon chips fabricated following the process outlined in Appendix , micro transfer printing was performed using the cantilevered stamps. An array of 3x3 silicon chips was deposited onto a glass substrate using the cantilevered stamp; the results of the experiment are shown in figure 19. This experiment verified that cantilevered stamp architecture can produce sufficient forces to pick up and print ink during micro transfer printing.

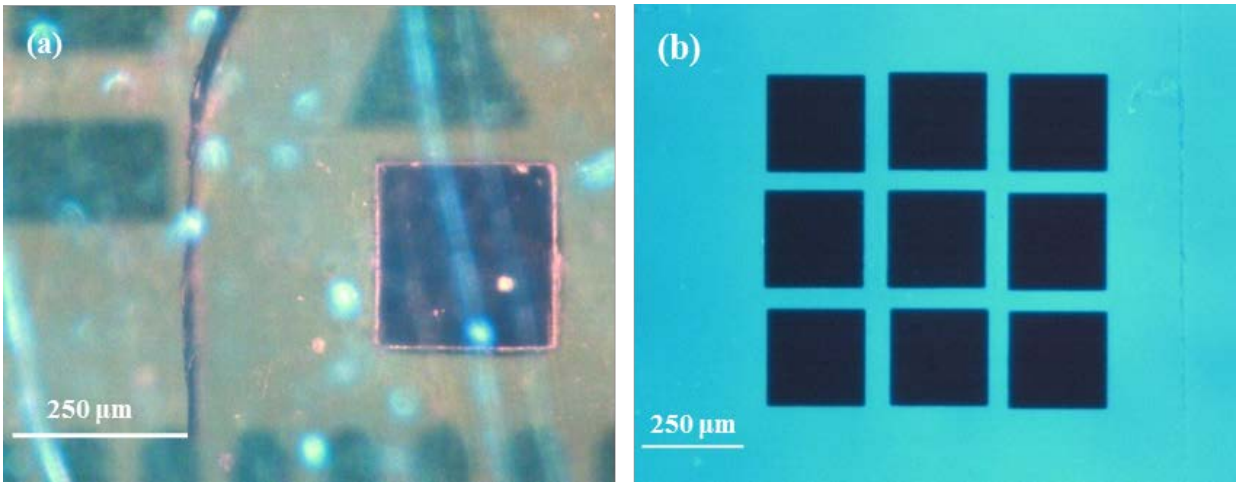

Figure 19: (a) Image captured from the micro transfer printing tool camera of a single silicon chip picked up and attached to the PDMS post of a cantilevered stamp. The image is taken from the top, observing through the cantilever. (b) Image of a 3x3 array of silicon chips assembled onto a glass substrate using micro transfer printing with cantilevered stamps.

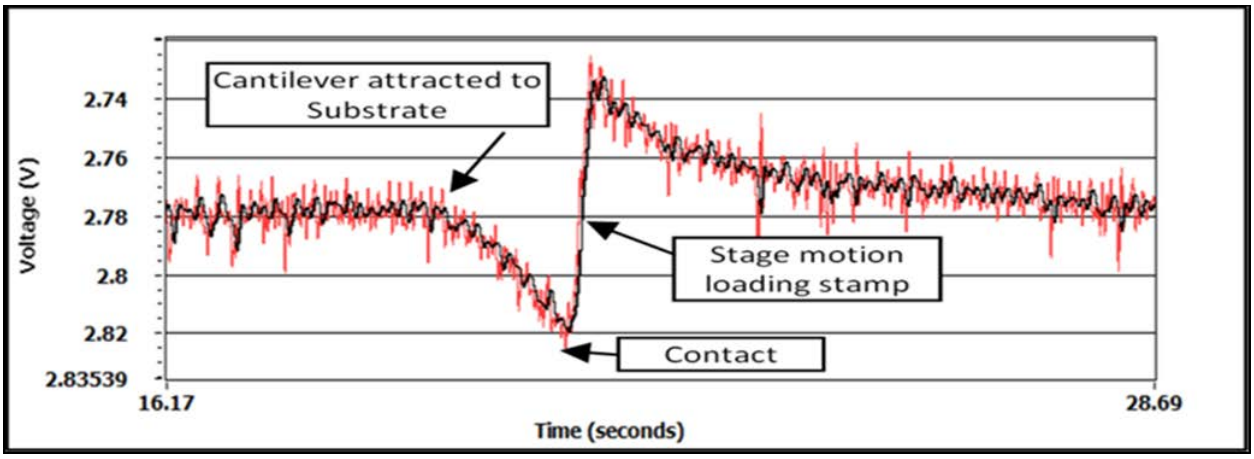

Figure 20: Image of a typical signal trace captured from the sensor of the cantilevered stamp.

Finally the signal from the strain gage in the cantilevered stamp was captured. The signal trace showed sufficient signal to noise ration and force resolution to measure important process event and delamination/adhesion force. A typical signal trace is shown in figure 20.

The experimental verification of requirements for performing micro transfer printing using the cantilevered stamps proved that a stamp based on the instrumented composite stamp architecture is a viable alternative to the bulk stamp. The next step was to develop a facile process for creating more precise arrays of stamps based on the original design concept.

3.3 Instrumented composite stamp design

Going back to the instrumented composite stamp concept shown in figure 14, the first layer is a thin PDMS web patterned with posts, similar to a bulk PDMS stamps but with a much smaller thickness. The second layer is made of SU-8 cantilevers connected to the rest of the substrate layer, to obtain localized and directional compliance behind the posts. These cantilevers replace the compliance of the bulk PDMS that backs the posts in a bulk stamp. Sensing the deflection of each cantilever is a metallic strain gauge. Each strain gauge is connected to a compensating strain gauge

that, in the composite stamp, is located in the rigid region away from the cantilevers. This is used for compensating thermal effects and common mode noise cancellation. Finally, an additional handle layer is patterned with windows to permit the free deflection of the cantilevers and provide access to electrical contact pads of the strain gauges. The handle layer provides the stamp with rigidity for easy of handling and attachment.

One important consideration in the design of the composite stamp is to make its behavior, at least from a process point of view, very similar to a conventional bulk PDMS transfer printing stamp. This is achieved to a large extent by maintaining the first layer of the composite stamp to be PDMS and patterning posts whose dimensions are the same as in conventional stamps. Next the dimensions of the cantilevers in the second layer of the composite and the thicknesses of the PDMS web and the SU-8 cantilever layer must be designed so that the overall stamp stiffness is in the desired range (close to the stiffness of a bulk stamp). Previous measurements of the stiffness of a bulk PDMS stamp with a 250μm x 250μm, 100 microns tall post, have shown the stiffness to be around 600 N/m [29]. For the composite stamps, a target stiffness of 300 N/m is chosen. A lower stiffness is chosen to produce a larger strain in the sensing cantilevers to make the stamp sensitive enough to detect events during the transfer printing process. The instrumented composite stamp is designed with a linear array of four posts with 250 μm x 250μm, heights of 100 microns, positioned at a pitch of 1 mm. It was experimentally determined that the smallest thickness for the PDMS membrane that could be fabricated with the available equipment was 20 μm. With this thickness of the PDMS web, the length and pitch of the cantilevers were fixed at 1mm, while width and thickness of the cantilevers were chosen to achieve the desired stamp stiffness. To do so, a 3-D finite element model of the composite stamp was developed. The model consists of a 20 μm layer of PDMS with the PDMS post attached to it. The PDMS membrane is bonded to an SU-8

cantilever whose dimensions are to be determined. The PDMS membrane was made larger than the SU-8 cantilever and the motion of its edges constrained (simulating its bonding to the rigid part of the stamp around the window in the backing layer). The SU-8 cantilever is free to move. A distributed load was applied at the PDMS post surface corresponding to applied force to the PDMS post and the corresponding deflection was calculated. The above identified dimensions were adjusted until the stiffness of the stamp became 300 N/m. From the analysis the required thickness and width of the SU-8 cantilever were calculated to be 40 µm and 650 µm respectively. Results

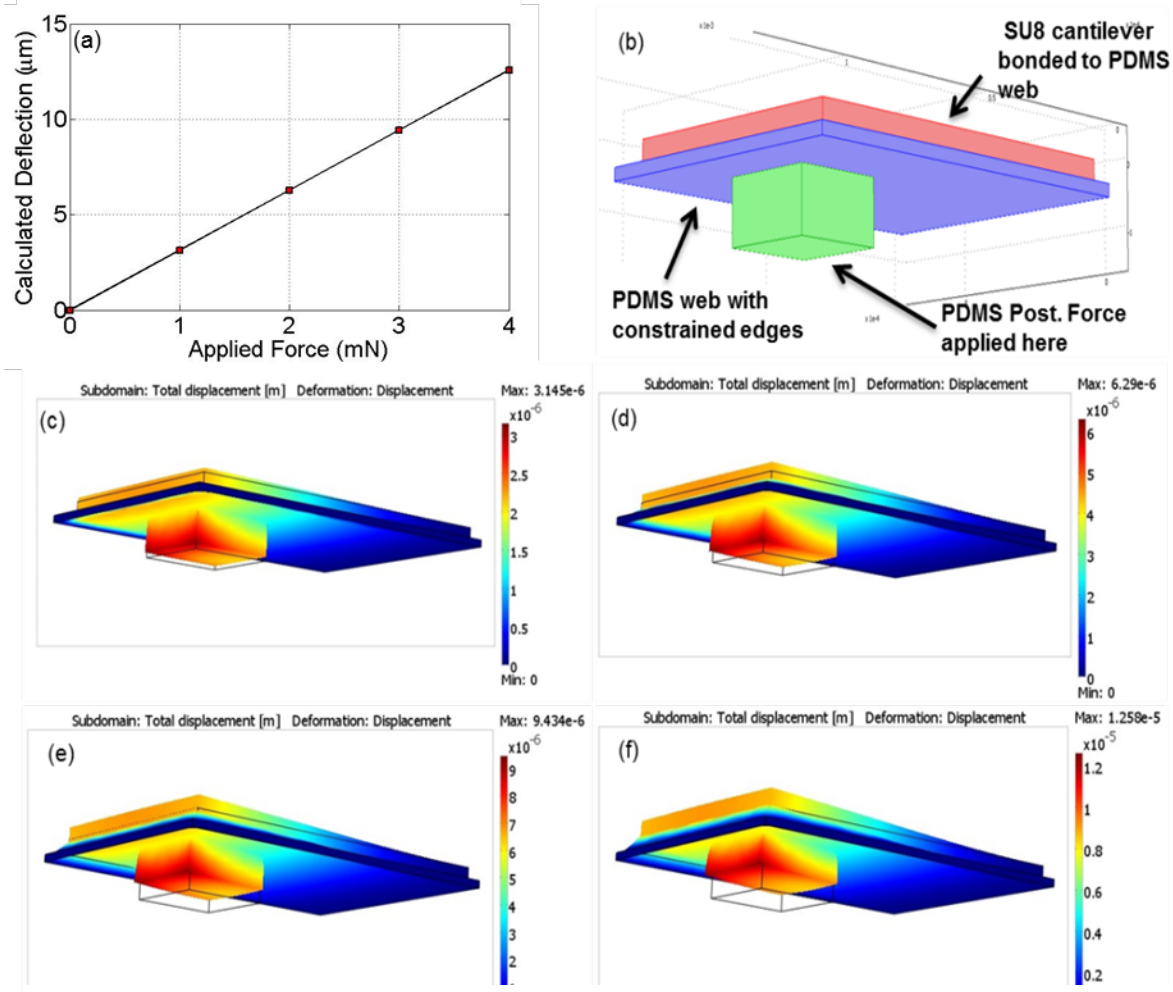

Figure 21**:** (a) Plot of applied force and calculated deflection from the FEA studies. (b) Image of the model used for the FEA. (d - f) The four frames from the FEA study done to determine the required dimensions of the composite stamp to achieve the target stiffness. Frames show the deflection of a single stamp when a distributed force of magnitude 1 mN, 2 mN, 3 mN and 4 mN is applied to the post surface, respectively.

from the FEA model are shown in figure 21. For a 1 mN force applied at the post the deflection of the stamp is calculated to be around 3 μm with forces starting with 1 mN and incrementing in steps of 1 mN up to 4 mN.

3.4 Instrumented composite stamp fabrication

The cantilever stamps primarily consists of 4 layers; a PDMS layer that forms a web that carries the posts, an SU-8 layer that forms the cantilevers that carry the strain gauges, a metallic sensing layer into which the strain gauges are patterned, and a thick SU-8 layer that forms the handle used to provide the stamp with rigidity for manipulation and mounting on the printing machines.

Figure 22 schematically shows the fabrication process for the four layers of the instrumented composite stamps. Fabrication begins with the manufacturing of an SU-8 master mold, used to mold the PDMS layer. The mold also serves as the handle for all the processing steps in the manufacture of the composite stamp. A 100 micron film of SU-8 100 (from Microchem Corp.) is spun on to a polished silicon wafer and photo-lithographically patterned with square holes (for the posts on the PDMS layer). Before use, the SU-8 surface is treated with (Tridecafluoro-

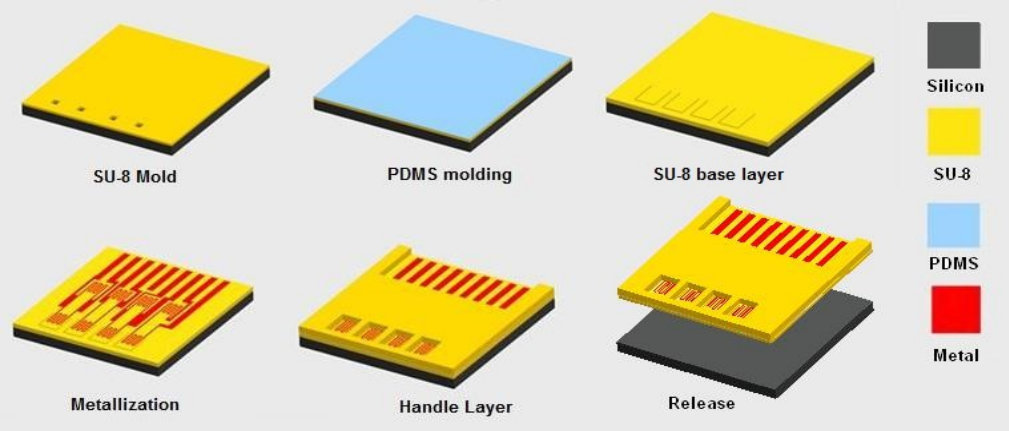

Figure 22: Schematic representation of the instrumented composite stamp fabrication process showing the constituent layers

1,1,2,2-Tetrahydrooctyl)-1-Dimethylchlorosilane (from UCT Inc.), to prevent the PDMS from sticking to the mold and to facilitate eventual de-molding of the composite stamp after fabrication. PDMS (SLYGARD 184 SILICONE ELASTOMER from Dow Corning Corp.) is spun coated onto the mold to form a PDMS web that carries the posts. The PDMS is cured in a vacuum oven at 70 ^{o}C for 24 hours.

The next step begins with preparing the PDMS surface for the SU-8 cantilever layer. Typically, SU-8 has poor adhesion with PDMS. As a result it is difficult to spin SU-8 on a PDMS surface. Bonding of PDMS and SU-8 has typically been achieved by creating an amino group on the PDMS surface using Oxygen and Nitrogen plasma [52]. For our fabrication process we functionalized the PDMS surface with a self-assembled monolayer (SAM) containing an amino group. First the PDMS surface was activated using Oxygen plasma at 100 watts for 1 minute. Then the activated PDMS was soaked into a 1% v/v solution of (3-Aminopropyl)triethoxysilane (from Sigma-Aldrich Corp) in methanol for 15 minutes, and then dipped in methanol for 2 minutes. This leaves behind a SAM on top of the PDMS which acts as an adhesion promoter for SU-8 and permanently bonds the PDMS and SU-8 together. After application of the SAM, SU-8 fabrication is carried out by spinning a 40 micron layer and photolithographically patterning the cantilevers above the regions of the PDMS web carrying the posts, forming the base layer.

A 50 nm layer of Gold is sputtered on to the SU-8 base layer, after sputtering a 10 nm Cr adhesion layer. The strain gauges, contacts and interconnects are then patterned in this metal layer. Special care is taken to perform all the fabrication steps at a maximum temperature of 75^{o}C to reduce bending of the cantilevers because of internal stresses in the SU-8. Next, a 200 micron SU-8 layer is spun on and patterned to form the handle layer of the stamp, providing it with rigidity

for ease of handling and mounting. Figure 23 shows the image of an array of 9 instrumented composite stamps after completion of the fabrication process.

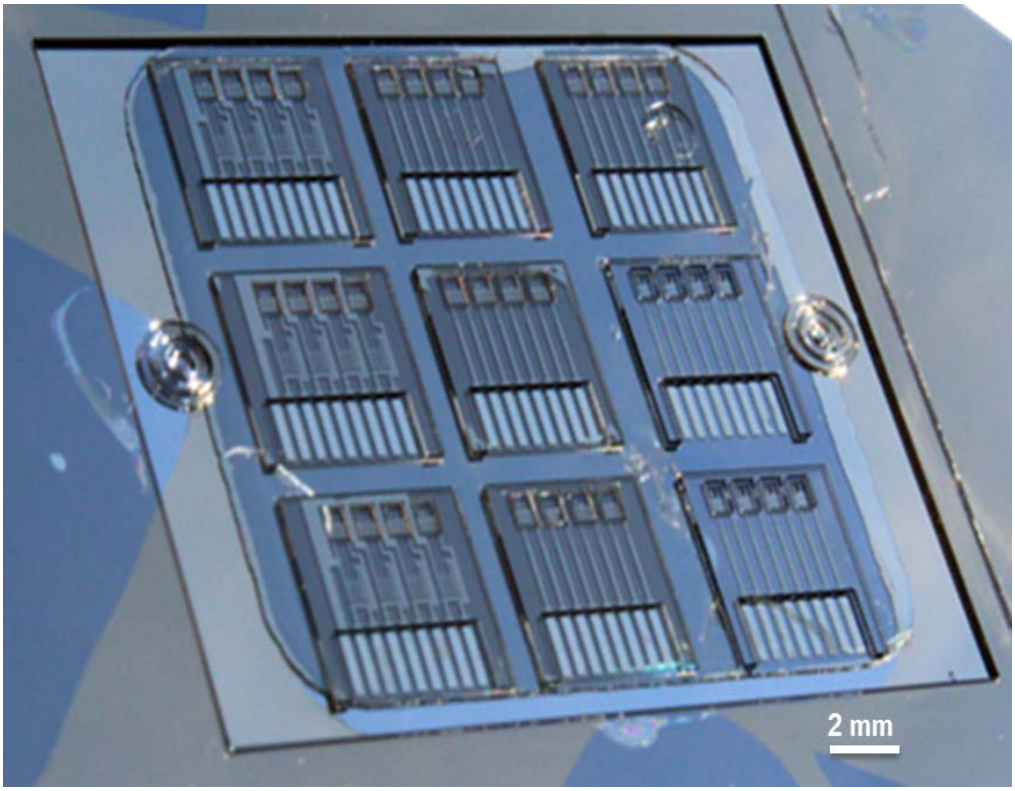

Figure 23**:** Image of an array of nine instrumented composite stamps prior to release from the SU-8 mold.

After fabrication, the instrumented composite stamps are released from the mold by separating the PDMS from the mold at one corner with a sharp blade and gently peeling the stamp away from the mold. Anisotropic Conductive Film (ACF) is then bonded to the contact pads for connecting with the readout circuitry. The stamp is then bonded to a glass slide using either Norland Optical Adhesive NOA 73 (from Norland Products Inc.) or double sided Kapton tape. Figure 24 shows the stamp attached to the transfer printer.

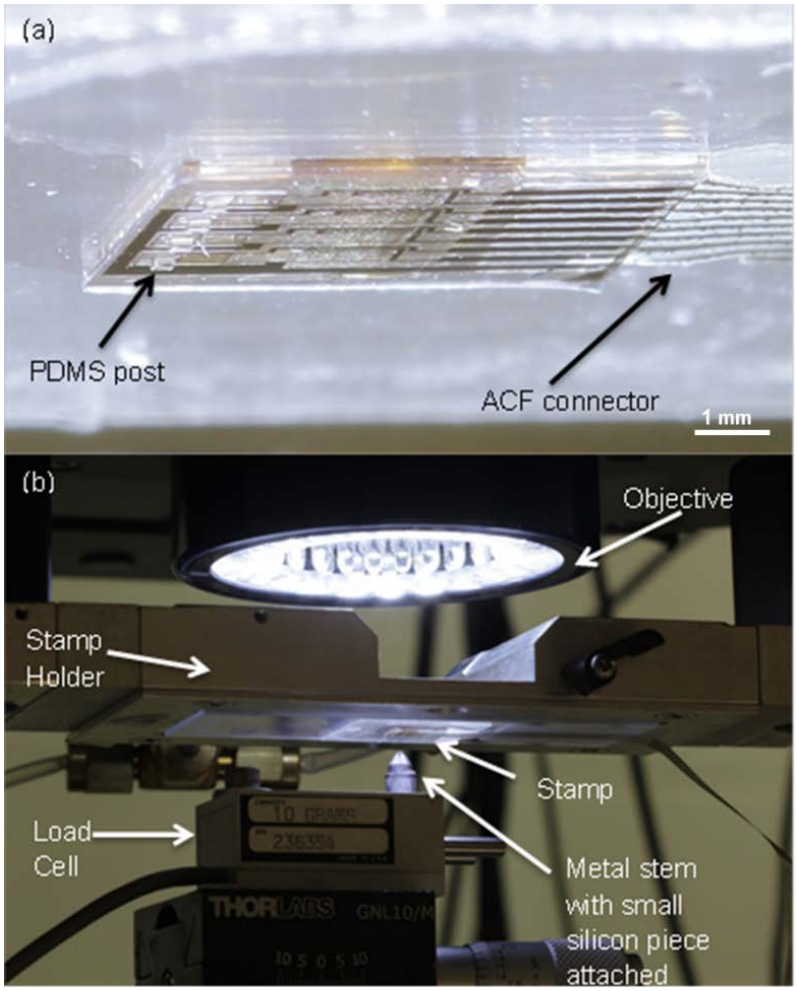

Figure 24: (a) Close up image of the composite stamp attached to the transfer printing. The image shows the ACF film used to connect contacts with the interface circuitry and the array of PDMS posts. (b) Image shows the composite stamp attached to the transfer printed and the test setup used for stamp characterization.

3.5 Instrumented composite stamp characterization

The instrumented composite stamp was characterized to measure its stiffness and its force sensing capabilities. It is also tested to verify that the dependence of the adhesion of the stamp-ink interface on separation velocity is preserved. To begin, for each printing post or cantilever on the stamp (and the stamps are fabricated with a linear array of 4 posts), the measuring strain gage is connected to form a Wheatstone bridge with its compensating gauge and a pair of matched

resistors, similar to the interface scheme presented earlier in figure 17. The Wheatstone bridge excitation voltage is 1.5 V and the output of the Wheatstone bridge is amplified 1000 times using an instrumentation amplifier. The amplified signal is then collected using the data acquisition system. The interfaced stamp is mounted into the transfer printing machine. The stamp is characterized using the custom calibration and testing setup that was presented earlier. The image of the stamp being tested using this setup is shown in figure 24(b).

3.5.1 Stiffness measurement

To measure the stiffness of the instrumented stamp, each post on the stamp was brought into contact with the silicon die attached to the load cell. The z-axis or vertical axis of the printer (to which the stamp is attached) is moved downwards through a known displacement (here 3 microns). Because the post and the cantilever in the stamp are the only compliant elements in the

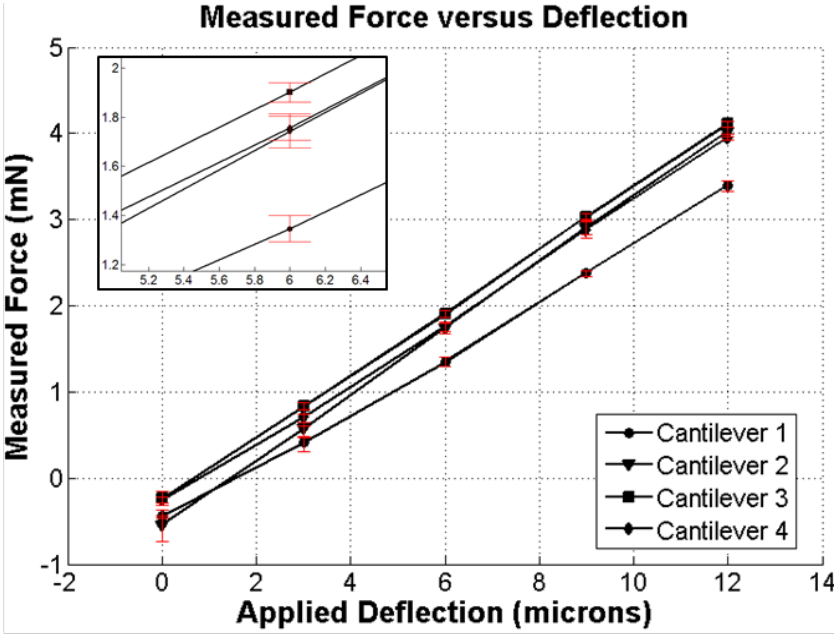

Figure 25: Graph of measured forces as a function of deflection of the cantilevers in the instrumented composite stamp when each of the 4 posts is pressed against a substrate. The insert shows typical RMS error of the measurement.

set-up, the displacement of the z-axis is accommodated by stamp deflection. Thus, the programmed displacement represents the deflection of the stamp. The resulting force applied to the load cell is recorded to produce force versus displacement curve for the post or cantilever in contact with the silicon die. Figure 25 shows the force deflection curves for the four cantilevers/posts of a composite stamp. Each measurement is repeated 5 times. It can be seen that the stiffness of the stamp at the posts was measured to be around 330 N/m, the design stiffness for each stamp post was 300 N/m.

3.5.2 Sensitivity measurement

During the stiffness testing where the stamp is deflected and forces measured, the voltage output from the bridge circuit of the strain gauges was also recorded. The cantilever senses the force applied to it as a change in resistance of its sensing strain gauge, which experiences a strain as the cantilever bends in response to the applied force. The change in resistance of the strain gauge is given by:

$$\Delta R_s = \varepsilon G R_s \tag{3.1}$$

Here, ε is the induced strain; G is the gauge factor (typically ~2 for thin film metals) and R_s is nominal resistance of the sensing element under no strain. The strain gauge is connected with matching resistors to form a Wheatstone bridge whose output is connected to an instrumentation amplifier. This amplified voltage is read out as the signal coming from the instrumented stamp and is given by:

$$V_o = \frac{A \times R \times \Delta R_s \times V_e}{(R + R_s)^2} \tag{3.2}$$

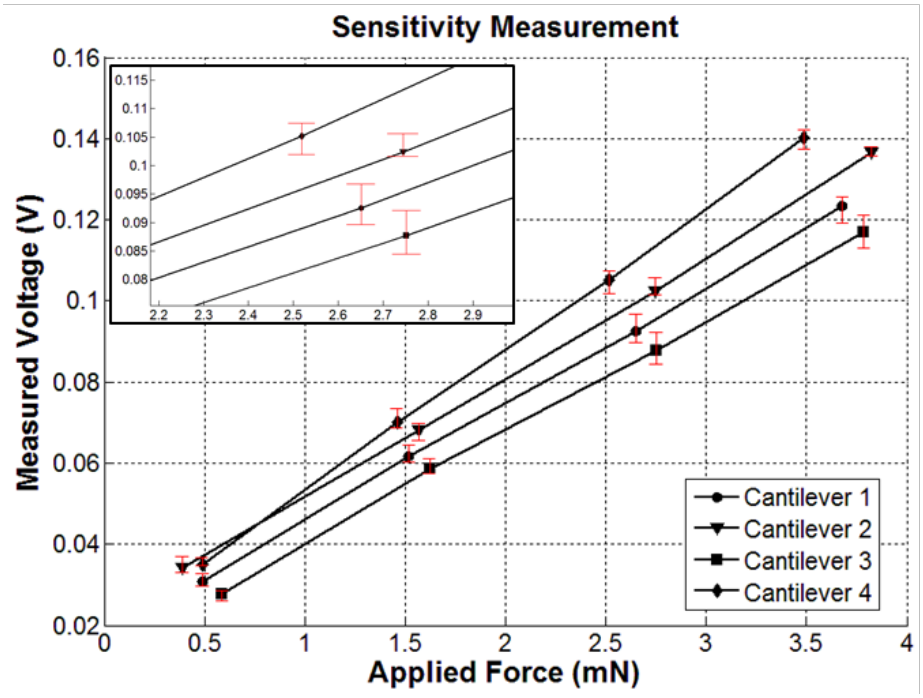

Figure 26**:** The voltage output from the bridge circuit (for each of the cantilevers) plotted against the applied forces at each of the corresponding posts. The insert shows typical RMS error of the measurement.

Here A is the amplification factor of the instrumentation amplifier; R is the resistance of the Wheatstone bridge resistors; V_e is the excitation voltage applied to the Wheatstone bridge. Finally we define the sensitivity as:

$$S = \frac{V_o}{F} = \underbrace{\left[\frac{A \times R}{(R + R_s)^2}\right]}_{Constant} \times \left(\frac{\Delta R_s}{F}\right) \times V_e \tag{3.3}$$

Figure 26 shows the force-voltage relationship for the four cantilevers of the array. The average sensitivity was measured to be 45 mV/mN per volt of applied bridge excitation voltage. For the operation of the composite stamp we use an excitation voltage of 1.5V.

3.5.3 Adhesion force measurements

The dependence of adhesion forces between PDMS and silicon on delamination or separation velocity is central to the functioning of adhesive less transfer printing. Even though, this is a property of the interface and not the volume within the stamp, it is necessary to ensure that this dependence is preserved in the composite stamp. To check this dependence, a single post on the composite stamp is brought into contact with a silicon die, mounted on the load cell, by slowly moving the z-axis of the printer. The post is pressed into substrate until a contact force of approximately 40 mN is generated. The z-axis is then reversed and moved away from the silicon die at controlled velocity. The maximum force generated is recorded and the delamination or adhesion force is calculated. Figure 27 shows a typical signal generated during such an experiment

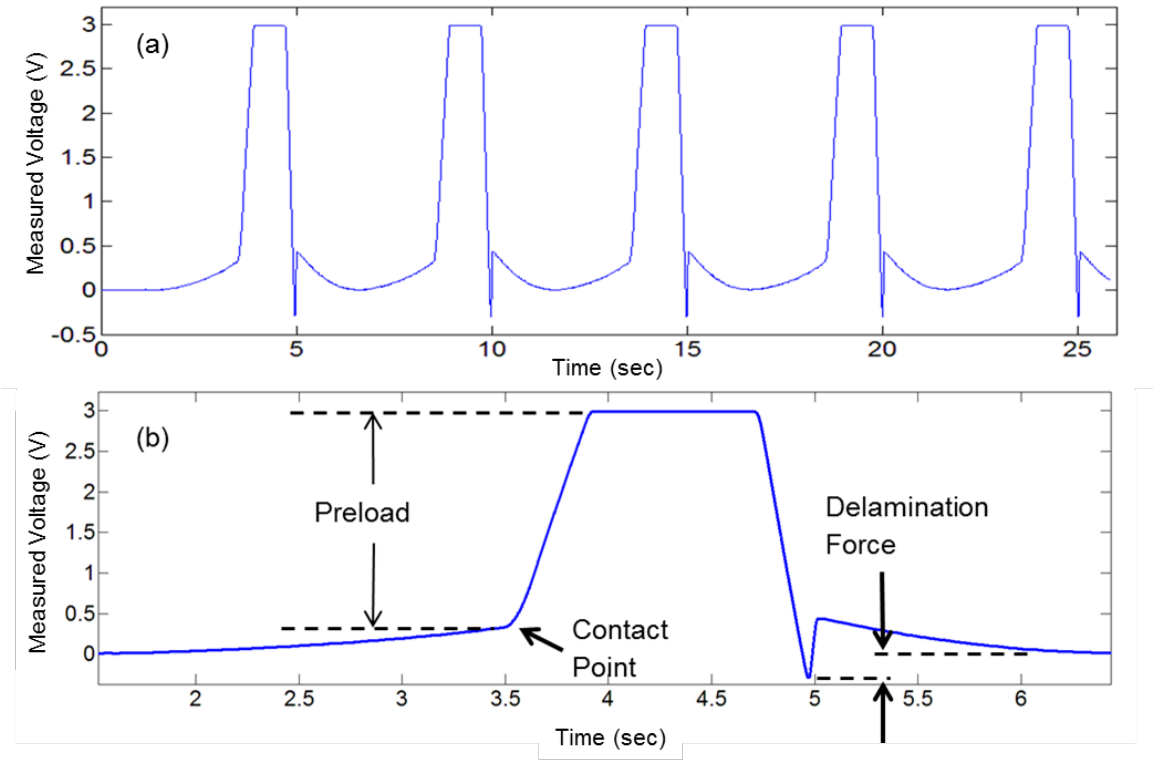

Figure 27: (a) Graph of voltage signal generated during adhesion testing experiment. The graph shows the voltage trace for repeated adhesion force measurement experiments. (b) Close-up of a single contact and delamination event.

and schematically depicts how the adhesion/delamination force is calculated. This experiment is repeated five times for each velocity. Figure 28 shows a plot of the measured delamination force as a function of delamination velocity. For purposes of comparison, delamination forces for a bulk stamp, measured by the load cell, have also been plotted on the same graph. As is apparent, the strong dependence of this force on velocity of separation is preserved in the composite stamp. The measured rate dependent adhesion of the instrumented stamp also approaches the baseline value of the bulk stamp as the stiffness of the instrumented stamp is closer to the bulk PDMS as compared to the results measured for the cantilevered stamp, this result is also apparent from the treatment presented in appendix A.

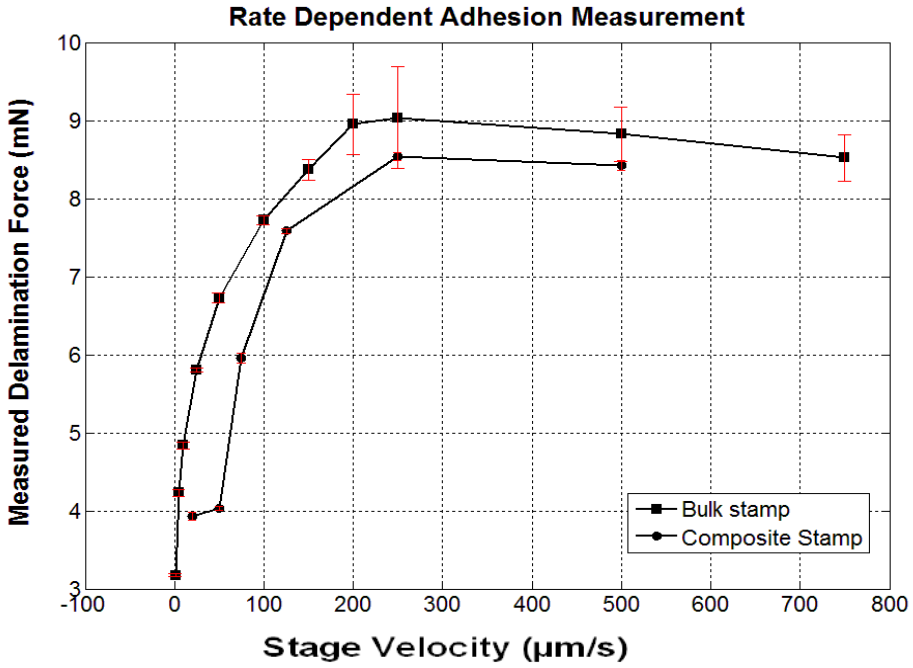

Figure 28**:** Graph of Adhesion force between PDMS and silicon and its dependence on delamination velocity for a bulk PDMS stamp and the composite stamp. The error bars represent the RMS error for the measured variable.

3.6 Transfer printing with instrumented composite stamps

Automated transfer printing is conventionally performed by programming in positions. While lateral positioning is essential for proper overlay registration, vertical positioning is essential

for successful pick up and printing. Tilting or vertical positioning errors of a substrate with respect to the programming reference frame can lead to inadequate contact of the stamp with the ink during pick up or inadequate contact of the ink with the receiving substrate during printing, both resulting in a failed print cycle. The introduction of force sensing capabilities in the stamp, in many ways, simplifies setup procedures as the output of the sensor can be used to detect contact between the stamp and the substrate. Analysis of the positions at which these events occur provides input for in-program compensation of misalignments. However, here we demonstrate how the force signals from the instrumented stamp are integrated into the printing cycle to make it more robust. Figure 29 shows a schematic trace of programmed motion during a conventional print cycle. While much of the executed motion is rapid motion to bring the stamp in close proximity to (typically a millimeter above) the location of engagement with the substrates ('Ready Point', in figure 29), the engagement with the substrate and the withdrawal from it are velocity-controlled motions. Further,

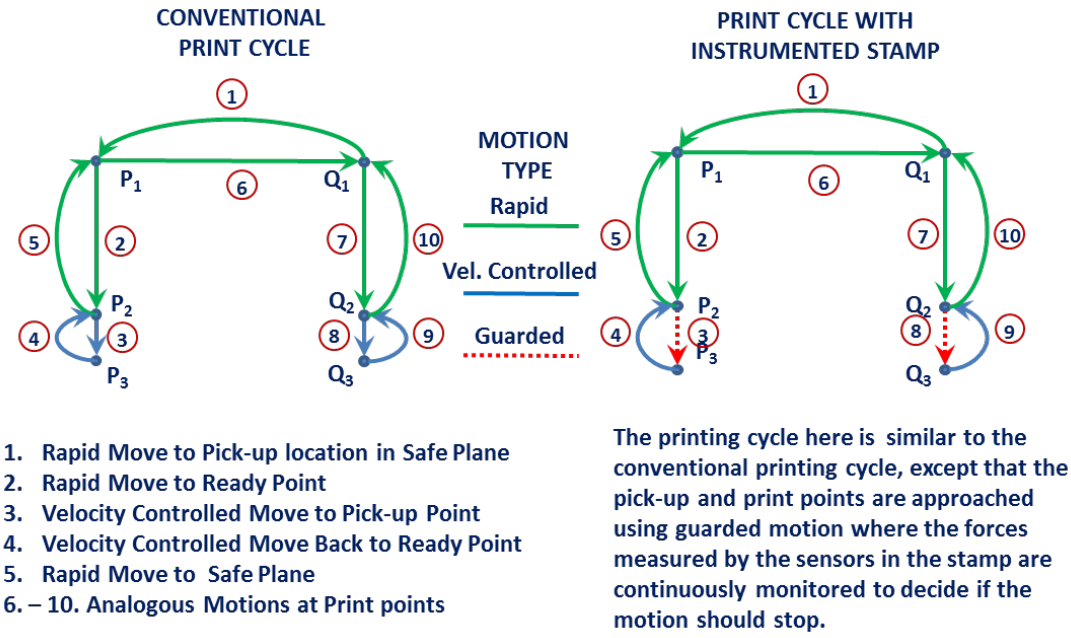

Figure 29: Schematic representations of a conventional transfer printing cycle (left) and one with an instrumented stamp (right). With an instrumented stamp, the stamp's engagement with the donor and receiver substrate can be controlled by monitoring the output of the strain gauges at each post.

the total force with which the stamp is pressed against the substrate is determined by the 'Pick-up' or 'Print' points (P3 and Q3) which, without the resistance of the substrates, would locate the inks below the surface of the substrates. Incomplete engagements caused misalignments and substrate flatness errors can lead to failure to pick up or print. Similarly, too much engagement can lead to stamp collapse and the loss of both, the substrate and stamp.

To develop a more robust print cycle, sensor information from each post is inserted into the cycle to define a sensor guarded move, where the forces at each post are continuously monitored as the stamp is brought into contact with the substrate. How this guarded motion is introduced in the print cycle is shown in figure 29. Points P3 and Q3 are located as deep in the substrates as is safe to do so. In the guarded move, when the forces on all the posts have crossed a defined threshold, the machine stops and dwells before executing the next statement in the program, i.e., the withdrawal from the substrate. For example, a statement like G_Move(P, V, [S1,….,Sn], T, Flag) is programmed as a macro asking the machine to move towards point P at a velocity of V until the outputs of the sensors in the set [S1,….,Sn], exceed threshold T. When the

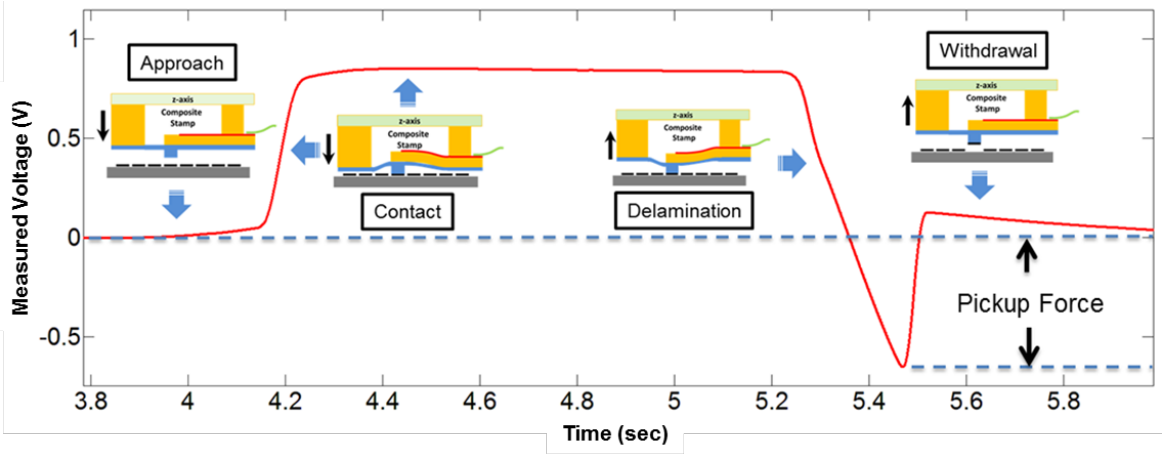

Figure 30: Voltage trace recorded for a post during engagement with the donor substrate in a printing cycle. The figure shows how the voltage output from the stamp changes with time during various events during engagement. Motion of the machine Z-stage stops once the output voltage reaches the threshold of 0.75V.

move is completed Flag indicates whether the move completed by the machine reaching point P or the sensors crossing threshold T. Figure 30 shows the output from a sensor during the engagement/withdrawal with the donor substrate during printing. Here the guarded motion is programmed to stop once the strain gauge output reaches a threshold of 0.75V (approximately 10mN force). During withdrawal, the pick-up force needed to cause failure of the anchor holding the ink on the donor substrate is also shown in the figure.

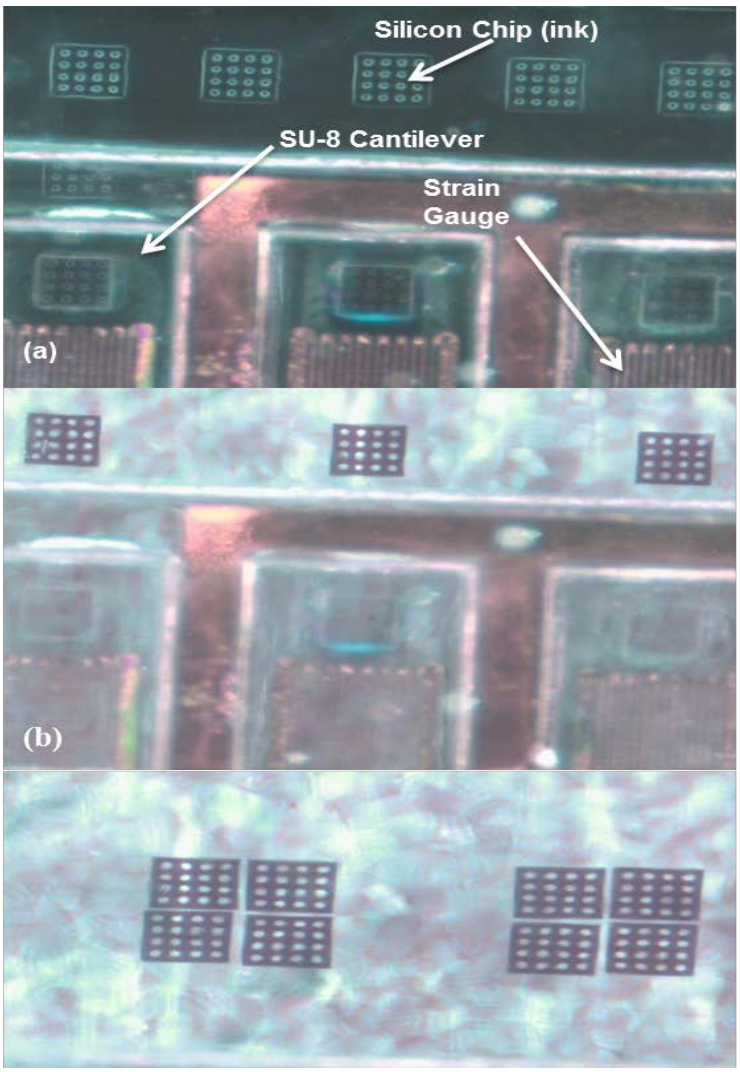

Figure 31**:** Image of stamp and ink during automated transfer printing process. Only three of the four cantilevers are visible due to the limited field of view of the optics (a) Image of stamp above the donor substrate. (b) Silicon chips (ink) printed on the acceptor. (c) Finished 2x2 array of ink for two of the four posts on the stamp.

To test this new force controlled transfer printing cycle, silicon chips (ink) with dimensions 250 µm x 250 µm and a thickness of 3 µm were extracted from a silicon donor substrate and printed into a glass substrate. The chips are fabricated on an SOI wafer by conventional lithographic processes following the general process outlined in Appendix B. The buried oxide layer is undercut etched to release the ink from the handle substrate. The ink is kept in place on the substrate by breakable photoresist anchors Figure 31 shows a set of micrographs taken by the vision system on the printer through the stamp, showing the result of an automated printing session with the instrumented composite stamp, demonstrating the working of this mode of printing.

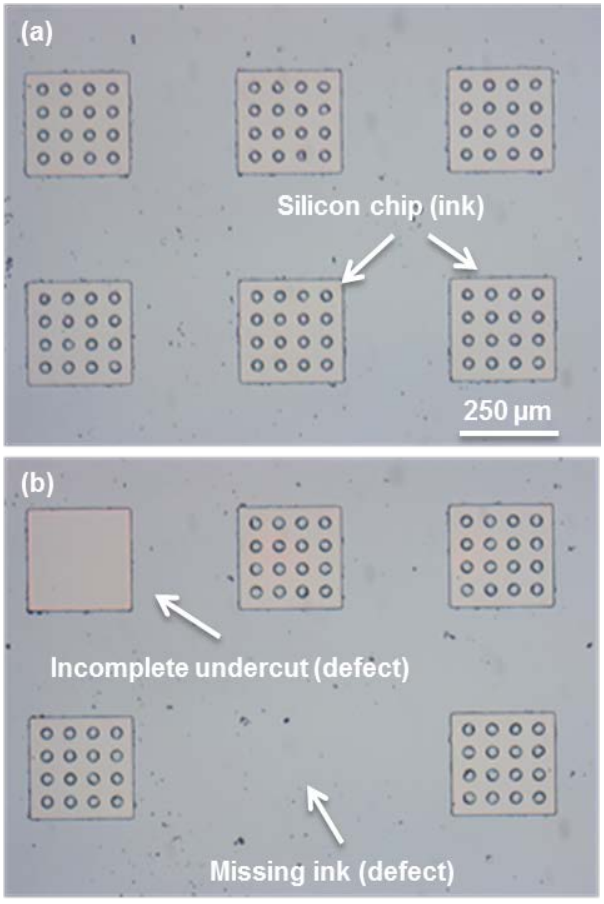

Figure 32: Image of the test donor wafer. (a) Micrograph of training area of donor wafer showing individual ink used for training. (b) Micrograph of teat area of donor wafer showing engineered defect location used for testing error detection.

Different parts of the printing cycle, i.e., picking-up ink from the donor substrate and printing on the receiving substrate are shown in figure 31 (a) and (b). Figure 31 (c) shows the printing result, i.e., 2x2 arrays of silicon squares on glass. Figure 32 shows a micrograph of the silicon ink used for transfer printing.

The printing cycle is completely automated. Instead of programming position into the printing cycle, contact events are detected. Using contact detection different phases of the printing cycles are executed by the controller.

3.7 Monitoring the micro transfer printing process

During a printing cycle, the two most common failures encountered are the failure to pick-up ink at the donor substrate and the failure to deposit the ink at the receiving substrate. Besides using the signals from the instrumented composite stamp to control the print cycle (as was discussed in the previous section), one also has an opportunity to use this information for deciding whether pick-up or printing at a particular post were successful during a print cycle. To do so, rudimentary Bayesian minimum-error classifiers are designed to discriminate between failures and successes during the pick-up and deposition phases of the print cycle. To build a Bayesian classifier, one needs to (1) identify the signals and the signal features on the basis of which to classify events, in this case, success or failure events during pick-up and printing, (2) collect training data samples of signals of different events and construct signal feature vectors, (3) use the training data to construct the classifier (or the discriminant function for the classifier), (4) assess the performance of the classifier on the training samples. If it is inadequate for the application, then return to step (1) and identify additional signals or signal features and repeat the process until adequate classification performance is obtained.

Separate classifiers for classifying events during pick-up and printing are developed. For signals, the delamination forces (see figure 27 (b), which defines it as the peak force or voltage signal that is produced when the stamp is withdrawn from the substrate) during pick-up or printing is used. The signal or feature vector is therefore a single value or a scalar. To start, this discussion focuses on classifying successful or failed pick-up events. Classification of successful and failed printing events is analogous, and will be briefly described at the end of this discussion. During normal operation, at pick-up, one of only two events occurs: i) if the anchors holding the ink to the donor substrate fail, then one has a successful pick-up. If the interface of the ink with the stamp fails, then one has a failure to-pick up. The classifier is designed to assign the pick-up event to one of these two classes. Other events like catastrophic failure of the stamp or the substrate can be detected by other means. Therefore, with a two-class classification problem, let ω_1 be the class representing pick-up events where the ink-substrate interface fails, i.e., successful pick-up events and ω_2 be the class that represents events where ink-stamp interface fails, i.e., unsuccessful pick-up events. Let X be the delamination force signal obtained during the pick-up event. Then the classification problem is: given that signal X is observed during a pick-up event, assign the event to the class of successful pick-up events, ω_1, or unsuccessful pick-up events, ω_2. The Bayes decision rule for minimum error is [53]:

$$P(\omega_1 / X) \geq P(\omega_2 / X) \Rightarrow X \in \omega_1 \qquad else \;\; X \in \omega_2 \tag{3.4}$$

The *a posteriori* probabilities, $P(\omega_i / X)$, of the signal X implying that an event belonging to class ω_i has occurred can be converted to expressions involving *a priori* probabilities, conditional density functions and mixture probability, $P(\omega_i)$, $P(X/\omega_i)$ and $P(X)$, using Bayes theorem. This produces:

$$\frac{p(X/\omega_1)P(\omega_1)}{P(X)} \geq \frac{p(X/\omega_2)P(\omega_2)}{P(X)} \Rightarrow X \in \omega_1$$
$$else \;\; X \in \omega_2 \tag{3.5}$$

or

$$\frac{p(X/\omega_1)}{p(X/\omega_2)} \geq \frac{P(\omega_2)}{P(\omega_1)} \Rightarrow X \in \omega_1$$
$$else \;\; X \in \omega_2 \tag{3.6}$$

When the conditional probabilities are Gaussian distributions, taking the natural logarithm of the ratio of conditional probabilities (called the likelihood ratio) produces a discriminant function given by:

$$\frac{1}{2}\left[\frac{(X-M_2)^2}{\sigma_2^2} - \frac{(X-M_1)^2}{\sigma_1^2}\right] + \ln\left[\frac{\sigma_2}{\sigma_1}\right] \geq \ln\left[\frac{P(\omega_2)}{P(\omega_1)}\right] \Rightarrow X \in \omega_1$$
$$else \;\; X \in \omega_2 \tag{3.7}$$

Where $N(M_1, \sigma_1)$ and $N(M_2, \sigma_2)$ are the Gaussian distributions representing successful and failed pick up and $P(\omega_1)$ and $P(\omega_2)$ are the *a priori* probabilities of success and failure in pick up. The training of the classifiers involves collecting data to estimate the parameters of the Gaussian distributions, M_i and σ_i, and the a priori probabilities, $P(\omega_i)$.Further, these estimates can be periodically updated with information collected during normal operation of the composite stamp.

For training of the classifier, force or voltage signal values for successful and failed pick-ups need to be collected. Noting that successful pick-up results when the anchor between the ink and donor wafer fails, the parameters of $N(M_1, \sigma_1)$ can be obtained by collecting signals during

successful pick-up of inks from the donor substrate. By recording the failed pick-up events during the training exercise, the *a priori* probabilities $P(\omega_i)$ of success and failure can also be estimated. Since the failure event during picking up occurs when the stamp-ink interface fails, the parameters for $N(M_2, \sigma_2)$ can be accessed from data in the adhesion tests reported in a previous section.

For testing this approach to using the signals from the instrumented composite stamp for process monitoring, we use 250 µm x 250 µm x 3 µm silicon chips as the ink, the image of the donor is shown in figure 32. For training the classifier, each post on the composite stamp was used to pick up 20 chips from the donor wafer and the force signals are recorded. These signals are used to estimate M_1 and σ_1, of the Gaussian distribution used to characterize ω_1 for each post. For obtaining M_2 and σ_2, of the Gaussian distribution characterizing ω_2, each post on the stamp is brought into contact with an unreleased chip and the stamp is withdrawn at a speed of 250 µm/sec.

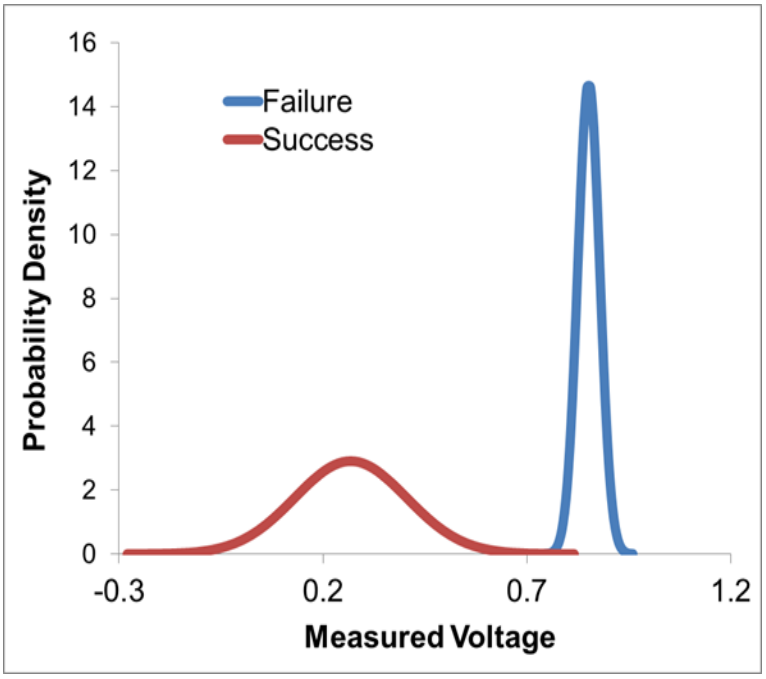

Figure 33: Plot of the two probability distributions of voltages representing peak delamination forces for successful and failed pick up of ink in a transfer printing. The distributions are calculated based on the mean and standard deviation calculated from the data captured on training samples.

Figure 33 shows the two distributions of signals from classes ω_1 and ω_2 for a typical post on the stamp, given by *N(0.852, 0.027)* and *N(0.268, 0.137),* respectively.

In the short training experiments, no failures were encountered. Failure to pick-up are usually associated with ink fabrication and occur when the undercut etch process does not completely release the ink from the substrate or when a photoresist anchor is over-exposed and becomes larger than designed. Therefore, for the a priori probabilities, $P(\omega_i)$, based on prior experience with the process, the threshold value (i.e., $P(\omega_2)/ P(\omega_1)$) was conservatively set to 0.02. The classifier for the post being used as an example therefore becomes from eq. (3.7):

$$\left[\frac{(X-0.268)^2}{0.0375}-\frac{(X-0.852)^2}{0.0015}\right]+1.62 \geq -3.91 \Rightarrow \textit{Successful Pick-up} \tag{3.8}$$

else, Failed Pick-up

The decision rule, tested on subsequent print cycles is shown in figure 34. Again, during the test run, no misclassifications were encountered.

In a similar manner, a Bayesian classifier is constructed for the printing or deposition event of the print cycle. Here, successful printing, class ω_1 corresponds to failure of the stamp-ink interface and failure to print, class ω_2, corresponds failure of the interface between the ink and the receiving substrate. The reasons for failure are (1) contamination on the surface of the receiving substrate, (2) incomplete release of the ink from the donor substrate that leaves behind asperities on the bottom surface of the ink, (3) surface defects on the receiving substrate. All these conditions prevent the ink for making full contact with the receiving substrate, resulting in a weak interface that fails when the stamp is withdrawn. The delamination forces vary widely, depending on the nature and size of the defect/contamination. Further, this is a rare event and therefore

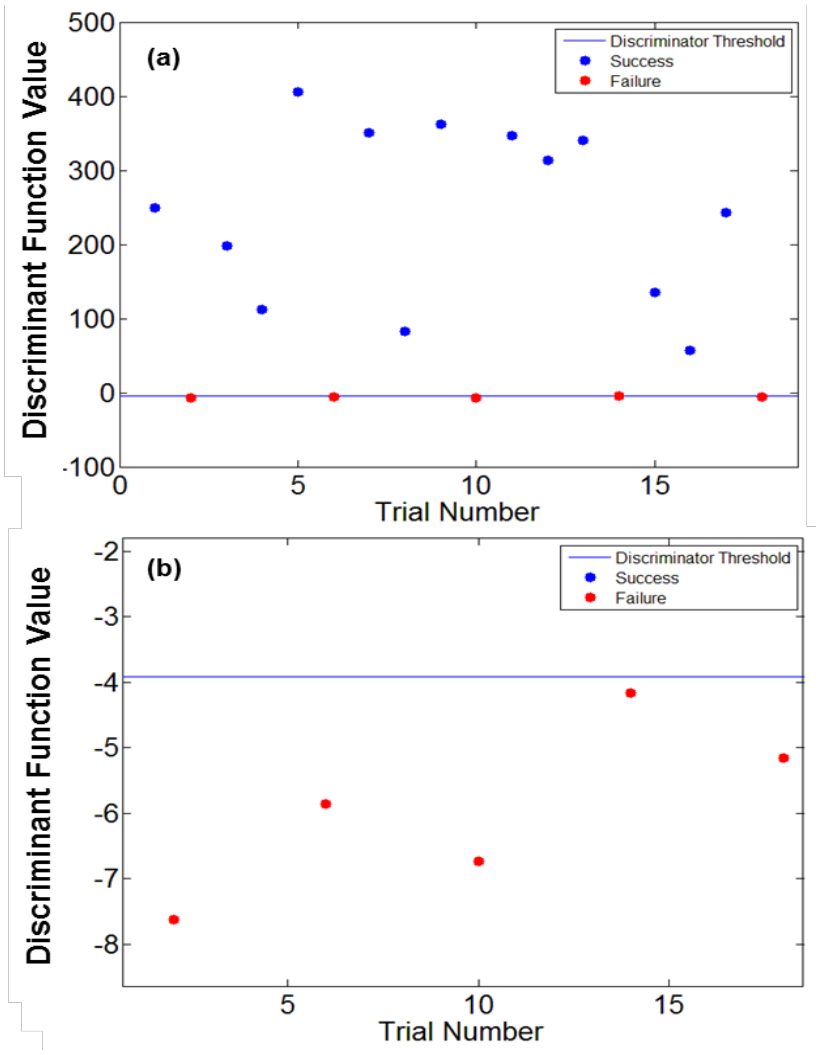

Figure 34: Plot of values calculated by the discriminant function based on the measured voltages during ink pickup. (a) Plot of calculated values for the entire data set. (b) Close up plot showing values of discriminant function for failure events in relation to the threshold.

difficult to characterize. However, the one feature that characterizes this class (failure to print) is that the delamination forces generated when printing fails are lower than the delamination forces when printing is successful (i.e., the ink-stamp interface fails). As we have seen, in the discussion on the design of the classifier for the pick-up phase of the cycle, the delamination force for ink-stamp delamination is easy to characterize. This, taken with the fact that delamination forces are always smaller when we have a failure to print and the difficulty in obtaining reliable distribution

parameters for the class of failure events leads us to develop a single-class classifier for this phase of the printing cycle. In the context of this work, this reduces to deciding outliers from the distribution that characterizes normal operation. We implement this as a one-sided hypothesis test, checking the Z-score of each observation of delamination force during printing with respect to the Gaussian distribution characterizing ω_1, the class representing successful printing events. The threshold of the Z-score is set to maintain the probability of a type-1 error (a successful printing event being classified as unsuccessful) to 0.025. The distribution for delamination force during successful printing is obtained by conducting adhesion tests at the printing speed (here, 50 µm/sec), similar to that described in a previous section, with unreleased chips on a donor substrate. If this distribution is characterized by *N(0.627, 0.003)*, then the classification test for successful/failed print is given by:

$$\frac{X - 0.627}{0.003} \leq -1.96 \Rightarrow Failed\ Print \tag{3.9}$$

else, Successful Print

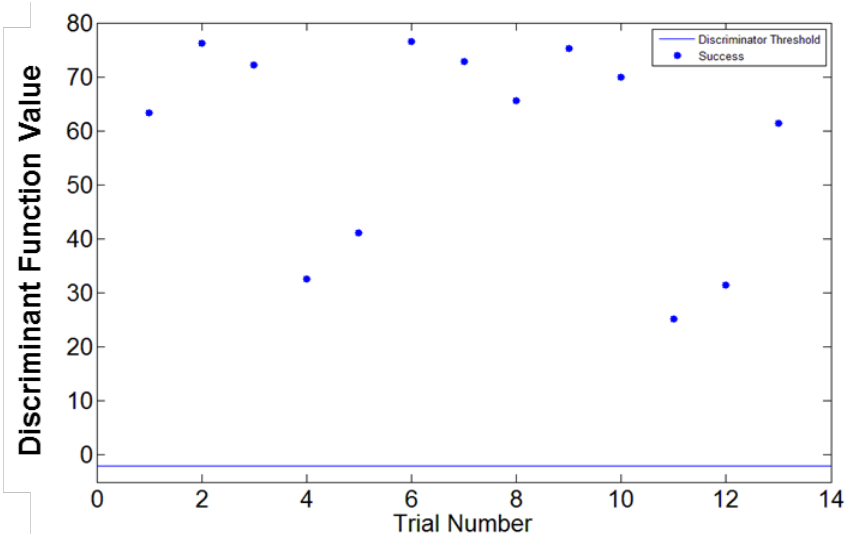

Figure 35: Plot of values calculated by the discriminant function during ink printing. The solid line represents the threshold value for discrimination.

Figure 35 shows a plot of values calculated by the discriminator based on the measured voltage for successful printing events. The classifier correctly classified all events. However, no failure events were encountered during the test.

3.8 Conclusion

A novel instrumented composite stamp design for micro transfer printing was presented. The composite stamp, comprised of four layers, embeds a strain gauge at each post on the stamp to provide the capability to observe the process at each printing site while, at the same time, emulating the mechanical behavior and interfaces of a bulk PDMS stamp. To realize this composite instrumented stamp, a new fabrication protocol that allows SU-8-based microfabrication on a PDMS substrate is developed. The protocol is designed to be a low-temperature process to limit the internal stresses produced in the SU-8 layers of the composite.

The fabricated stamps were characterized and shown to preserve important features (e.g., stiffness, dependence of adhesion forces on separation velocity) of bulk PDMS stamps. Further, the embedded strain gauge is demonstrated to have sufficient resolution to measure delamination forces. The instrumented composite stamps are shown to be capable of printing and performing in a manner similar to a bulk PDMS stamp. Using the capabilities of these stamps, a new sensor input driven print cycle has been developed to increase the robustness of the process to set-up errors. A process monitoring scheme involving a basic statistical pattern classifier is developed to analyze the force signals generated by the instrumented stamps so as to detect unsuccessful pick-up and printing events during an automated print cycle.

CHAPTER 4: ACTIVE COMPOSITE STAMPS FOR LOCALIZED ACTUATION AND SENSING

The driving motivation behind a stamp that preserves local process conditions for successful transfer printing, while providing the stamp with sensing and capability to adjust its geometry is to improve process robustness. Additionally, with local actuation capabilities, the stamp is able to provide process flexibility, permitting selective pick up or printing of microstructures in any pattern by appropriately actuating selected posts.

The above requires the integration of many different functions into the stamp, namely, a functional material for microstructure pick-up and release during micro-transfer printing, actuators for producing force/motion at the posts and sensors for measuring the force or the deflection, interconnects for bringing in power and extracting signals and structures for tuning the compliance to localize and direct the deformations in the stamp. The active composite architecture described earlier provides the foundation for integrating all these functionalities at the material scale with each function assigned to a constituent layer.

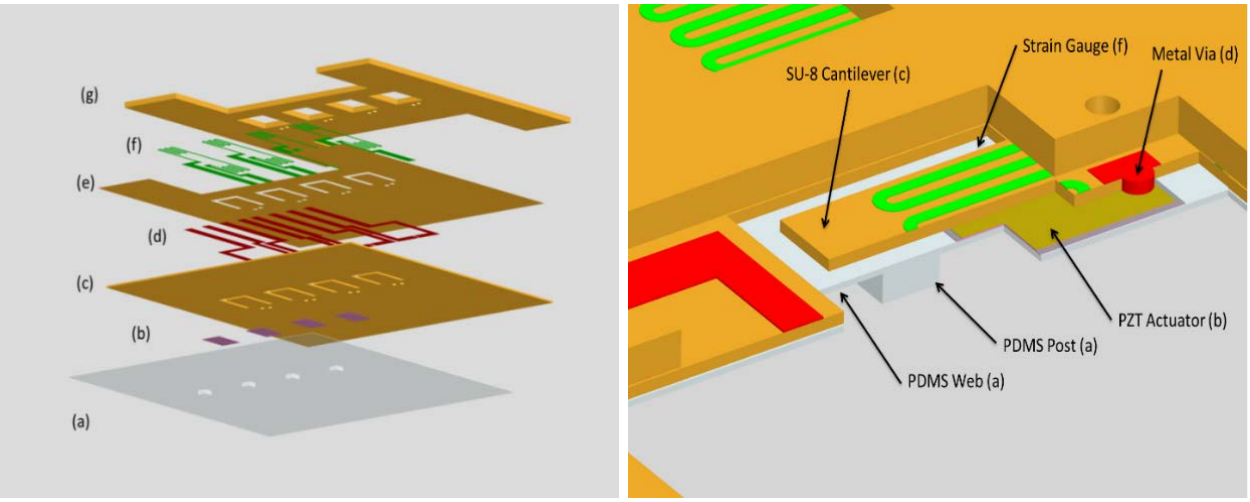

Figure 36: (Left) Exploded view of the solid model of the design showing the individual layers. (a) PDMS layer with posts, (b) PZT thin film placed for embedding actuation, (c) SU-8 structural layer providing selective compliance, (d) Metal interconnects, (e) SU-8 Encapsulation layer, (f) Metal strain gauge, compensation gauge and interconnects, (g) Handle layer. (Right) Close up view of a single post of active composite stamp showing the integration of the individual functional layers.

From a design methodology perspective, building upon the instrumented composite stamp architecture, the functional layer is composed of PDMS patterned with posts to replicate the geometry of a conventional micro-transfer printing stamp. The actuation layer is formed from a piezoelectric PZT layer that is first fabricated on a silicon growth substrate and then integrated into the polymer composite membrane using micro transfer printing. PZT was chosen based on its performance advantages and well as being a well characterized MEMS actuation material. A discussion on the various thin film materials for micro scale actuation is presented in appendix C. Stiffness tuning layer is constituted of cantilevers composed of SU-8; an epoxy based negative tone photoresist. The embedded sensor layer is a strain gauge integrated into the cantilever. A metallization layer for interconnects is below this layer. Finally, the stamp is completed with a thick handle layer made of SU-8 and patterned with windows to permit unrestricted deflection of the cantilevers and optical viewing from above the stamp (required for alignment and registration). Figure 36 shows a solid model of the active composite material based stamp exhibiting how the individual function layers are integrated into the stamp.

4.1 Active composite stamp design

The above selection of materials is based on function, but also compatibility with the fabrication strategy that was developed for the instrumented composite stamp. With this selection of materials, the dimensions i.e. thickness of the layers and lateral dimensions of features such as the cantilevers and the PZT actuators, the location of the PZT actuator relative to the cantilever and the PDMS post can be arrived at by using finite element analysis (FEA). The dimensions of the PZT membrane and the dimensions of the cantilevers were calculated using the FEA. Fabrication constraints on the thickness and dimensions of the layers in the composite were also

considered to create a search space; from which appropriate dimensions to obtain a minimum stiffness and deflection of 150 N/m and 5 µm, respectively at the printing posts were arrived at. Based on fabrication constraints the thickness of the PDMS layer and the location of the PZT layers were constrained. The thickness of the PDMS layer was set at 20 µm which is the thinnest layer that can be reliably spun coated while having PDMS posts with dimensions of 250 µm x 250 µm, 100 µm tall. The thickness of the sol-gel based PZT film was determined by the availability[1] of Silicon wafers with appropriate thin film layers (namely Platinum, PZT and Silicon Dioxide). A 0.5 µm thick PZT layer is embedded into the SU-8, at the SU-8/PDMS interface. The location of the PZT within the composite membrane was constrained by micro transfer printing requirements. The PZT actuator has bottom platinum and top gold layers, forming the two electrodes and need to be accessed for the purpose of supplying power. For a piezoelectric sheet, the poling direction (usually along the thickness) is designated as the 3-axis with axes 1 and 2 in the plane of the sheet. If the piezoelectric coefficients defining strain per unit electric field at constant stress are d_{ij}, then d_{31}, d_{32} and d_{33} represent the normal strain induced in the 1, 2 and 3 direction respectively, due to an electric field applied in the poling direction. Assuming transverse isotropy we have $d_{32} = d_{31}$. PZT based actuation of a cantilever structure can be characterized into two categories, namely longitudinal or d_{33} and transverse or d_{31} type; depending upon the direction of applied field and resulting strain. In a d_{33} type cantilever, an in-plane electric field induces an in-plane strain, which contracts or expands the PZT material [54, 55]. In a d_{31} type cantilever, the applied electric field is normal to the cantilever and the in-plane expansion or contraction is used to generate deflection of the cantilever. The former (d_{33}) requires the use of two metal interdigitated

[1]MEMS Solution Inc., Republic of Korea.

electrodes (IDE) on top of the piezoelectric film [56], while the latter (d_{31}) uses two sheet electrodes on the top and bottom of the piezoelectric film. Given the configuration of the PZT films, described above, our work uses the d_{31} actuation mode.

A three dimensional multiphysics based FEA model of a single cantilever was made to calculate the required dimensions of the various layers to meet design requirements. The FEA was done using the piezo solid application mode within the MEMS module of COMSOL Multiphysics® software (version 3.5a). An image of the model geometry is shown in figure 37. The bottom most layer in the model is a 20 µm thick layer of PDMS with a 250 µm x 250µm, 100 µm tall post, forming the PDMS membrane, the edges of the membrane are constrained to be fixed. The dimensions of the membrane are to be determined. A 0.5 µm thick layer of PZT is bonded on top of the PDMS membrane. The lateral dimensions of this membrane are to be determined. The next layer of the model is an SU-8 layer, forming the cantilever. The SU-8 cantilever is bonded to the PZT and PDMS. The base of the SU-8 cantilever is constrained. The final dimensions of the cantilever are to be determined using FEA. The elastic modulus of SU-8 used in the simulation

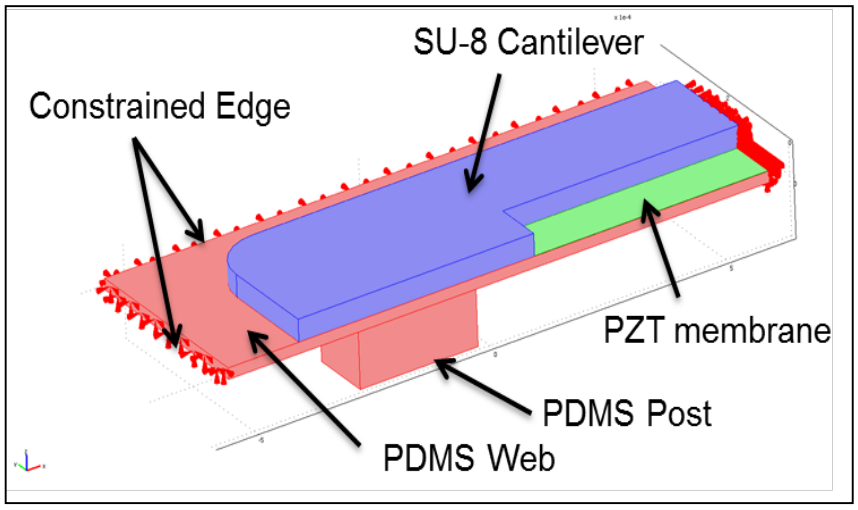

Figure 37: Isometric view of a half section of the FEA model, showing the PDMS web and post, the SU-8 cantilever, location of the PZT membrane and the constrained edges of the PDMS web.

was 4.02 GPa [57], the elastic modulus for PDMS was 2.0 MPa, and the PZT material properties such as the compliance, piezoelectric coupling used in the simulation were that of PZT-8 [58].

In the search for appropriate dimensions, first a force was applied to the face of the PDMS post, with no voltage applied across the PZT (top and bottom surface of the PZT were given ground electrical boundary conditions). The deflection of the cantilever and post under applied load was calculated, the thickness of the SU-8 layer in the composite and the lateral dimension of the cantilever and PDMS web were varied to get the desired stiffness. Next, voltage was applied to the PZT and deflection of the cantilever and post was calculated. The dimension of the PZT, SU-8, and PDMS were again varied to achieve the desired deflection and the iterations were continued until both design criteria were met. Constraints such as limitation on dimensions originating from fabrication processes were considered throughout the design process.

The dimensions of the PDMS web, the PZT membrane, and the SU-8 cantilever were calculated to be a length of 1000 µm and a width of 900 µm, a width of 600 µm and a length of 500 µm , and a width of 650 µm , a length of 900 µm respectively. The thickness of the SU-8 cantilever was calculated to be 40 µm. Figure 38 (a) shows a typical profile of the stamp when actuated and figure 38 (b) shows the FEA computed stamp deflections (at the face of the post) as a function of applied actuation voltages. A maximum deflection of about 7.5 µm at the face of the PDMS post is predicted for an applied voltage of 18V with an actuation constant of 0.417µm/V. A typical deflection profile of the stamp when a force is applied at the post is shown in figure 38 (c), while figure 38(d) shows the computed deflection at the post as a function of the applied force. The stiffness of the overall composite stack can be observed to be about 150 N/m for the designed dimensions.

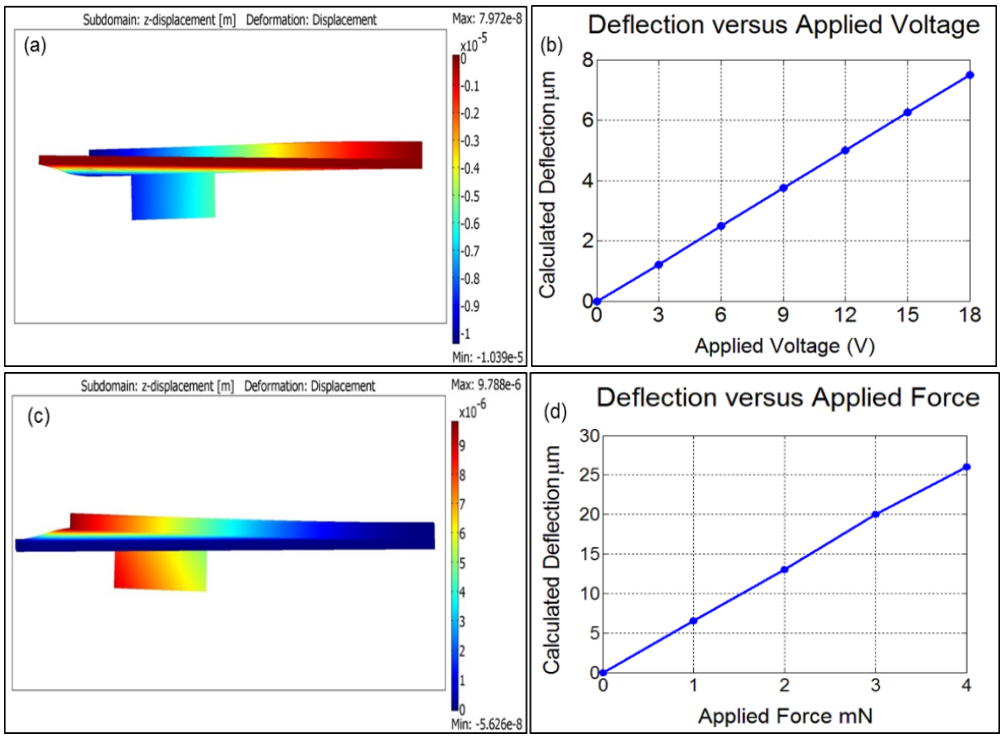

Figure 38: Results of FEA performed to calculate stamp deflection under actuation and applied forces. (a) Representative FEA computed deflection under actuation. (b) Graph of computed deflection at the post for various applied actuation voltages. The maximum deflection is 7.5 µm. (c) Representative FEA computed deflection when a force is applied at the post. (d) Calculated deflection at the post for various applied forces. The calculated stiffness is 150 N/m.

4.2 Active composite stamp fabrication

This section presents the details of the fabrication process used to create the PZT ink, and the active composite membrane stamp. All processes were done at a temperature of 75 ^{o}C to reduce thermally induced internal stresses [59].

4.2.1 PZT ink fabrication:

The individual PZT elements, embedded into the composite membrane stamp, consists of a layer of PZT (500nm) sandwiched between a top (Au/Cr, 200nm/5nm) and a bottom (Pt/Ti,

200nm/20nm) electrode. The dimensions of each PZT element are 600x 900 μm^2, slightly longer than the value calculated from the FEA to allow for placement of contacts. These PZT elements, are fabricated from a multilayer stack of $Pb(Zr_{52}Ti_{48})O_3$/Pt/Ti/SiO_2 (500nm/200nm/20nm/600nm) thin films on Si (100) wafer (MEMS Solution Inc.). The top electrode is composed of 200 nm thick gold on top of 5 nm thick seed layer of chromium, deposited by Electron Beam Physical Vapor Deposition on the PZT surface. After deposition of gold top electrode, the PZT is poled at 150 ^{0}C using a 100 kV/cm electric field, applied normal to the plane of the PZT for 1 hour.

After poling, the multilayer structure is patterned into arrays of individual units for use in micro transfer printing following the general process outlined in appendix B. First the top electrode is patterned using a photoresist (AZ4620) etch mask; patterned using photolithography. This is followed by etching of the gold layer by gold etchant (Transene Company Inc., TFA), and chromium layer by CR-7 chrome etchant (OM Group, USA), respectively. Similarly the PZT and Platinum are patterned by etching in a 4.5:4.5:91 v/v solution of HNO_3 (Nitric Acid, 70%): Buffered Oxide Etch (BOE, 6:1): Deionized Water (H_2O), and a 4:1 v/v solution of Hydrochloric acid (HCl, 37%): Nitric acid (HNO_3, 70%) at 95 ºC, respectively [60].

After the individual inks are fabricated, they are protected by photoresist (AZ4620) and undercut etched in 3:1 v/v solution of Deionized Water (H_2O): Hydrofluoric acid (HF, 49%) for

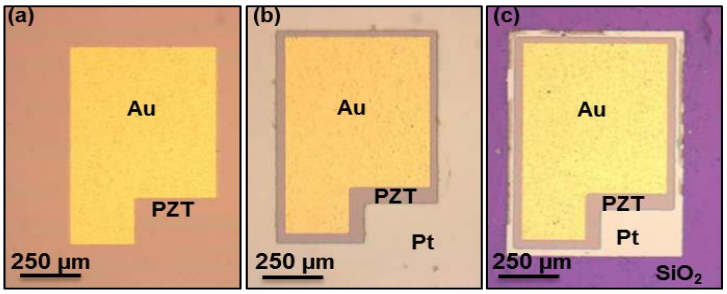

Figure 39**:** Fabrication of PZT ink for transfer printing. (a) Gold patterning after deposition. (b) PZT etching. (c) Pt etching.

twenty minutes to partially undercut the Silicon Dioxide layer underneath the Platinum. This helps to release the ink from the edges (100 μm on each side) and allows them to be easily detached from the silicon substrate and transferred during transfer printing. Images of the individual fabrication steps are shown in figure 39.

4.2.2 Active composite stamp fabrication:

The fabrication approach presented here builds upon on the design and fabrication of the instrumented composite stamps for micro transfer printing presented in chapter 3 [61]. The first layer is a functional layer made of PDMS spun coated onto a mold to form a PDMS (20 μm thick) web that carries the posts. The active composite material; consisting of PZT and spin cast SU-8 (40 μm thick) is integrated on top of the PDMS followed by patterning the individual cantilevers and the die. Metal contacts (Ti/Cu, 10nm/500nm) and measurement and compensation metal strain gauges (Ti/Au, 10nm/50nm) are patterned on top of the SU-8. Finally a thick SU-8 (200 μm) layer is spun cast and patterned to form the handle layer of the stamp, providing rigidity for ease of handling and mounting.

Fabrication begins with the manufacturing of a SU-8 master mold, used to mold the PDMS layer. A 100 μm thick film of SU-8 50 (Microchem Corp.) is spun on to a polished silicon wafer and photolithographically patterned with square holes (for the printing posts on the PDMS layer). Before PDMS casting, the surface of the mold is coated with a thin layer of Polytetrafluoroethylene (PTFE), deposited using an Inductively Coupled Plasma Deep Reactive Ion Etching (ICP-DRIE) machine (PlasmaTherm, SLR 770) to prevent the PDMS from sticking to the mold and to facilitate eventual de-molding after fabrication is completed. A 20 μm thick PDMS (Dow Corning Corp.,

Sylgard 184) layer is spun coated onto the mold. The PDMS is semi cured in an oven at 70ºC for 30 minutes.

Metal-sandwiched PZT membrane 'inks' (whose fabrication was described earlier) are micro-transfer printed into specific locations on the semi-cured PDMS membrane, still on its SU-8 mold. Following the scheme depicted in figure 10, a PDMS stamp with patterned posts is used to make contact with the PZT ink, extract them from the donor silicon handle substrate, and place them at predetermined locations on the PDMS membrane. Figure 40 (a) shows a close up of a

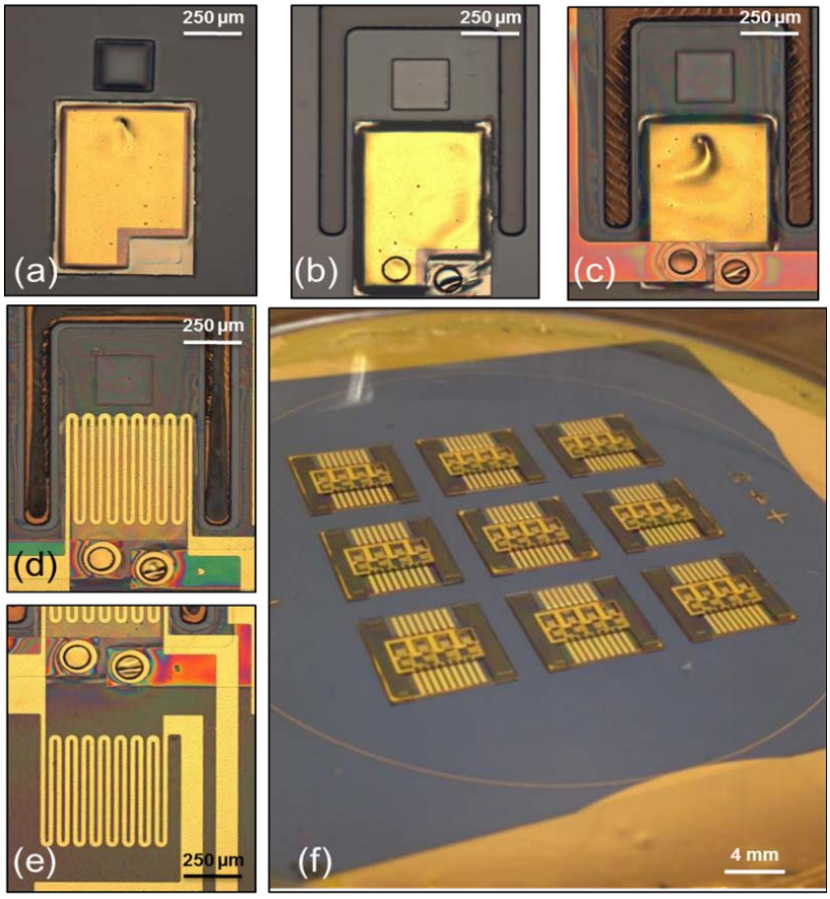

Figure 40: Fabrication of the active membrane composite stamp. (a) PZT actuator ink transfer printing. (b) SU-8 structural layer photolithography. (c) First metal interconnect layer formation and passivation. (d) Second metal layer fabrication forming the sensing and (e) compensation strain gauges and interconnects. (f) Image of a single wafer with nine individual stamps.

single PZT ink printed onto its target location. After transfer printing, the PDMS is fully cured at 70 ^{o}C for 24 hours in an oven. After fully curing, the PDMS surface is functionalized with a self-assembled monolayer (SAM) containing an amino group. To do this, the PDMS surface is first activated using an O_2 plasma in a Reactive Ion Etching (RIE) machine (March, CS-1701). Then the activated PDMS is soaked into a 1% v/v solution of (3-Aminopropyl)triethoxysilane (Sigma-Aldrich Corp., APTES) and methanol for 15 minutes, and then dipped in methanol for 2 minutes to desorb the excess APTES. This leaves behind a SAM on top of the PDMS which acts as an adhesion promoter for SU-8, facilitating SU-8 based micro fabrication on top of a PDMS substrate and permanently bonds the PDMS and SU-8 together, based on the reaction of the amino group of the SAM with the epoxy group of SU-8.

A 40 μm thick layer of SU-8 50 is spun coated on top of the PDMS/PZT, embedding the PZT into the polymer. The SU-8 layer is patterned to form the cantilever structures, once again using photolithography. The overlay registration is such that the posts in the PDMS are located under the free ends of the cantilevers. Thus, this layer provides the composite with selective compliance for locally actuating the printing posts. Via holes patterned in this layer allow for routing of electrical connections to the PZT actuator electrodes.

After fabrication of this layer, a 10 nm layer of Titanium followed by a 500 nm layer of Copper is sputtered using a vacuum sputtering tool (AJA International Inc., ATC Series). After sputtering, the contacts are formed by spin coating and patterning a photoresist (AZ 5214E) etch masks and etching the copper using copper etchant (Transene Company Inc., CE-100) and Titanium using BOE (Buffered Oxide Etch 6:1); forming the first level interconnects.

After the first level interconnects are patterned, a passivation layer of 5 μm thick SU-8 5 (Microchem Corp.) is spun coated and patterned. A layer of 10 nm thick Titanium followed by 50 nm thick Gold is sputtered on top of this passivation layer. After sputtering, the strain gauges used for sensing along with a co-located compensation resistor and their contacts are patterned by spin coating and patterning a photoresist (AZ 5214E) etch mask and etching the Gold and Titanium layers; forming the sensing layer in the composite, consisting of measuring strain gages, compensation gauge and interconnects.

After the sensing layer is formed, a 200 μm thick layer of SU-8 100 (Microchem Corp.) is spin coated and patterned to form the handle layer of the stamp forming individual dies, providing it with rigidity for ease of handling and mounting. Figure 40 shows micrographs of a single post and cantilever of the active membrane composite stamp during various stages of fabrication.

After fabrication the PDMS layer around the stamp die is cut, the individual dies are then released from the mold by separating the PDMS from the mold at one corner with a sharp blade and gently peeling it away from the mold. Figure 41 (a) shows the image of a released die with an array of 4 actuated posts. After release from the fabrication substrate, Anisotropic Conductive Film (3M Corp., ACF) is bonded to the contacts and the membrane die is attached to a glass slide using

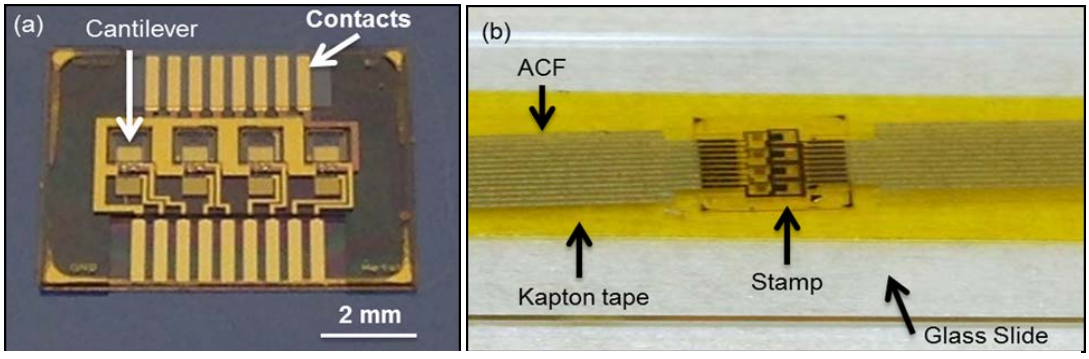

Figure 41: (a) Image of a released stamp. (b) Image of a single stamp with array of four actuated posts attached to a glass slide with ACF connections.

double sided polyimide tape (Kapton tape), forming the final stamp. The image of a completed, interfaced stamp is shown in figure 41(b)

4.3 Active composite stamp characterization

The individual actuated printing posts are mechanically tested for their stiffness, actuation capabilities and sensitivity using the calibration and testing setup described in section 3.2.1 Custom calibration and testing setup. Figure 42 shows the schematic, along with an image of the experimental setup.

The stamp being tested is mounted in the stamp holder of the transfer printing tool. The mounted stamp is interfaced with signal conditioning and drive electronics. The strain gages on the stamp are connected to Wheatstone bridges, whose output is amplified by a factor of five hundred using an instrumentation amplifier. The amplified signal is then collected using a data acquisition system (National Instruments, USB-6009). The digital signal is then fed into the transfer printer's interface software. The PZT actuators are connected to drive circuits that provide the high voltage for moving the individual posts.

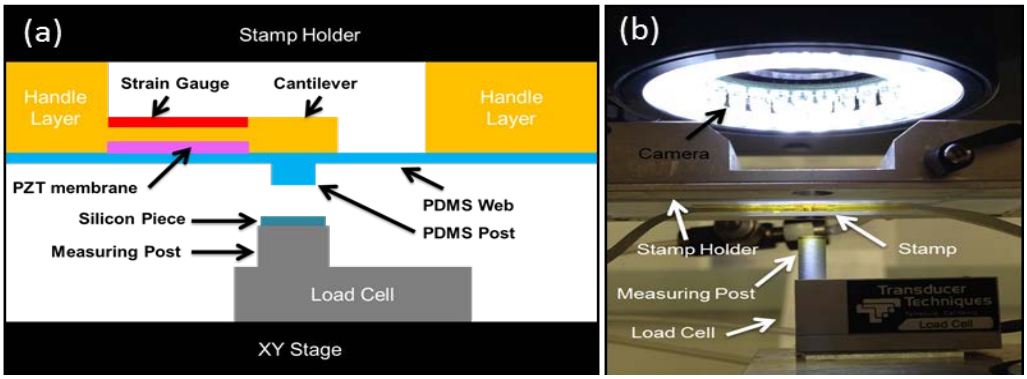

Figure 42: Schematic of the experimental setup used for characterization of the active membrane composite stamp. (b) Image of the experimental setup used for characterization of the active membrane stamp.

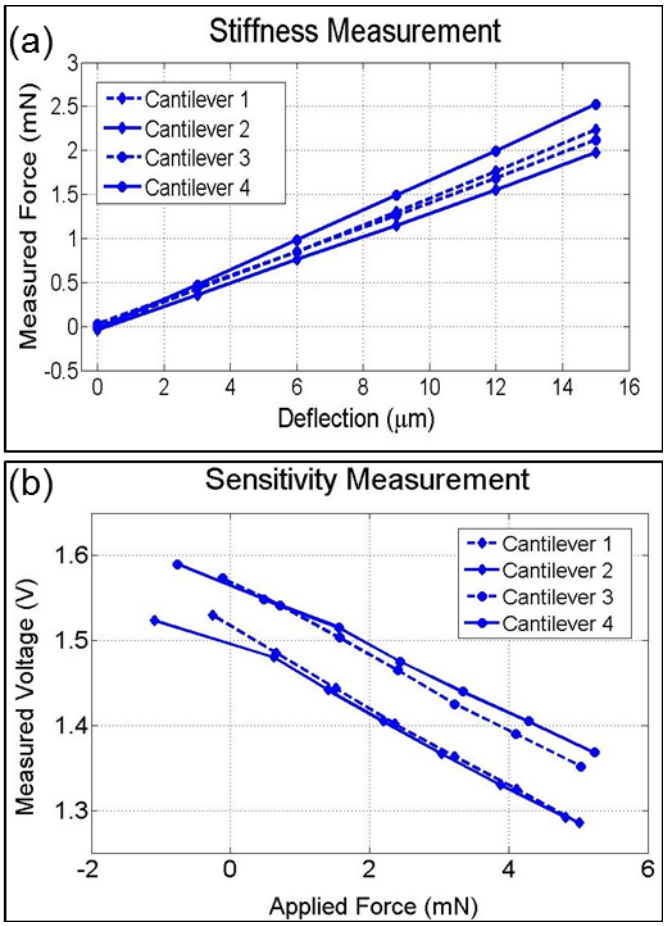

Figure 43: Graph of measured forces as a function of deflection of (the cantilevers and posts in) the active membrane composite stamp when each of the 4 posts is pressed against the silicon substrate. (b) Graph of measured voltage output from the bridge circuit (for each of the cantilevers) plotted against the applied forces at each of the corresponding posts.

4.3.1 Stiffness measurement:

To measure the stiffness of the stamp, the post on each of the cantilevers is brought into contact with the silicon attached to the load cell. The z-axis or vertical axis of the printer (to which the stamp is attached) is moved downwards through a known displacement (here 3 micrometers). Because the post and the cantilever in the stamp are the only compliant elements in the set-up, the displacement of the z-axis is accommodated by the local compliance of the stamp obtained as a

result of the deflection of the SU-8 cantilever behind the post. Thus, the programmed displacement represents the deflection of the cantilever. The resulting force applied to the load cell is recorded to produce force versus displacement curve for each of the posts of the active membrane composite stamp in contact with the silicon. Figure 43 (a) shows the force-deflection curves for the four posts. Each measurement is repeated 5 times. The average stiffness of the composite cantilever and post structures was measured to be 148.5 N/m with a standard deviation of 13.7 N/m. The measured stiffness is very close to the value of 150 N/m, computed using FEA of the designed stamp.

4.3.2 Sensitivity measurement:

During the stiffness measurement, where the stamp is deflected and forces measured, the voltage output from the bridge circuit of the strain gages was also recorded. Using the applied force versus measured output voltage information, the sensitivity of the individual cantilever was calculated. Figure 43 (b) shows the force-voltage relationship for the four cantilevers of the array. The average sensitivity was measured to be 42.6 mV/mN with a standard deviation of 0.03 mV/mN.

4.3.3 Actuation measurements:

The actuation of the individual posts was also measured during characterization. Voltage is applied to each cantilever and the deflection produced at the PDMS post measured. To measure the deflection, the PDMS post is brought into contact with the Silicon piece attached to the load cell. The location of the z-axis at which contact is detected is recorded as the zero position $\boldsymbol{Z_0}$. The PDMS post is then moved away from the Silicon by moving the z-axis of the machine. Next a voltage, *V*, is applied to the piezoelectric actuator and the z-axis of the machine is moved towards the Silicon until contact is detected. This location of the z-axis is recorded as the deflected position

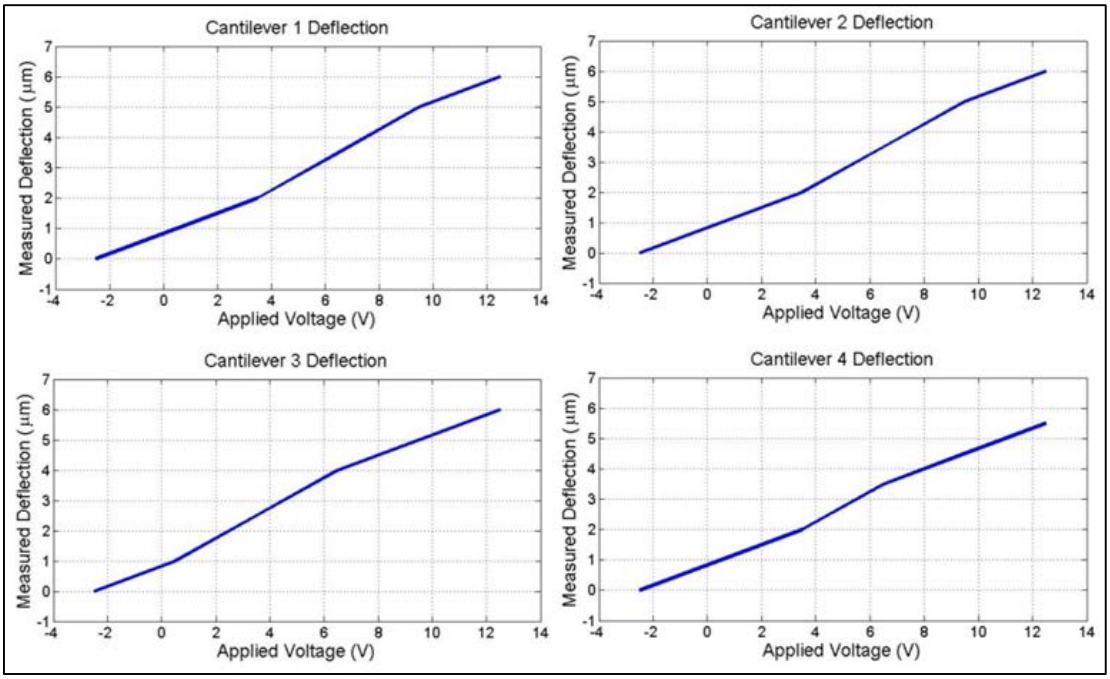

Figure 44: Measured deflection versus applied voltage graphs for four posts of the active membrane composite stamp. The average measured actuation was 0.4 μm/V

Z_v corresponding to an actuation voltage *V*. The difference $Z_v - Z_0$ gives the post's deflection for the applied voltage *V*. Following this method the deflections for a series of applied voltages are measured. Six different voltages were applied with the magnitude of -2.5, 0.5, 3.5, 6.5, 9.5 and 12.5 Volts. The total deflection measured for this range of inputs was 6 μm. Figure 44 shows graphs of deflection versus applied voltage data collected for the four posts. The measured actuation constant is about 0.4 μm/V, in good agreement with the 0.417μm/V computed from the FEA model of the stamp. The slight difference can be attributed to the actual material properties of the PZT being slightly different (smaller piezoelectric coefficients) from those used in the FEA.

4.3.4 Actuation sensing

The ability of the stamp to sense actuation was also measured as part of the characterization process. Using a function generator a 12.5 V peak-to-peak, 1 Hz sine wave signal was applied to

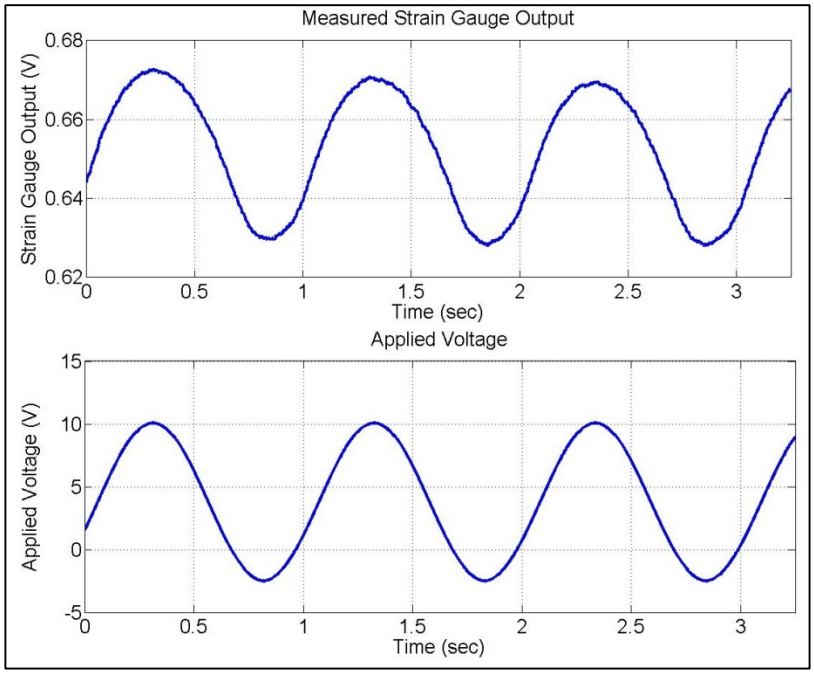

Figure 45: Strain signal measured using the embedded strain gauge for an applied sine wave with peak-to-peak voltage of 12.5 V and frequency of 1 Hz.

the PZT, to actuate the post. The resulting change in resistance in the strain gauge; due to the strain caused by the actuation, was sensed as a voltage change using the Wheatstone bridge. Figure 45 shows the plot of the waveforms for the collected signal and the applied voltage for a single post. The measured peak-to-peak voltage is 40 mV corresponding to approximately 5 μm deflection of the post.

4.4 Transfer printing experiments

To demonstrate a practical application of the active composite stamp, it was used to perform selective printing of silicon chips (‘ink’) in the automated transfer printing machine. To perform transfer printing, a single active membrane stamp with 4 posts was mounted onto the transfer printer (to the Z-axis or vertical axis), and two of the posts were interfaced with the drive circuitry. To demonstrate transfer printing we picked up and printed a 2x3 array of silicon squares

250 x 250 µm and 3 µm thick. The silicon squares have a center to center pitch of 300 µm on the donor wafer. They were picked up by two cantilevers with a pitch of 1500 µm. The silicon chips were selectively printed by actuating the two cantilevers individually and printed at a pitch of 350 µm.

Figure 46 shows a schematic representation of the individual process steps. The process steps are as follows. Step 1: Alignment of the PDMS posts on the cantilevers with the ink. Step 2: Both posts 1 and 2 are actuated before moving the z-axis down to make contact between the PDMS posts and ink. Here only posts 1&2 will make contact and be 'inked'. Posts 3and 4 remain 'uninked'. Step 3: Retrieval of the ink by posts 1 and 2 when the z-axis is retracted. Step 4: Translation to the receiving substrate. Steps 5&6: Actuation of post 2 brings the first silicon chip

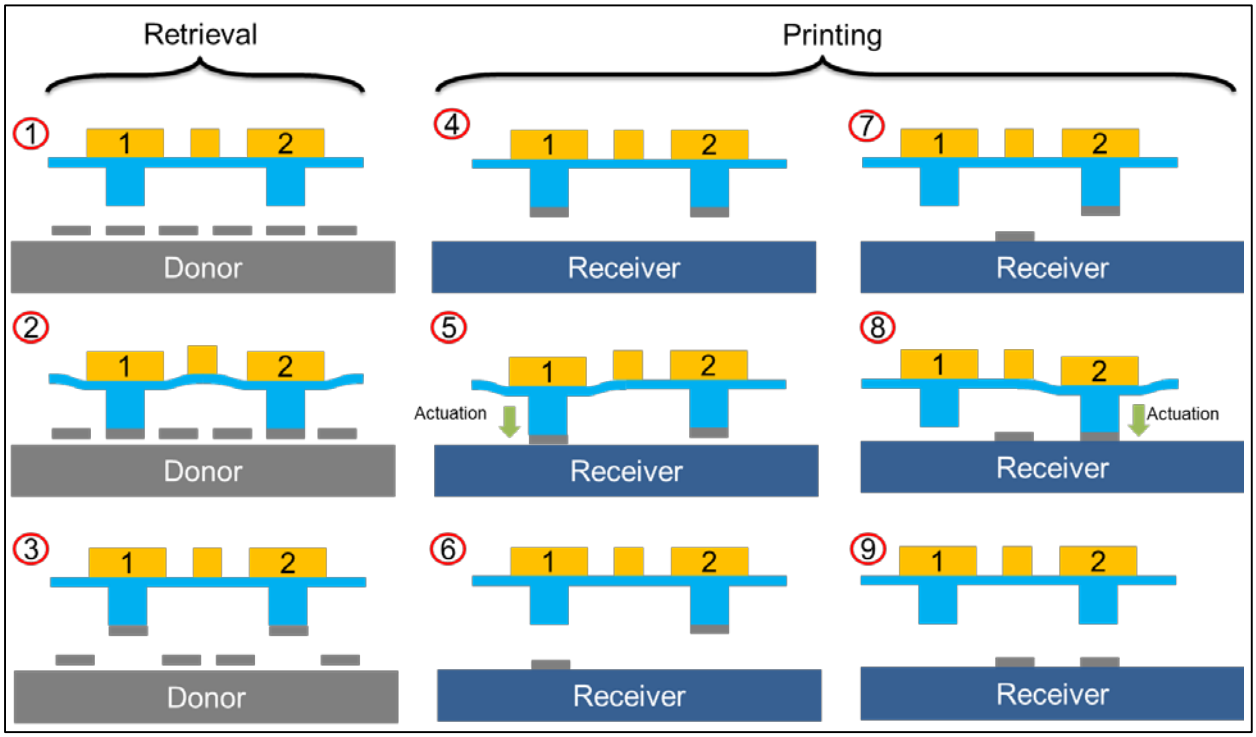

Figure 46: Schematic representation of micro transfer printing using two posts from an array of four of the active membrane composite stamp. (Steps 1-3) alignment and retrieval of silicon chips from donor wafer. (Steps 4-9) Translation, alignment and selective printing of individual silicon chips; using actuation of individual posts.

in contact with the receiving substrate. Subsequent retraction of the z-axis results in printing of the first silicon chip. Step 7: Translation of the stamp. Step 8&9: Actuation of post 1 brings second silicon chip in contact with the receiving substrate. Subsequent retraction of the z-axis results in printing of the second silicon chip. After both the chips are printed, the cycle is then repeated starting from step 1.

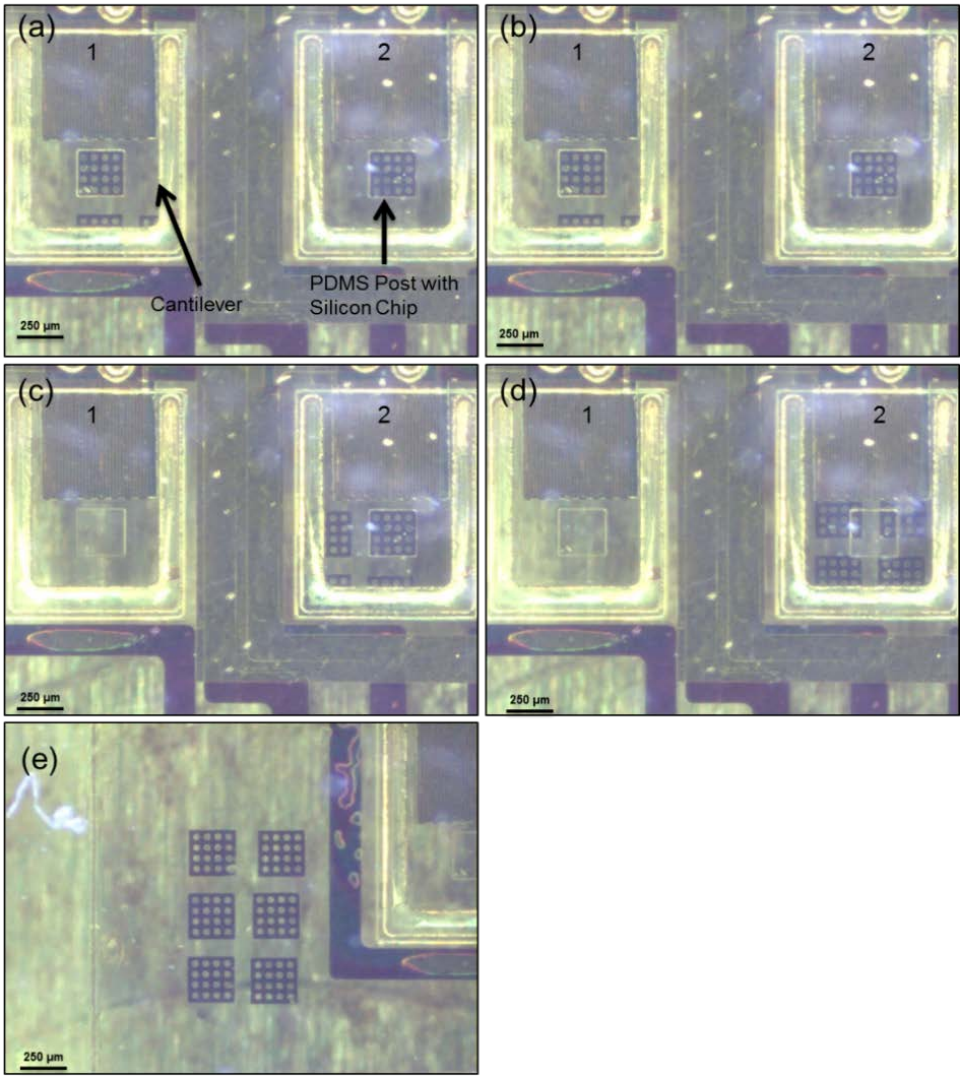

Figure 47: Image of the active composite cantilever array during transfer printing. (a) Both cantilevers are shown over the receiving substrate with ink attached to their respective PDMS posts. (b) Cantilever '1' actuated and making contact with the substrate surface, (c) image showing the array translated after the silicon chip from cantilever '1' was selectively printed (the PDMS post for cantilever '1' does not have silicon chip attached to it) (d) image showing both cantilevers after successful printing of their respective silicon chips. Also the printed chips can be seen through the cantilevers. (e) Shows the final array with a pitch much smaller than the pitch of the individual cantilevers achieved through selective printing

Figure 47 shows images captured during the course of the experiment. The frames show steps 4 to 9 as represented in figure 46. Figure 47 (a) shows two posts of the active membrane composite stamp with attached silicon chips over the receiving substrate (figure 46, step 4). Figure 47 (b) shows cantilever '1' actuated and contacting the receiving substrate surface. Figure 47 (c) shows the two cantilevers after silicon chip from cantilever '1' has been deposited and the array is translated to print with cantilever '2' (figure 46, step 7). Figure 47 (d) shows both cantilevers after their respective chips have been printed (Figure 46, step 9). Figure 47 (e) shows the image of the final printed array of silicon chips after the selective printing cycle has been executed 3 times. Notice that the pitch at which the devices were printed is much smaller than the pitch of the cantilevers; resulting in the ability to selectively print ink using the individually actuated cantilevers.

4.5 Closed loop control setup and experimental results

Piezoelectric materials typically suffer from creep and drift. To allow for reliable operation closed loop control is desirable. To achieve closed loop control, first the active composite stamps need to be calibrated. For this an improved characterization technique to allow for calibration of all four cantilevers within the same setup was developed. The improved calibration process employs visual observation along with sensor readout. A two megapixel camera with a 24x objective is used to observe the stamp side-on. The camera is equipped with focus and zoom optics and translational stages for X, Y and Z motion. Figure 48 shows the image of the optical calibration setup.

For calibration first the camera is focused onto the post of one of the cantilevers on the stamp; which is to be calibrated. Actuation voltage is applied to the PZT, the deflection of the post

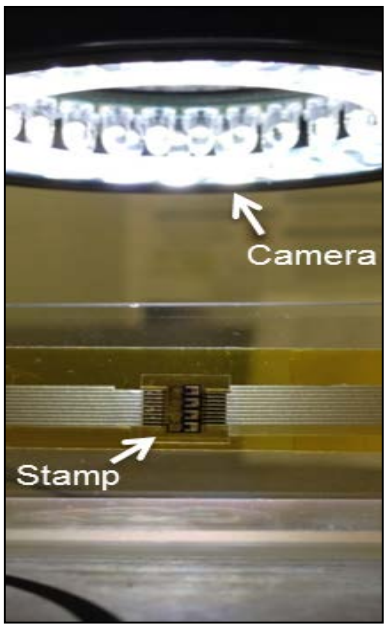

Figure 48: Image of the calibration setup showing the stamp and the camera used to observe the cantilever deflection.

along with the readout from the strain gauge are recorded. The actuation voltage is varied to get the static actuation and sensing characteristics of the cantilever. Once the cantilever is calibrated, the camera is focused onto the next cantilever and the process is repeated. Using this method static calibrations on all four cantilevers were performed. The visual observation method allows us to measure 0.5 µm motion of the post.

Figure 49 shows the two graphs obtained for a single cantilever during the calibration process. Figure 49 (a) shows the relationship between the measured sensor output voltage V_m versus mechanical deflection, d. Figure 49 (b) shows the relationship between the mechanical deflection d and applied actuation voltage V_d.

Approximating with an LTI-model the deflection d of the composite cantilever versus the applied voltage V_d can be characterized by a static gain K, such that,

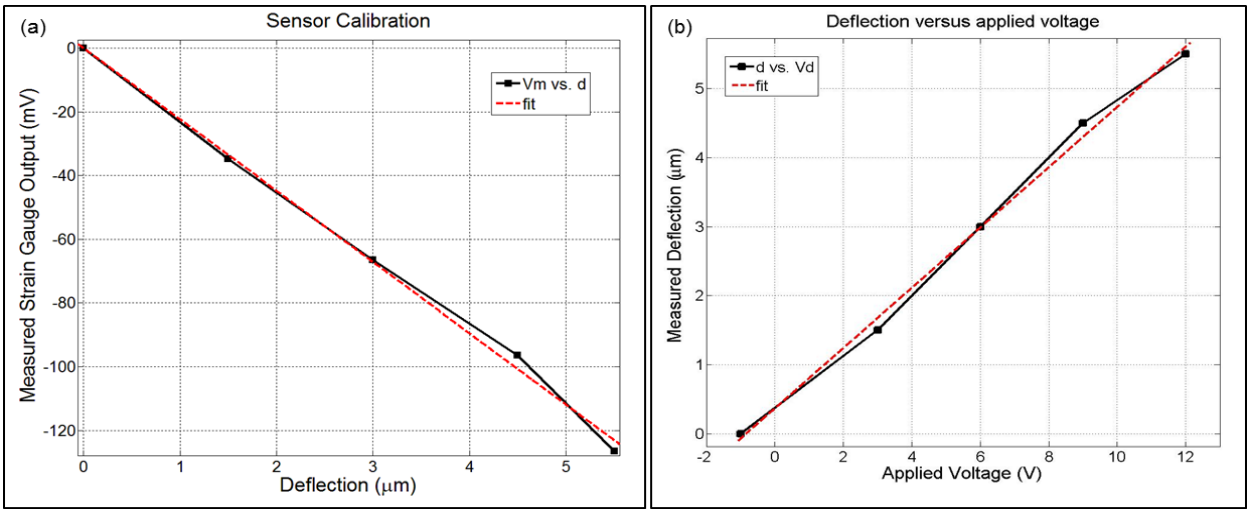

Figure 49: Calibration curves captured for a single active composite cantilever. (a) Measured strain gauge voltage versus post deflection curve. (b) Measured post deflection versus applied actuation voltage. The red dashed line shows the linear fit used to obtain the model

$$d = KV_d + c_1 \tag{4.1}$$

Similarly, the measured strain gauge output voltage versus mechanical deflection is given by,

$$V_m = Ad + c_2 \tag{4.2}$$

Using a linear fit, the values of K, c_1, A, c_2 are found to be 0.4368, 0.3667, -22.4 and 0.1074 respectively.

Assuming that a single post on the active composite membrane stamp behaves as a unimorph cantilever, for a cantilever characterized by its length L, thickness t; a theoretically linear relationship between the displacement and applied voltage is obtained [62]:

$$d = \Delta \frac{3L^2}{2t} d_{31} E_3 \tag{4.3}$$

Where, d_{31} is the piezoelectric coefficient, E_3 is the applied electric field and Δ is a geometric constant given by,

$$\Delta = \frac{\boldsymbol{2AB1 + B^2}}{\boldsymbol{A^2B^4 + 2A(2B + 3B^2 + 2B^3) + 1}} \tag{4.4}$$

With,

$$A = \frac{Y_e}{Y_p} \tag{4.5}$$

$$B = \frac{h_e}{h_p} \tag{4.6}$$

Here, Y is the elastic modulus and h is the layer thickness. The subscripts 'p' and 'e' denote the piezoelectric and elastic layers of the cantilever structure.

From eq. 4.3 it is easy to note that the deflection of the post is linear with respect to the strain produced in the piezoelectric layer. However the strain itself within the PZT layer is highly nonlinear with respect to the applied voltage. Thus the deflection profile of the cantilevers themselves will behave nonlinearly. To test this we applied a 20 V peak-to-peak triangular waveform voltage to the PZT layer and recorded the deflection using the strain gauge, the deflection measured was plotted as a function of the applied voltage and is shown in figure 50. The measured deflection versus voltage relationship shows the typical strain versus electric field behavior of a ferroelectric material such as PZT, typically referred to as a butterfly loop.

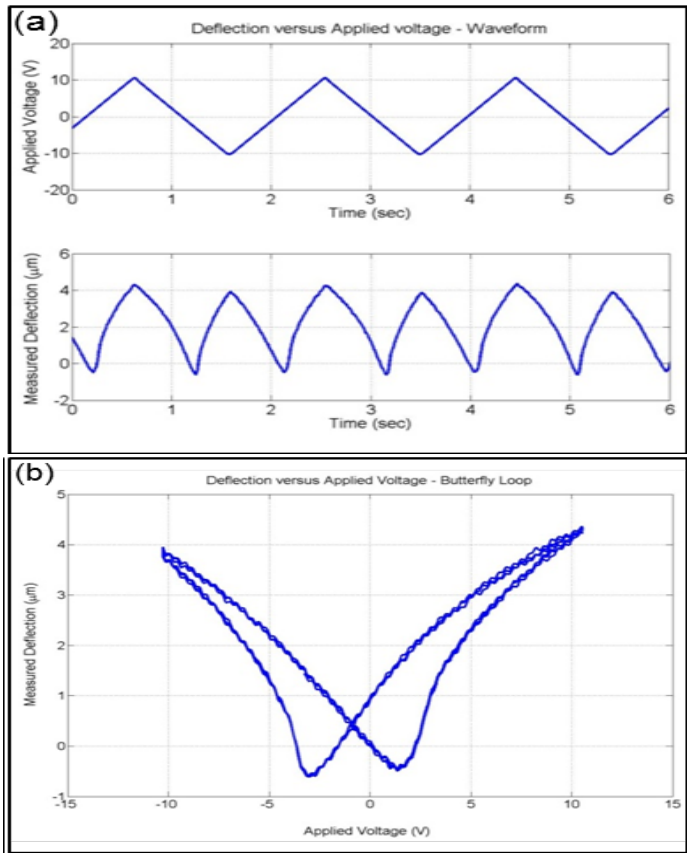

Figure 50: Measured deflection versus applied voltage. (a) Applied voltage and measured deflection waveforms. (b) Deflection versus applied voltage relationship for a single active composite membrane cantilever. The deflection versus applied voltage relationship shows the same behavior as the strain versus applied electric field of a typical ferroelectric material such as PZT.

The response of the cantilever to an oscillating input was also studied. A 12 V peak-to-peak, 1 Hz Sine wave actuation signal was applied. Depending on the input voltage range two distinct effects were observed. Figure 51 shows the response obtained when the cantilever is subjected to a 1 Hz sine wave oscillating between -2 to 10 V. Figure 51 (a) shows the collected waveforms and figure 51 (b) shows the deflection versus applied voltage relationship. As can be seen, when the PZT layer is forward biased a nearly linear deflection – voltage relationship is achieved.

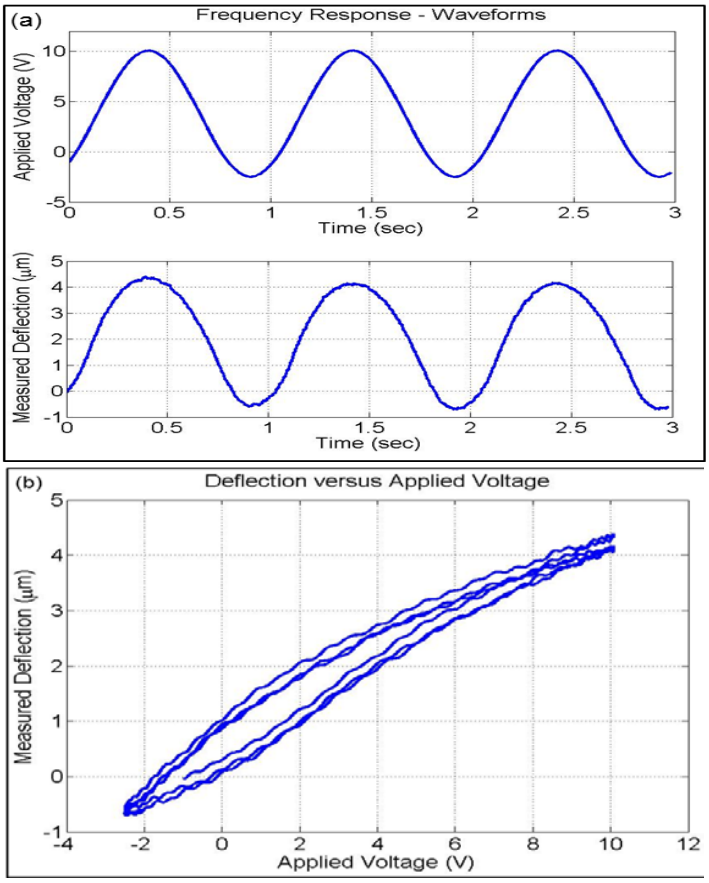

Figure 51: Measured deflection versus applied voltage for a 1 Hz sine wave. (a) Applied voltage and measured deflection waveforms. (b) Deflection versus applied voltage relationship for a forward biased 1 Hz sine wave applied to the PZT actuator. The deflection is approximately linear with respect to the applied voltage.

Next the input voltage range was changed to oscillate between -5 to 7 V. In this case a highly nonlinear response was observed. Figure 52 (a) shows the collected waveforms for applied input and measured deflection. Figure 52 (b) shows the deflection versus applied voltage relationship. Thus when both forward and reverse bias voltages are applied to the PZT layer, the output deflection behavior is highly nonlinear. A frequency doubling effect is also observed with reduced deflections.

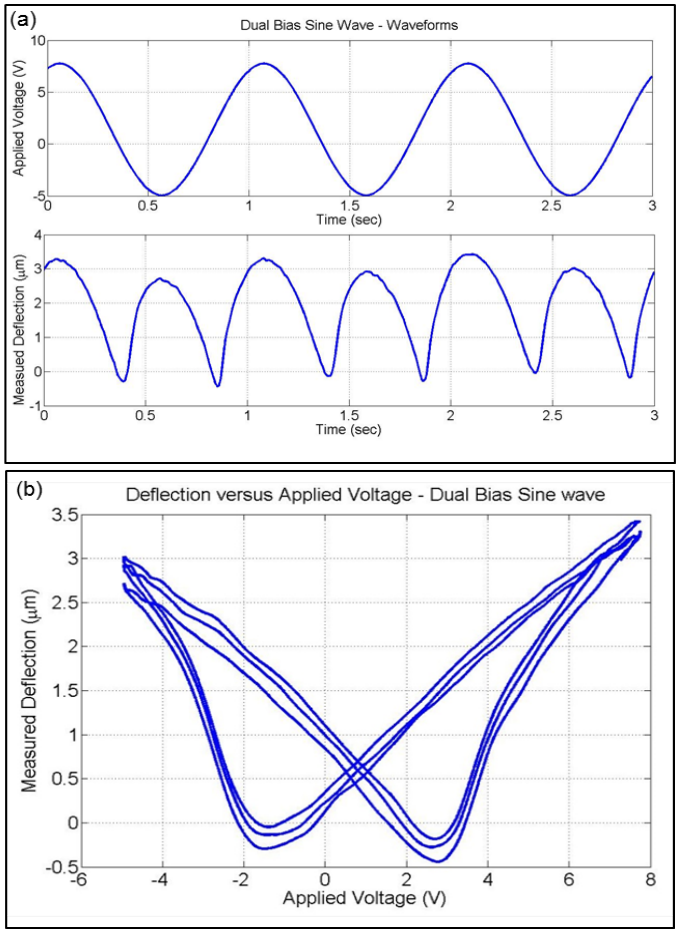

Figure 52: Measured deflection versus applied voltage for a 1 Hz sine wave. (a) Applied voltage and measured deflection waveforms. (b) Deflection versus applied voltage relationship for a dual bias 1 Hz sine wave applied to the PZT actuator. The deflection is highly nonlinear compared to the forward biased case.

For the composite membrane cantilever only the forward biased operation is used. The open loop response result for a single cantilever to a unit step input and is shown in Figure 53 (a). Although the deflection-voltage response is almost linear, there is a strong hysteresis that can be seen in figure 50 (b**)** and its effects are clearly illustrated in figure 53 (b) as the step heights are different for decreasing deflection versus increasing deflection.

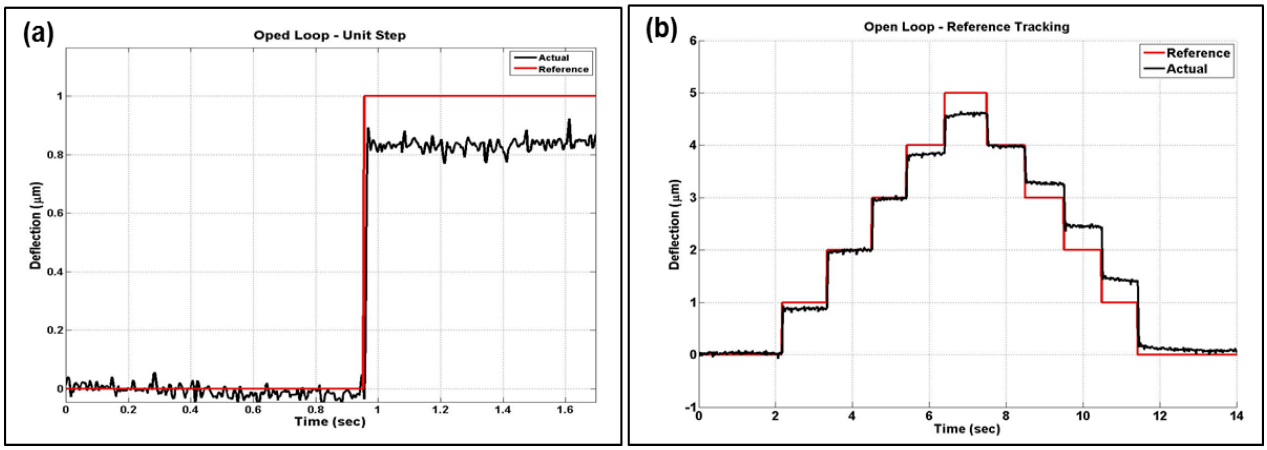

Figure 53: Open loop response of a single cantilever. (a) Response to a unit step input. (b) Open loop reference tracking performance.

4.5.1 Position control

To improve position regulation a closed loop control scheme has been implemented. Figure 54 shows the feedback control diagram of the system. Here r is the reference input, X_m is the measured deflection, e is the error given by $e=r-X_m$, V_m is the strain gage output voltage, V_c is the controller output and V_d is the drive voltage applied to the PZT.

To implement the control scheme we first identified the system transfer function. Using the open loop unit step response the system transfer function was identified using the system identification tool box in MATAB®. A second order linear model was fit to the open loop step response data. The obtained transfer function is:

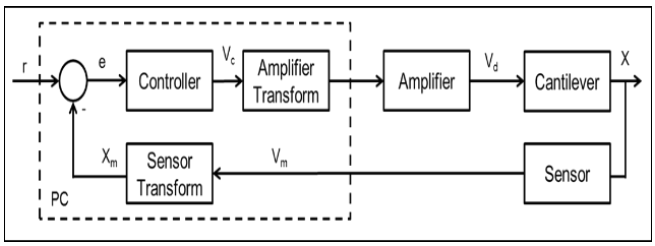

Figure 54: Closed loop system diagram for a single cantilever

$$G(s) = \frac{3844}{s^2 + 92.4s + 4733} \tag{4.7}$$

Once system identification was completed, the feedback control algorithm was implemented in LabVIEW running on an x86-based PC with Windows® operating system. Here results are shown for a single cantilever. Once the feedback control design is completed it can be implemented on all four cantilevers in the array with minimal changes.

A PI control law was used. The controller output $V_c(t)$ is given by,

$$V_c(t) = K_p e(t) + \frac{K_p}{T_i}\int_o^t e(t)\, d\tau \tag{4.8}$$

Or equivalently

$$V_c(t) = K_p e(t) + K_i \int_o^t e(t)\, d\tau \tag{4.9}$$

Here the proportional and integral gains are K_p and K_i respectively, e is the error given by $e=r-X_m$. The discrete time version of the control law that was practically implemented is given by,

$$u_k = u_{k-1} + K_p(e_k - e_{k-1}) + K_i T_s e_k \tag{4.10}$$

Where u is the controller output, e is the error and T_s is the sampling time between two successive iterations. The subscripts k and $k-1$ demote the current and previous iteration respectively.

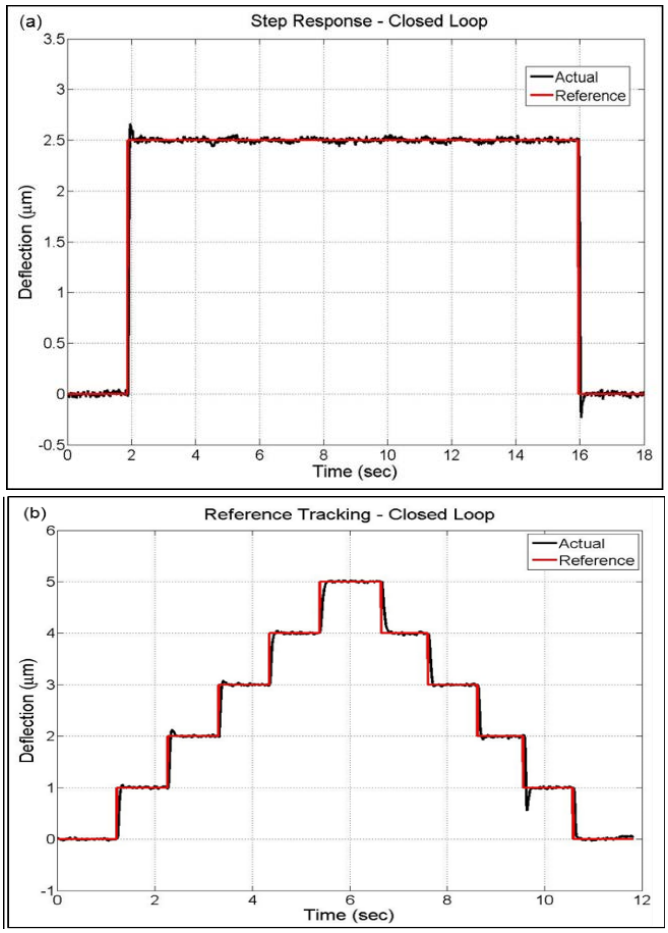

Figure 55: Closed performance of a single active composite cantilever. (a) Response to an arbitrary step input. (b) Response to multiple step inputs showing good tracking over the entire actuation range.

The proportional gain K_p and integral gain K_i were designed using the PID controller tuning tool available in MATLAB® (version 2014a) and were calculated to be 1 and 72 respectively. Figure 55 shows the step response and tracking performance of the system. Figure 56 shows the tracking performance of the system for 100 nm step inputs.

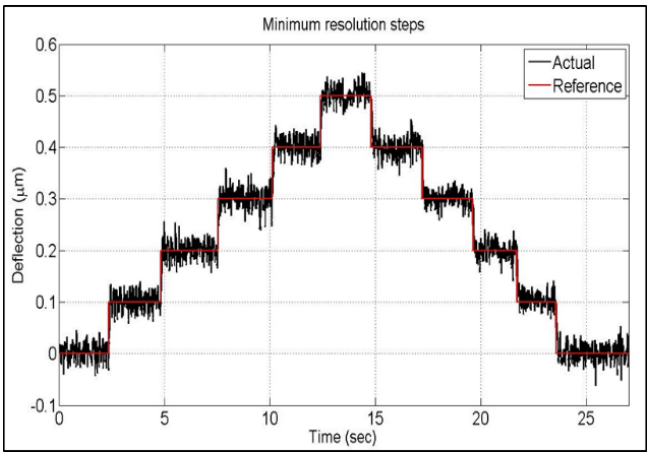

Figure 56: Tracking performance for 100 nm step inputs. The sensor noise limits the resolution.

4.5.2 Force control

In addition to position control we also use the stamps for force control. The goal is to bring the post of the membrane into contact with a surface and control the pressure exerted by the post onto the surface using internal actuation.

To achieve this we first perform static calibrate of the sensor. The calibration is performed using the custom calibration and testing setup that has been described earlier.

A single post on the membrane is brought into contact with the load cell and the force registered by the load cell is recorded. Next, input voltage is applied to the PZT to bend the cantilever, this exerts a load onto the load cell and the bending of the cantilever produces a signal from the strain gauge. The actuation voltage is varied and the resulting strain gauge output and the force measured by the load cell are recorded. A triangular waveform input voltage was applied to the PZT. Figure 57 shows the graph of the input voltage waveform, force measured from the load cell and the output voltage of the strain gauge. Using the collected data the strain gage is calibrated.

After Calibration, a PI controller was implemented to regulate the force applied by the post onto the loadcell. Using the internal calibrated strain gage the applied force was estimated. The loadcell provided the external measurement of the actual force being exerted and was only used to gage performance. The reference tracking performance of the system is shown in figure 58. A reference signal of 250 μN force steps was applied. The system was able to track the reference

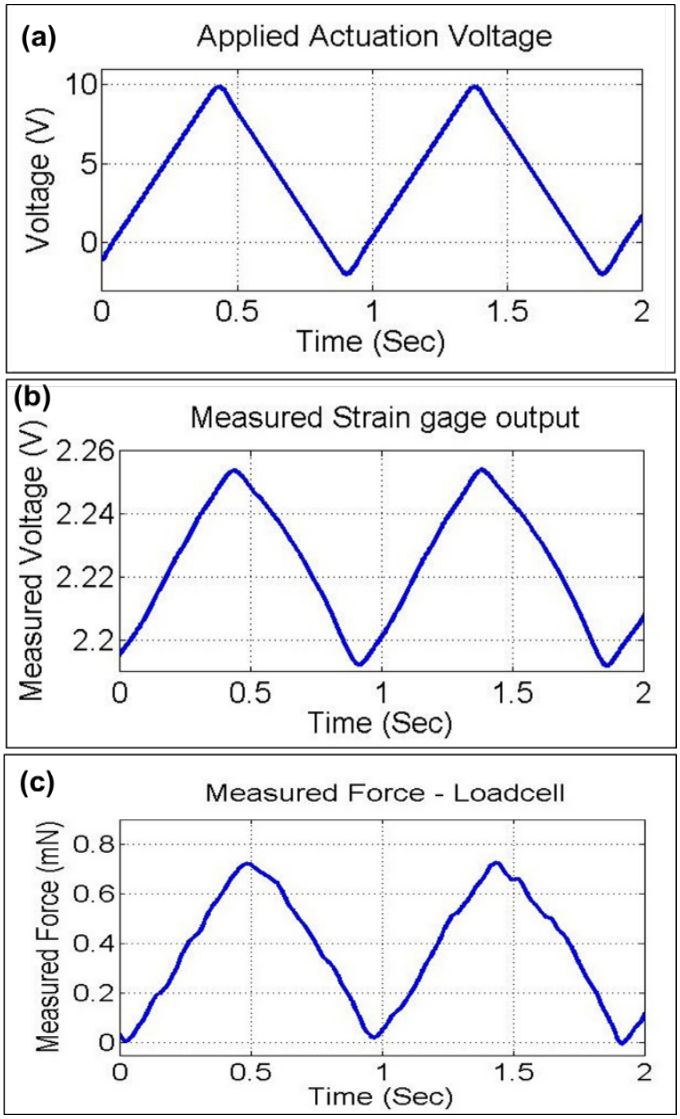

Figure 57: Force sensor calibration waveforms. (a) Applied actuation voltage waveform. (b) Measured strain gauge output voltage waveform. (c) Waveform for the force applied by the post when subjected to the actuation voltage in (a).

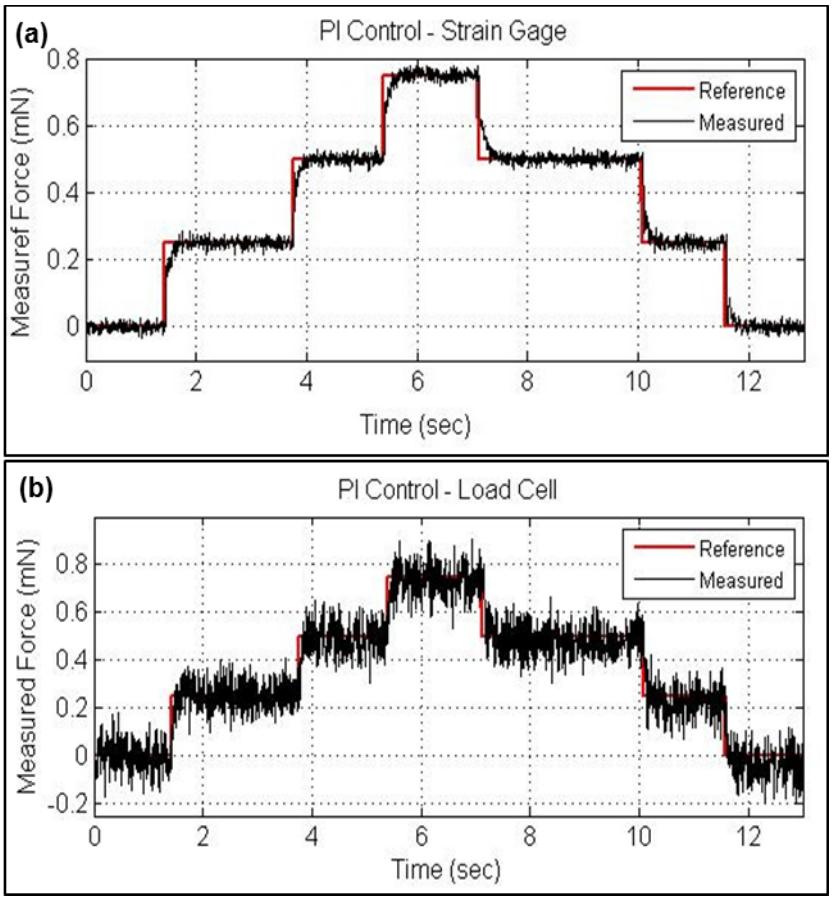

Figure 58: Reference tracking performance of the closed loop system. (a) Signal collected from the strain gage. (b) Signal collected from the loadcell measuring the actual applied force.

very well. Figure 58 (a) shows the signal captured using the strain gauge. Figure 58 (b) shows the actual force being applied. The result show good agreement between the reference and the applied force.

The tracking performance of the system for 50 μN steps is shown in figure 59. These small steps are beyond the resolution limit of the loadcell used to verify the actual force being applied, however the general trend and maximum force applied is still visible in figure (b) and shows good agreement with the measurements in figure 59 (a). Here also the minimum resolution is determined by the signal noise in the sensor.

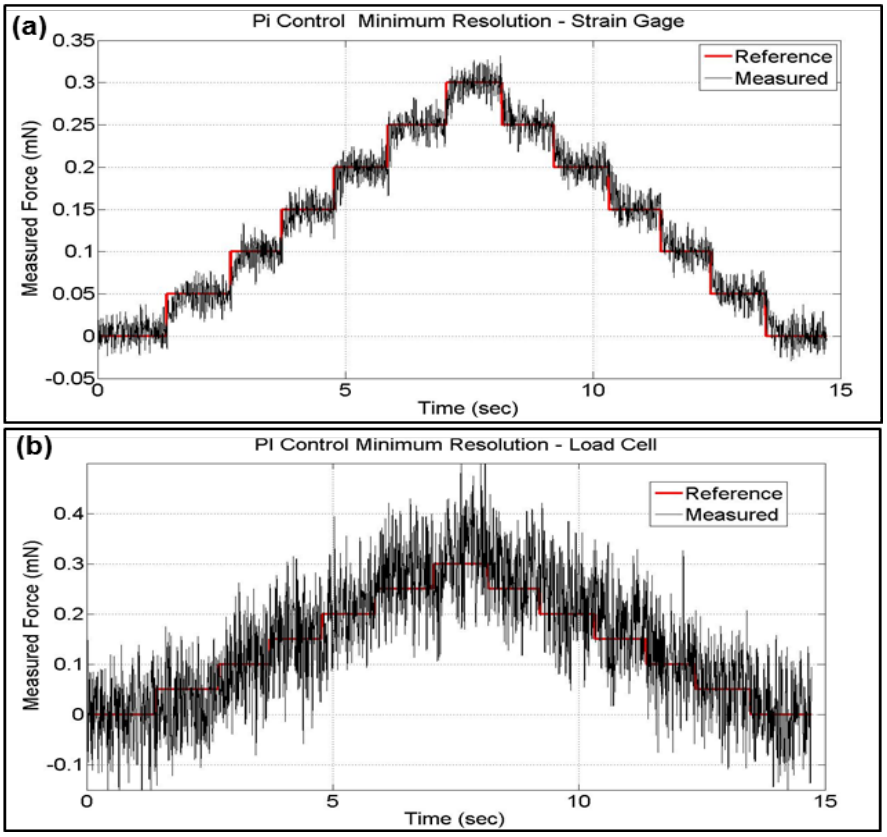

Figure 59: Minimum resolution steps tracking performance. (a) Signal captured from the strain gauge. (b) Measured force signal from the loadcell.

4.6 Conclusion

In this chapter we presented the development of micro transfer printing stamps with integrated sensing and actuation based on the active composite material, extending the instrumented composite stamp design. The active composite stamps design was presented along with the development of a facile fabrication process to manufacture the stamps.

After fabrication the stamps were characterized and calibrated, comparisons were drawn with the design values. Following characterization and calibration the stamps were integrated into

the micro transfer printing process and a new collect and place process mode – in which the ink is picked up in parallel and deposited selectively – was demonstrated.

Finally a new actuation calibration system was described. Using the calibrated stamps a closed loop control scheme was developed. Closed loop position control was demonstrated with the ability to perform 100 nm steps. Using the stamps closed loop contact force control was also demonstrated with the ability to produce force as small as 50 μN.

CHAPTER 5: ACTIVE COMPOSITE STAMPS : THERMO-MECHANICAL ACTUATION

During the design process of the active composite material based stamps, the existence of a potential second actuation mode based on the architecture of the stamps was identified. The integration of a ceramic layer into a composite structure created a bi-material cantilever. Exploiting the large CTE mismatch between the PZT and the SU-8 layers, it would be possible to thermally actuate the stamps. The integrated strain gauge in the cantilever would provide the means of heating the cantilever through joule heating. In addition to being a structure layer, the PZT would act as a sensor to sense contact and interaction forces by means of its piezoelectric properties. It would also be able to sense the deflection of the cantilever by the charge generated due to deflection and heating; through a combination of the piezoelectric and pyroelectric properties of the PZT. Thus from a functionality point of view the piezoelectric PZT layer now serves as a sensor and the integrated strain gauge serves as the actuator, deflecting the cantilever through the heat generated in it when a current is passed through it. This gives rise to a second actuation mode which we term as thermo-mechanical actuation.

5.1 Actuation simulation

To calculate the deflection of the active composite stamp under thermo-mechanical actuation we simulated a single cantilever of the active composite stamp. Using the same FEA model that was developed for the piezoelectric actuation mode described in chapter 4, the actuation of the posts as a function of the cantilever temperature was calculated. The same model was used since the stamp architecture in both the application modes is identical, only the function of the actuation layer and the sensing layers are interchanged in the two modes.

The glass transition temperature T_g of cross-linked SU-8 can vary between 150°C to 240°C based on the degree of crosslinking and post exposure bake temperature [63]. To ensure safe operation of the device a maximum operating temperature of 90°C was chosen. The simulation assumed uniform heating of the entire cantilever. Using the above constraint and assumption the deflection of the post for different temperature was calculated. The FEA results predict a deflection of 20 µm for the maximum temperature of 90°C. Figure 60 (a) shows the graph of the calculated deflection versus temperature from the FEA. A frame from one of the simulations showing the cantilever deflection is also shown in figure 60 (b). The calculated deflection is about three times

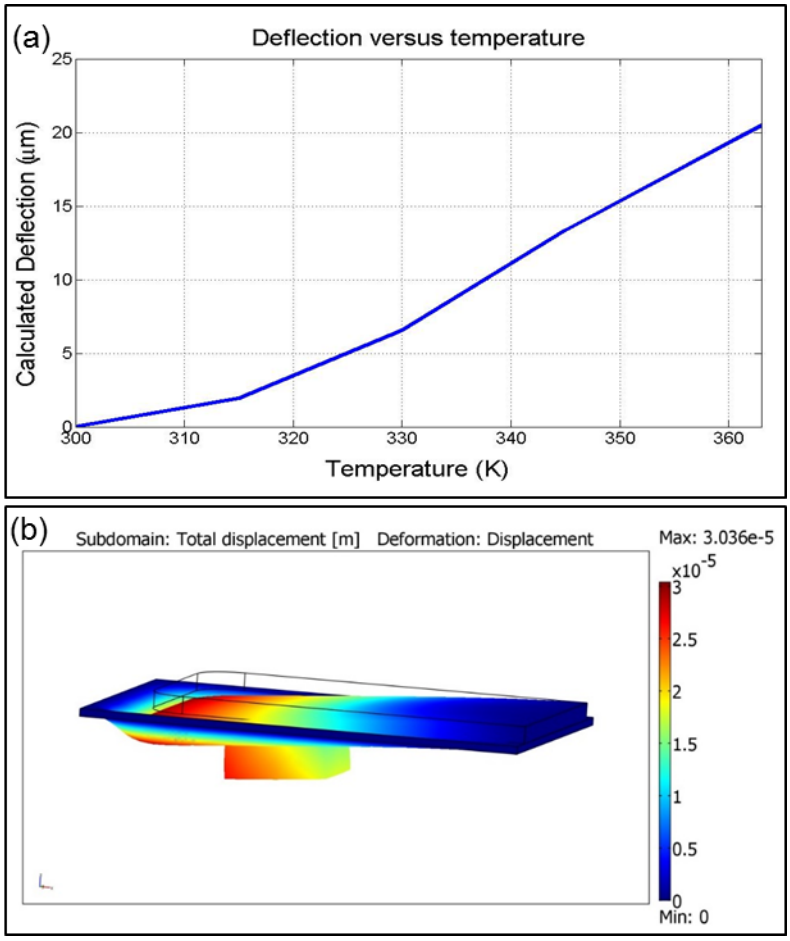

Figure 60: Results from the finite element analysis. (a) Graph of deflection versus temperature. (b) Single frame of the representative deflection calculated from the FEA simulation.

larger than what is achieved from the piezoelectric actuation mode. The predicted deflection is sufficiently large to allow more robust operation of the stamp in applications requiring stamp geometry modulation.

5.2 System characterization

Using the improved optical calibration setup described above in section 4.5 the actuation behavior of the thermo-mechanically actuated active composite stamps was experimentally studied. The stamp under test is mounted onto the transfer printer as was done in previously described testing setups. Here the PZT sensing element is connected to a custom built charge amplifier; which converts the charge generated by the PZT sensor into a voltage, this voltage is then fed into the data acquisition device (National Instruments, USB-6009). The heating element is connected to a drive circuit that is controlled using the transfer printer software.

5.2.1 Actuation measurements

To measure the actuation behavior of the individual posts on the stamp, a voltage was applied to the heating element of the individual cantilevers in the stamp. The deflection of the post as a function of the input voltage was recorded. A voltage of 0V to 3V was applied with 0.5V steps, each experiment was repeated five times and the deflection was averaged. The results of the experiment was shown in figure 61.

The results of figure 61 (a) show a nonlinear behavior that is in agreement with the i^2R heating that is taking place in the individual heating elements. When the input power is considered instead of the voltage as the control variable, a linear relationship between the deflection and the input power is observed as can be seen in figure 61 (b).

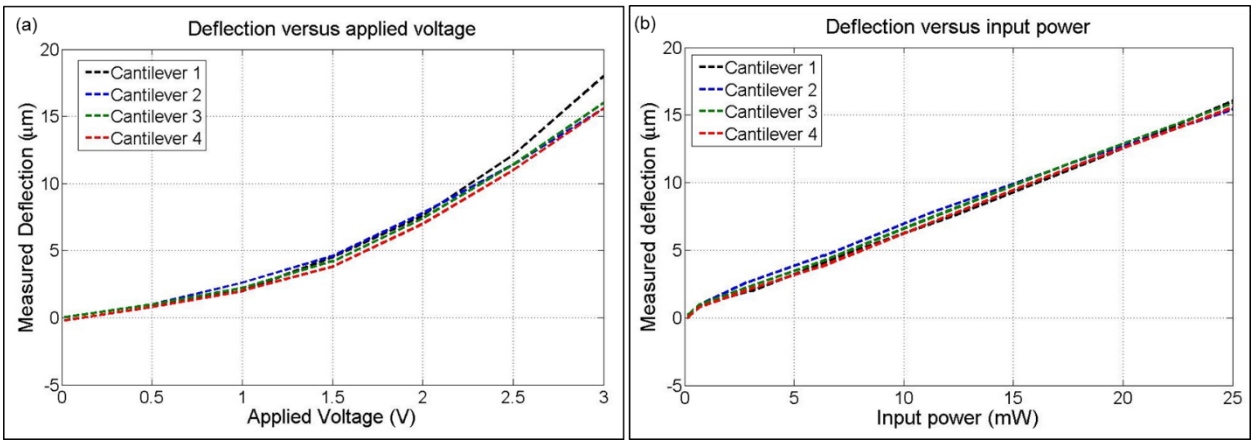

Figure 61: Graph of the actuation behavior of the posts of the active composite stamp under thermo-mechanical actuation. (a) Graph of deflection as a function of the applied voltage to the heating element of the individual cantilevers. (b) Graph of deflection of each cantilever as a function of the input power.

Using the actuation data a mathematical model of the response of the individual cantilevers was developed.

$$d = C_1 P_i + C_2 \tag{5.1}$$

A first order polynomial as shown in eq. 5.1 was fit to the post deflection as a function of input power data of figure 61(b). The model is used later to calculate the deflection of the post during sensor calibration and dynamical modeling. Each post was calibrated individually

5.2.2 PZT based sensing

After measuring the actuation behavior of the stamp, the PZT based sensing was characterized. Using the custom measurement and calibration setup described earlier the PZT sensor was characterized. The voltage output from the PZT sensor was recorded. The PZT sensors had an average sensitivity of 246 mV/mN. Transfer printing was performed using the stamps. A typical voltage trace measured during transfer printing is shown in figure 62. The signal showed sufficient resolution to detect important process events.

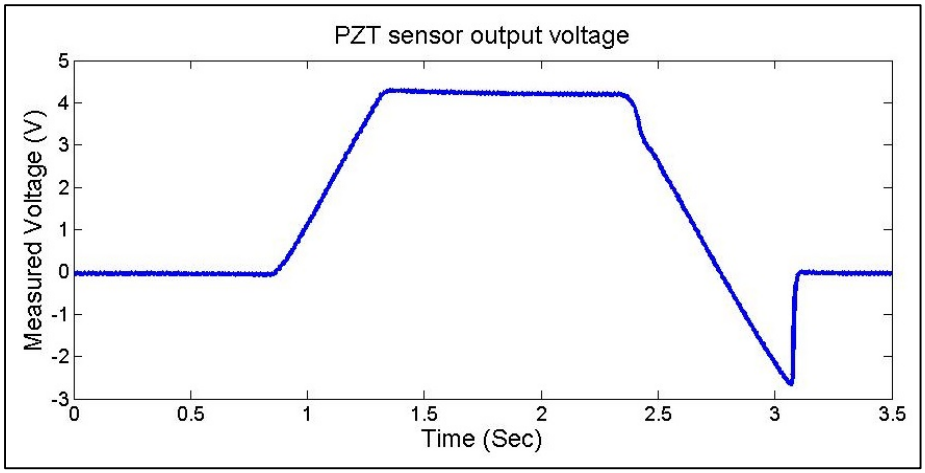

Figure 62: Graph of a typical voltage trace generated by the PZT sensor during transfer printing.

Once the external force sensing and event detection capabilities using the PZT sensor were experimentally verified, the sensor was characterized for measuring the deflection of the posts. PZT exhibits both piezoelectric and pyroelectric behavior hence the signal sensitivity is different

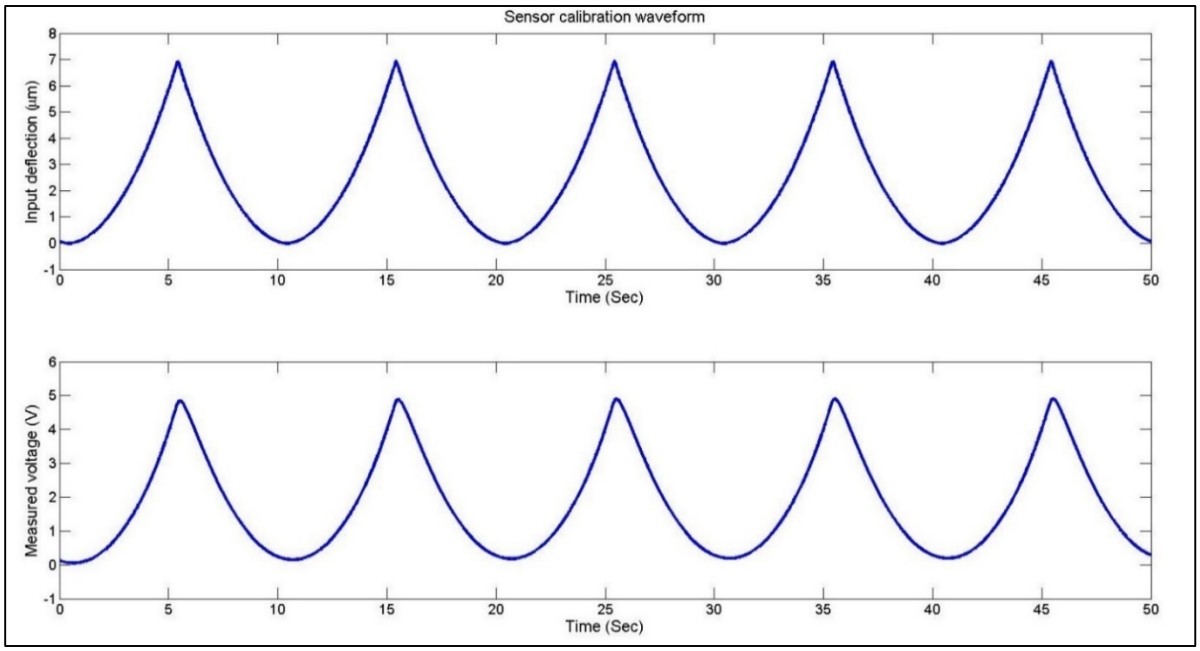

Figure 63: Typical graph of deflection of the post and the resulting sensor output voltage for a single post of the active composite stamp. The measured voltage versus deflection data is used to calibrate the sensor for sensing the deflection when the posts are actuated.

when sensing actuation because the sensor gets heated up along with the cantilever during the thermo-mechanical actuation.

To characterize the deflection sensing, a triangular voltage waveform was applied to the heater of each cantilever. The output voltage from the PZT sensor was recorded along with the input voltage waveform. Using the actuator model and the input voltage; the deflection of the post was calculated. Figure 63 shows a graph of the post deflection and the resulting sensor output voltage. Using the collected data each sensor was calibrated. A first order polynomial model as in eq. 5.2 was fit to the calibration data for each sensor. This sensor calibration is later used for dynamic modeling and the final closed loop control.

$$d_m = K_1 V_m + K_2 \tag{5.2}$$

5.2.3 Modeling dynamic behavior

Once the actuator and sensor calibration was completed the dynamic behavior of the stamp was modeled. Using frequency domain system identification techniques a transfer function for the behavior of the stamp posts was developed.

First the response of the system to a variable frequency signal was recorded. Using a function generator, a 180 second linear chirp signal from 0.05 Hz to 5 Hz was generated. This signal was fed into the heater of each cantilever using the drive circuit. As the cantilever deflected in response to the input signal, an output signal corresponding to the produced deflection was generated from the PZT sensor. Both the input voltage signal and the sensor output signal were recorded simultaneously. After signal collection, using the actuator and sensor models the signals

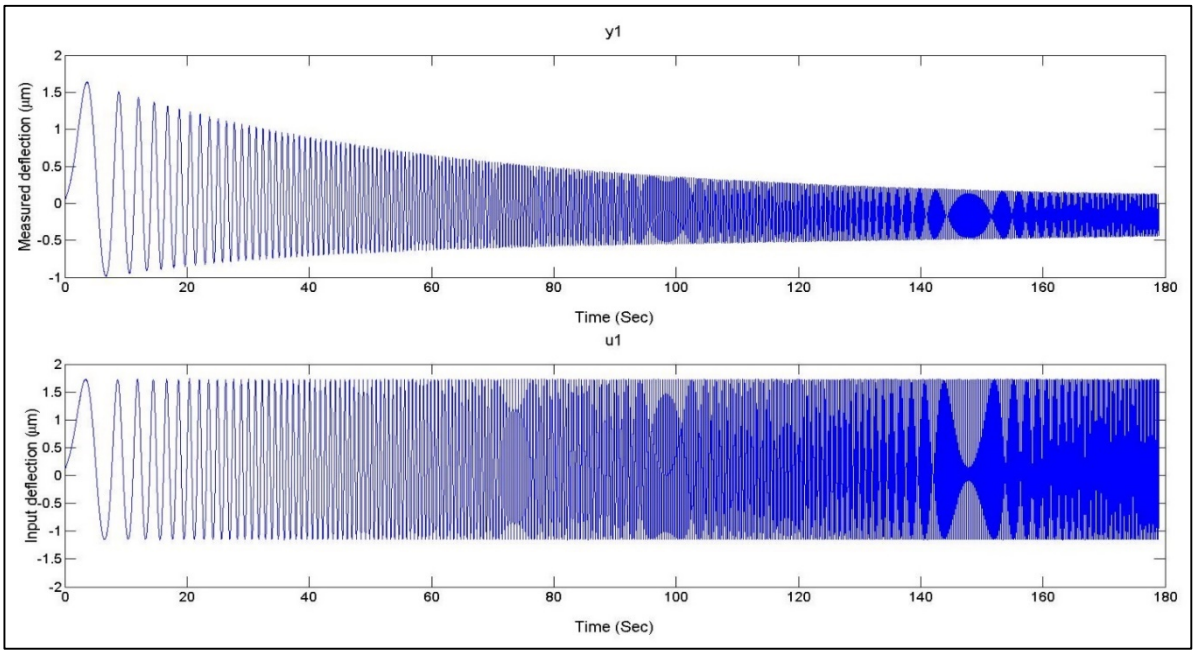

Figure 64: Graph of data collected for modeling the dynamic behavior of the posts. The trace shows the desired deflection u1 and measured deflection y1 of a single post as the input signal frequency is varied.

were converted into the desired and measured deflection. Figure 64 shows the trace of desired deflection and the actual deflection of a single post collected during the experiment. Using this

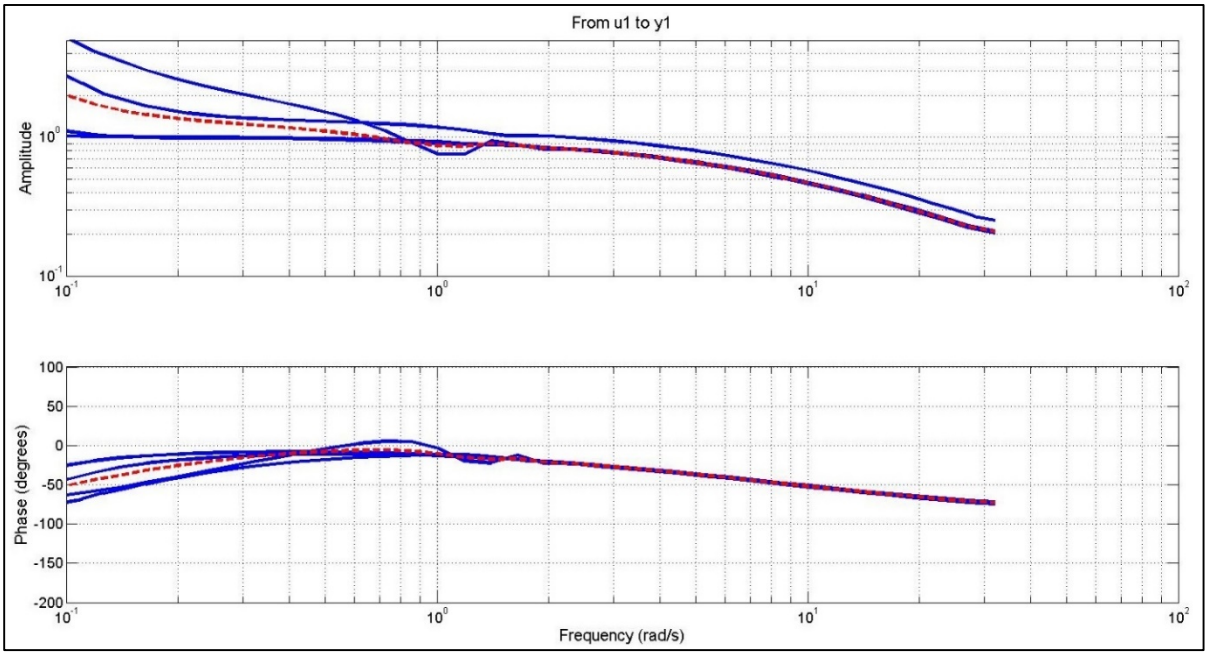

Figure 65: Graph of the frequency response of the individual posts of the stamp (blue, solid lines) along with the average (red, dashed line)

method the frequency response of each post on the stamp was collected.

After the frequency response data was collected it was converted from its original time domain form into the frequency domain to get the spectral data of figure 65. The solid lines in figure 65 correspond to the response for each individual post. The dashed line is the average of the four posts. To identify a single model depicting the nominal behavior of the posts we used the average of the spectral responses to identify the transfer function.

A second order transfer function model was fit to the average frequency response. The frequency response of the identified model and the original data are shown in figure 66. A second order model was the simplest model that showed good agreement with the collected frequency response data. The identified nominal model is:

$$G(s) = \frac{1.043s + 0.125}{0.171s^2 + s} \tag{5.3}$$

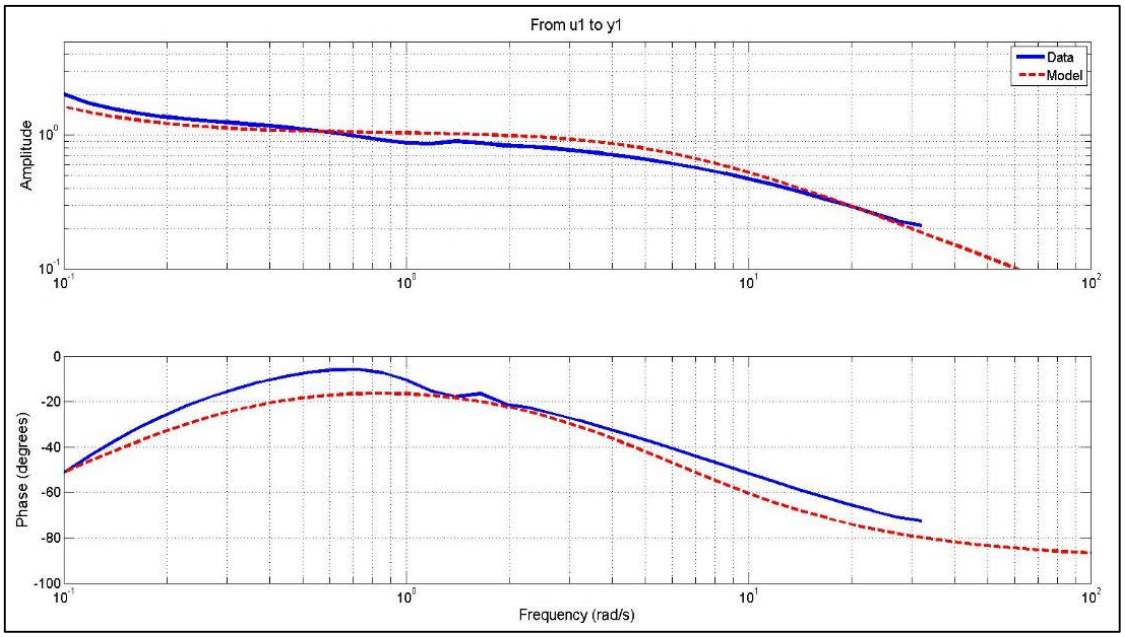

Figure 66**:** Graph of the frequency reponse of the model along with the original data used to fit the model.

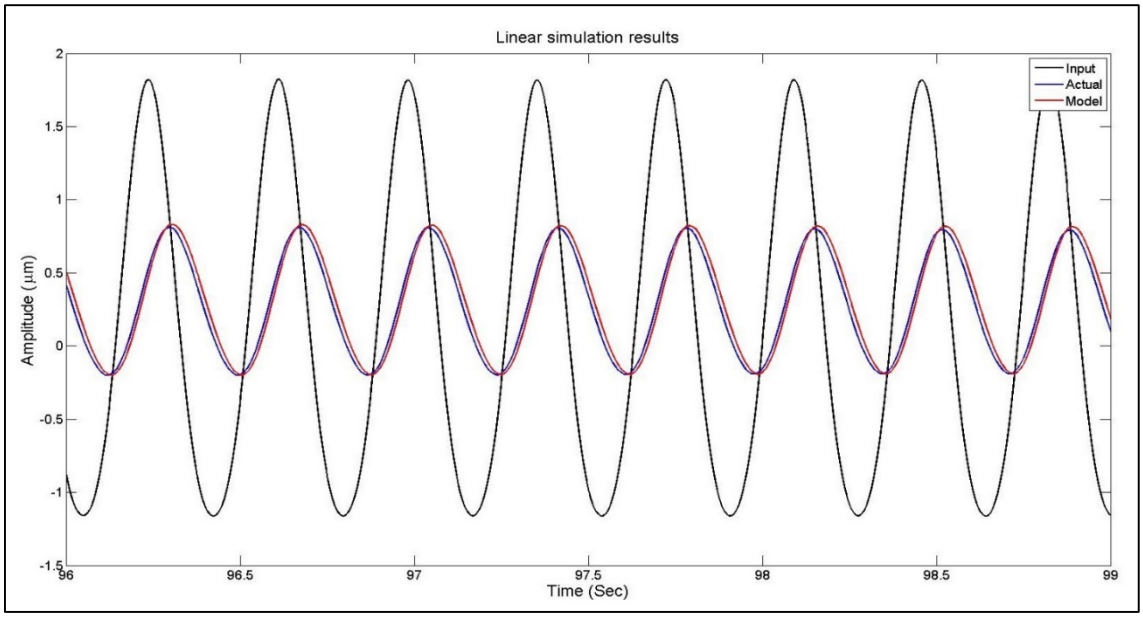

Figure 67**:** Linear simulation results of the nominal system model along with the actual system response for once of the posts of the active composite stamp.

After identification of the nominal system transfer function the response of the model was simulated. The input signal used to test one of the posts was applied to the nominal model and its response was calculated. The simulated response was compared with the actual response of the post. The result showed good agreement between the model and the actual system. One of the simulation results is shown in figure 67.

5.3 Closed loop control

To improve the accuracy of position regulation a closed loop control system was implemented to control the deflection of the individual posts. Using the nominal model for the system described earlier in section 5.2.3, a PI controller was designed using the PID tuning toolbox in MATLAB®. The implemented control architecture is shown in figure 68.

A reference signal *r;* is the desired deflection of the post to be tracked by the control system, X_m is the measured deflection of the post as read from the sensor; calculated using eq. 5.2, *e* is the

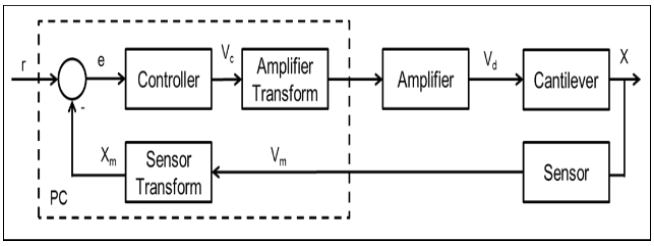

Figure 68: Closed loop system diagram for a single cantilever

error between the reference and the actual post deflection given by $e=r-X_m$, V_m is the voltage of the PZT sensor, V_c is the controller output and V_d is the drive voltage applied to the heater of the cantilever.

The feedback control algorithm was implemented in LabVIEW running on an x86-based PC with Windows® operating system. Here results are shown for a single cantilever. The same feedback control design is implemented on all four cantilevers in the array with minimal changes. A discrete time control law is used as shown below in eq. 5.4.

$$u_k = u_{k-1} + K_p(e_k - e_{k-1}) + K_i T_s e_k \tag{5.4}$$

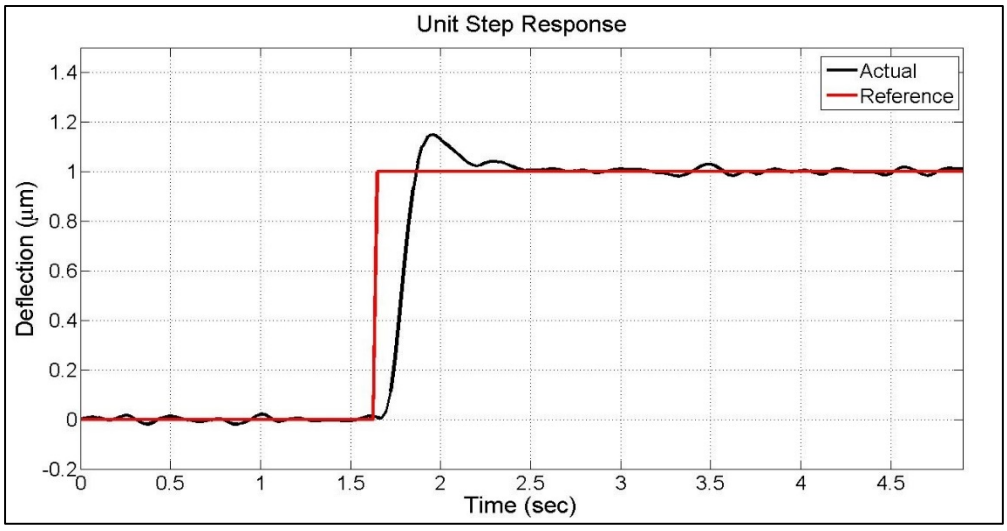

Figure 69: Closed loop system response to a unit step reference.

Where u is the controller output, e is the error and T_s is the sampling time between two successive iterations. The subscripts k and $k-1$ demote the current and previous iteration respectively.

The proportional gain K_p and integral gain K_i were calculated to be 0.328 and 4.27 respectively. The sampling time for the closed loop system was 25 msec. The closed loop control system was implemented and the closed loop performance of the system was experimentally determined. Figure 69 shows the unit step response the system. A rise time of 250 msec and a settling times of 500 msec is experimentally observed.

In addition to measuring the step response, the performance of the system to track multiple step reference and minimum step resolution was also tested. Figure 70 shows the response of the control system to multiple step inputs. The experimental results show good tracking performance over the entire range. Figure 71 shows the system tracking performance to 100nm steps. Good tracking performance was observed over the entire operational range.

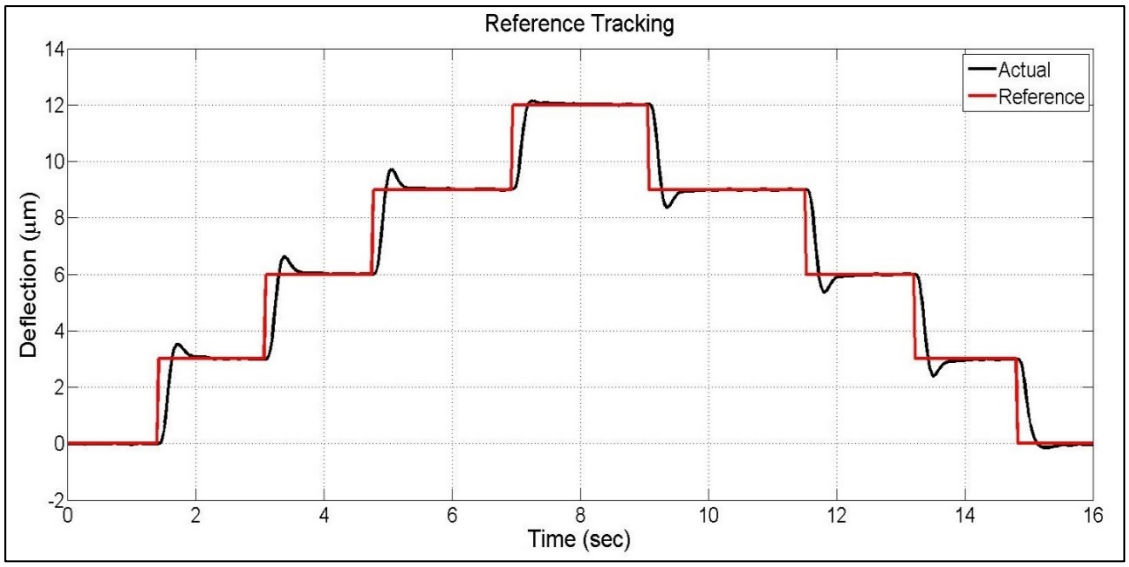

Figure 70: Closed loop system response to multiple step inputs showing good tracking over the entire actuation range.

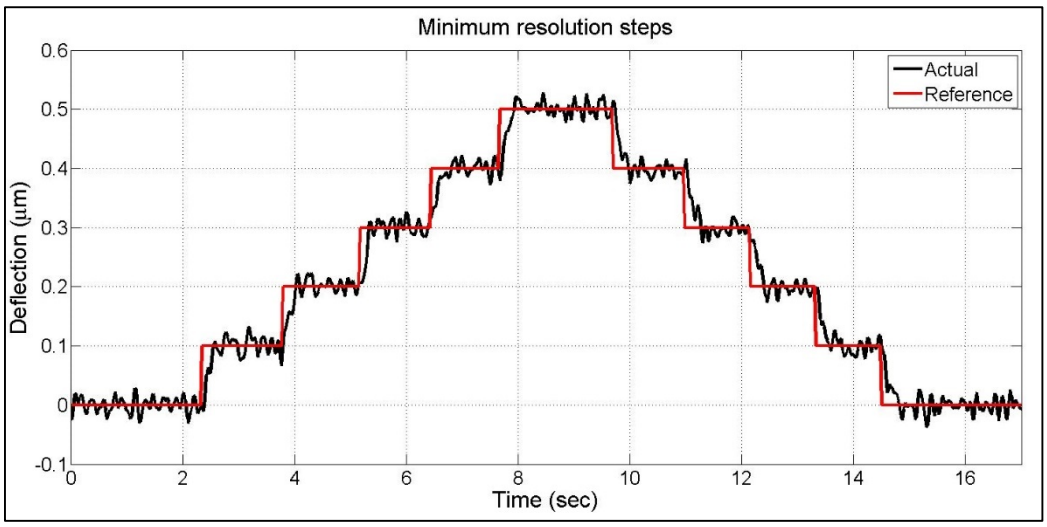

Figure 71: Tracking performance for 100 nm step inputs. Good tracking performance is observed in this case.

5.4 Transfer printing experiments

The main motivation of creating stamps using the active composite material is to develop stamps that allow for new modes of transfer printing to be implement using their integrated functionality. This section presents the experimental results of implementing some of these novel transfer printing modes.

First a set of sample inks was developed with two different types of ink to test selective transfer printing. Two different regions were created on the donor. Gold pads 50 µm x 50 µm were patterned on silicon chips. Two types of silicon chips were created, type 1 with four pads and type 2 with two pads. Figure 72 shows the image of the ink sample with the two different type of silicon chips. The two different types of silicon chips depict two device types to be used for demonstrating selective ink retrieval.

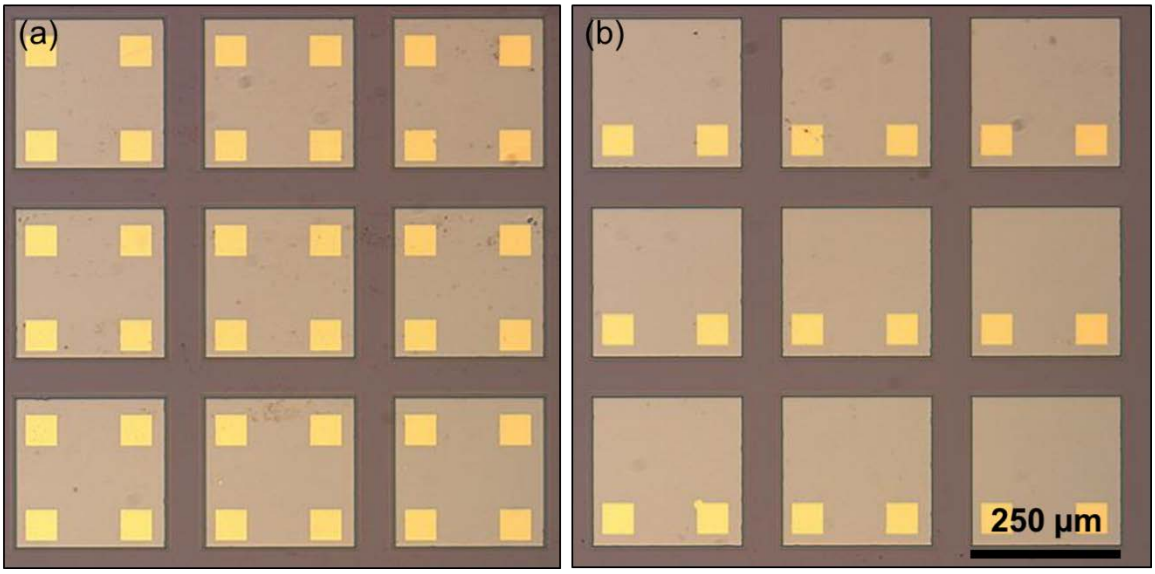

Figure 72: Image of two different types of ink designed to experimentally test selective transfer printing based on thermally actuated active composite stamps. (a) Type 1 devices and (b) type 2 devices.

The first printing mode that was implemented using the thermo-mechanically actuated stamps was the collect and place printing mode. Type 1 silicon chips from the donor substrate are retrieved in parallel from the donor wafer using all the posts. After ink retrieval the stamp travels to the acceptor substrate. Here each individual post is actuated and brought into contact with the receiving substrate, a single post is used to print one silicon chip at a time. Figure 73 shows a collection of frames captured during the collect and place printing process. In figure 73 (a) the ink has been retrieved using all four posts on the stamp. Figure 73 (b) shows the ink released only from the first post, the rest of the posts have their ink still attached to the post. Figure 73 (b), (c) and (d) shows subsequent frames for printing done by actuating a releasing ink from post two, three and four respectively.

Figure 74 shows the image of a sparse array printed using the collect and place printing mode. A total a 20 silicon chips were printed with 5 ink retrieval steps. The spacing between each device on the acceptor is larger than the width of the four posts on the stamp.

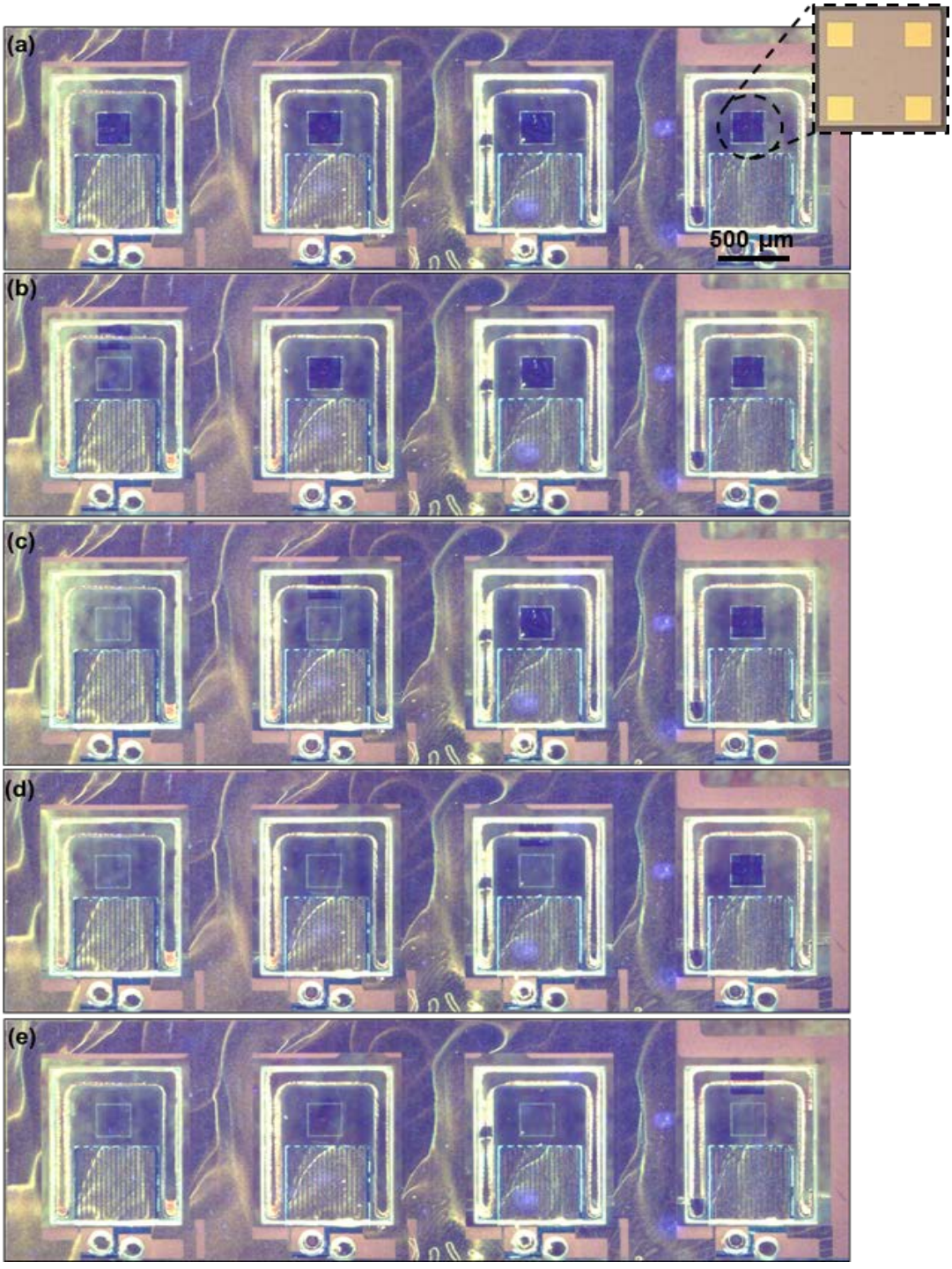

Figure 73: Frames captured during collect and place printing using the thermo-mechanicall actuated active composite stamp. (a) Image of the four posts with their retreived ink. (b) Image of post one after actuation and ink release. (b), (c) and (d) Images of post two three and four respectively after actuation and release of their ink.

Figure 74: Image of a sparse arrach of silicon chip printed onto an acceptor substrate using a collect and place printing more.

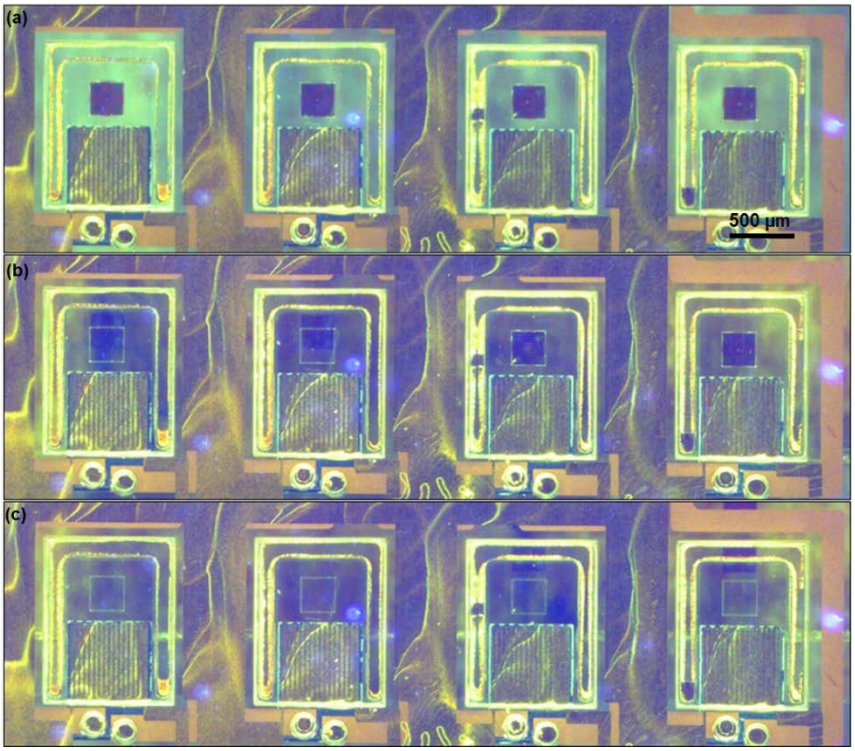

Figure 75: Frames captured during collect and place printing with actuation. (a) Image of the four posts with their retreived ink. (b) Image of posts one and two after actuation and ink release. (b) Image of posts three and four after actuation and release of their ink.

Since the posts are individually addressable printing can also be performed using a combination of posts. Figure 75 shows image of frames captured during collect and place printing with parallel printing. Here a pair of posts is used to print ink in parallel. For this mode, type 1

silicon chips from the donor were used. Figure 75 (a) shows image of four type 1 silicon chips retrieved from the donor, figure 75 (b) shows image of devices printed using actuation and release, using post one and two while devices on post three and four are still attached to their posts, figure 75 (c) shows the posts with no silicon chips attached to them after actuation and release from posts three and four.

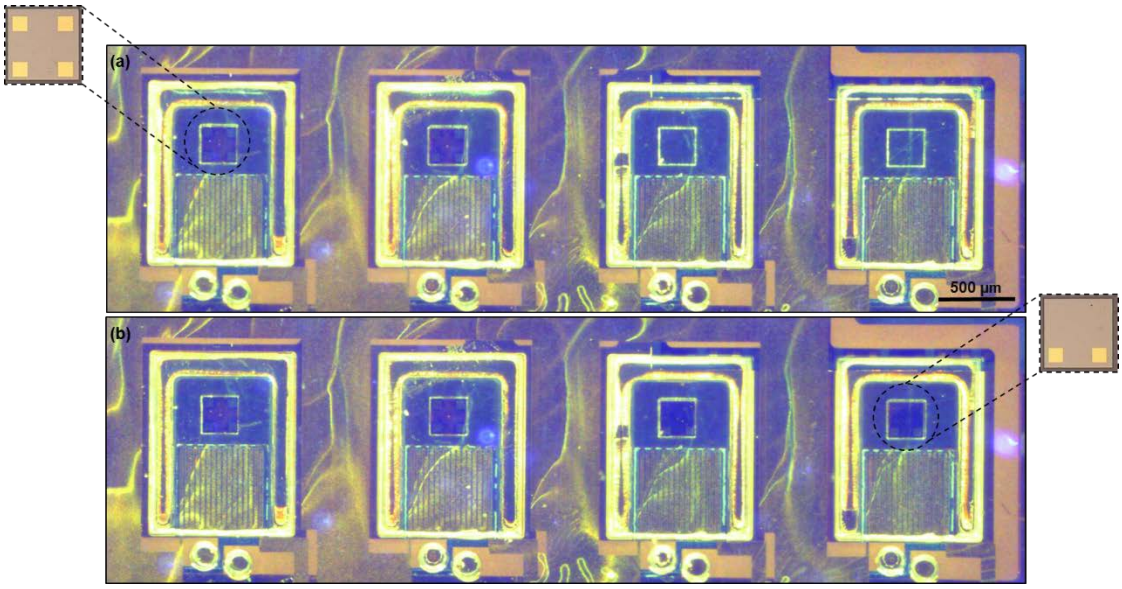

Figure 76: Image of selective ink retreival. (a) Image of type 1 silicon chips picked up using posts 1 and 2 with no ink attached to post 3 and 4. (b) Image showing type 2 silicon chips picked up using posts 3 and 4 with type 1 chips attached to posts 1 and 2.

In addition to collect and place, the ability to modulate stamp geometry also allows for selective retrieval of inks. To experimentally demonstrate this application mode a stamp was first aligned with type 1 silicon chip region of the donor. Using parallel actuation a pair of type 1 silicon chips were picked up shown in figure 76 (a), post three and four have no devices attached to them. Next the stamp was aligned with the second region with type 2 silicon chips and the type 2 silicon chips were picked up using parallel actuation of posts three and four shown in figure 76(b).

After ink retrieval they were printed onto the acceptor substrate using a combination of selective printing. Figure 77 shows an image of the two device types printed together onto the same substrate in an asymmetric pattern using a single stamp and setup.

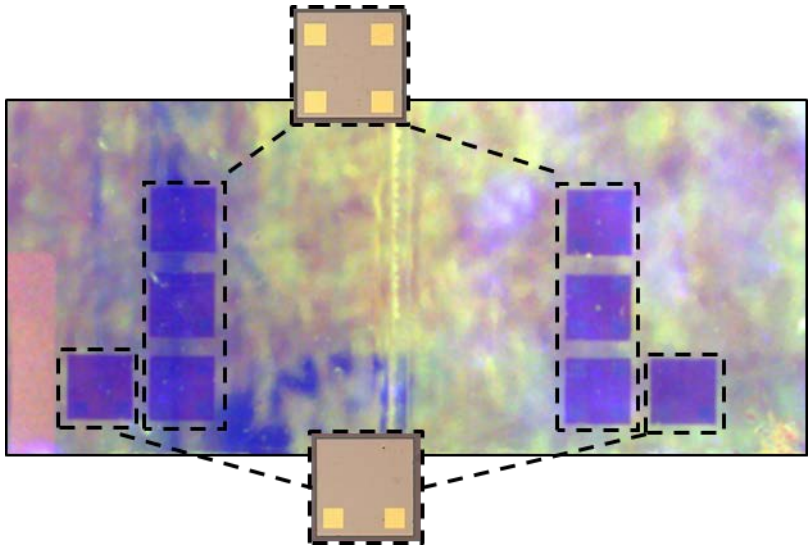

Figure 77: Image of an assymetrical pattern printer using selective ink retreival and printing. The pattern has six type 1 silicon chips and two type 2 silicon chips printed at two different pitches.

5.5 Conclusion

In this chapter we presented the extension of the operation of the active composite material based micro transfer printing stamps by employing thermo-mechanical actuation and piezoelectric sensing. Finite element analysis was used to simulate the behavior of the stamp and the simulation results predicted that the thermo-mechanically actuated stamps can achieve three times larger deflection compared to the piezoelectric actuation mode.

Using the calibration setups, experimental data for the actuation and sensing behavior for each post were collected; mathematical models for actuation and sensing were developed using the experimental data. Using frequency domain system identification techniques a nominal

dynamic model of the system was developed. The simulated output of the developed model was compared to the actual system and showed good agreement with the experimental measurements.

Finally using the nominal system model a closed loop system was designed. Closed loop control was implemented on the individual posts using the designed gains. The response of the closed loop system to different references was experimentally measured. Good dynamic performance and reference tracking was achieved using the closed loop system.

CHAPTER 6: EXPLORING NEW APPLICATION AREAS FOR MICRO TRANSFER PRINTING

This chapter presents the results of pilot experiments conducted to test the feasibility of using micro transfer printing in new application areas.

6.1 Micro scale assembly with in-situ bonding

The main motivation behind this experimental study is to assess the use of transfer printing to perform micro scale assembly, taking advantage of the inherent parallelism of transfer printing. The idea is to perform micro scale assembly of silicon using transfer printing and in-situ bonding of silicon to polymer. The process works by bringing a piece of silicon in contact with a polymer, using localized heating at the silicon/polymer interface the polymer is heated above its glass transition temperature and then allowed to cool back down, bonding the silicon to the polymer. This process has the potential to allow micro scale assembly without the need for specialized interfaces for attachment such as clamps, specialized hinges, etc. The polymer chosen for testing this process is SU-8. SU-8 is a thermally and chemically stable epoxy based negative tone permanent photoresist. It can be easily spin coated with thickness varying from 10 µm up to 300 µm. The glass transition temperature of cross-linked SU-8 varies between 150^{o}C to 240^{o}C. Owing to good thermal and chemical stability and compatibility with standard microfabrication techniques made SU-8 a good candidate for this experimental study.

6.1.1 Achieving localized heating through laser irradiation

The main idea of the process is to bond silicon to a polymer by heating the silicon/polymer interface. To locally heat only the silicon/polymer interface requires a highly confined heating source. One way to produce this highly localized heating is to use a laser source to heat the silicon.

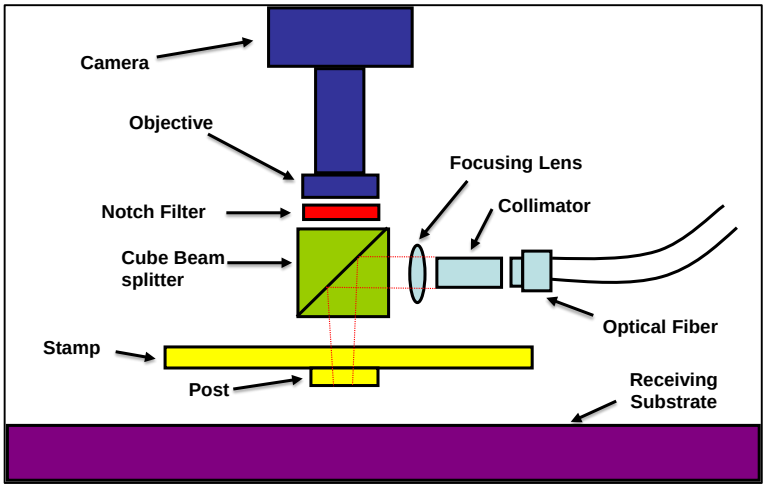

Figure 78: Schematic of the transfer printing stamp holder with integrated high power laser.

Using a laser beam with the appropriate wavelength, focused energy can be transferred into the silicon through absorption causing it to heat up. By controlling the incident laser power the temperature of the silicon/polymer interface can be modulated.

To achieve laser based localized heating, a custom transfer printing tool head is used that allows for the integration of a laser light source into the stamp holder. Figure 78 shows the schematic of the custom tool head. The main components of the system are a Camera with its illumination source used for alignment and optical feedback. A fiber optic cable with a 4mm collimator and focusing lens with a 51 mm focal distance bring in the laser radiation. A beam splitter is used to align the optical path of the laser with the camera. A notch filer is applied to filter out the laser wavelength to allow observation through the camera by limiting overexposure. The laser used in this setup is an 805nm 30W electronically pulsed diode laser. The laser is focused to a 600µm-700µm diameter spot at the PDMS post face. Figure 79 shows the image of the tool head with the camera and laser along with its optics interfaced onto it. The camera and the optics are mounted on an independent three axis motion stage, this allow for independent motion of the tool head relative to the stamp. This way the laser can be focused at any point on the stamp.

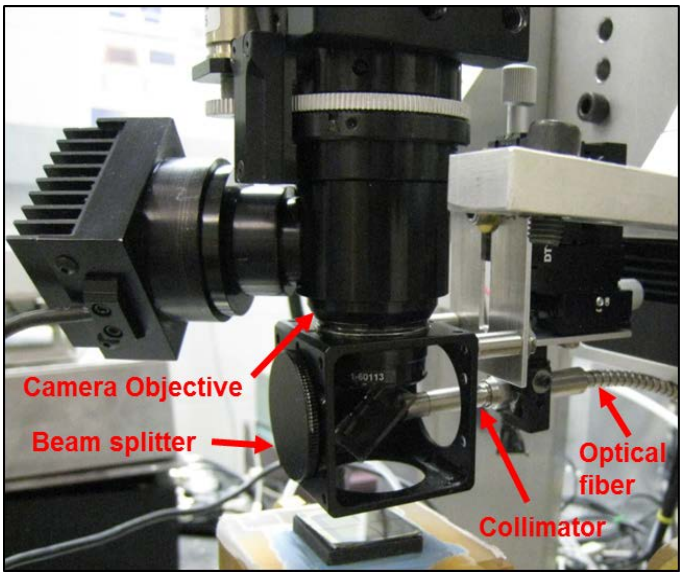

Figure 79: Image of the transfer printer stamp holder with the laser interface and optics.

6.1.2 Simulating localized heating

To bond effectively, the silicon area that needs to be bonded to the polymer needs to be heated to a sufficiently high temperature; causing the polymer at the interface to heat up beyond its glass transition temperature and reflow, allowing the interface to bond. To assess the feasibility of this process a FEA based simulation of the temperature of silicon under laser based heating was done.

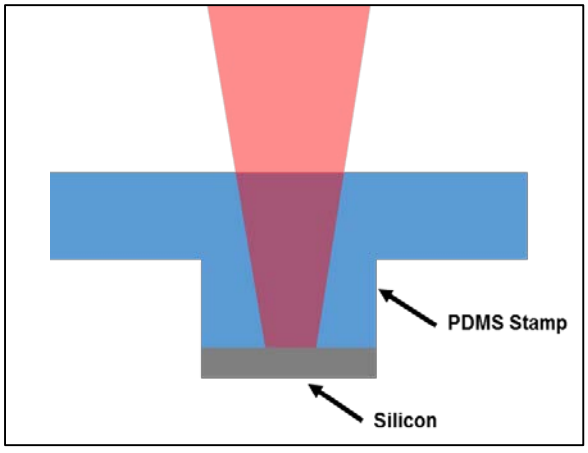

Figure 80: A schematic representation of the FEA model used to calculate the effect of laser based localized heating on silicon piece attached to a PDMS

The FEA model consists of a 250 µm wide silicon piece attached to PDMS on one side. The silicon is assumed to be in air for the purpose of the simulation. The laser is incident onto the silicon through the PDMS. To calculate the temperature of the silicon, an incident laser power of 5W was chosen, the spot size diameter is assumed to be 600 µm. Assuming uniform flux, the incident laser power per unit area is 1.76E7 W/m^2. For the purpose of simplifying the simulation the laser power is assumed to be absorbed at the surface of the silicon at the silicon/PDMS interface. Figure 80 shows a schematic of the model.

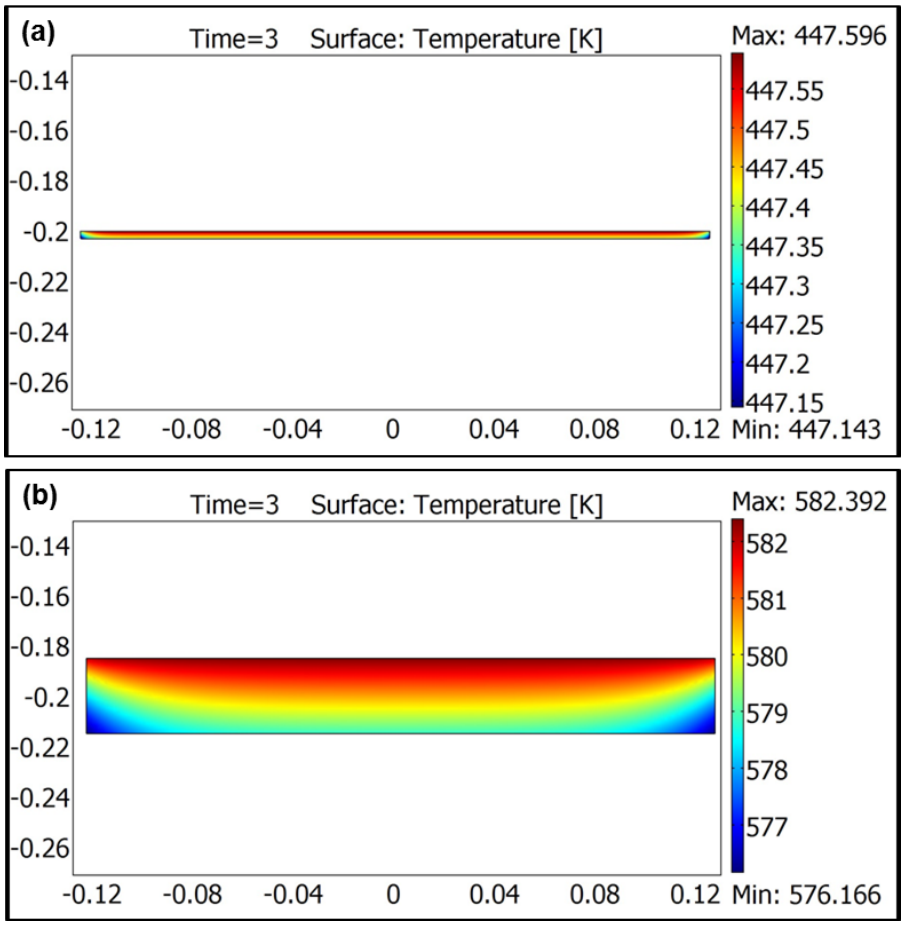

Figure 81: FEA simulation results showing the temperature of the silicon attached to the PDMS stamp. (a) Temperature of a 3 µm thick silicon piece after being irradiated by the laser pulse for 3 msec.(b) Temperature of a 30 µm thick silicon piece after the same laser exposure.

Two different thicknesses of silicon were simulated, 3 μm and 30 μm. The reflectivity value for the PDMS/Silicon interface is takes to be 18%. The light absorption strongly depends on the thickness of the silicon, for the 3 μm silicon a 30% absorption rate is used, for the 30 μm silicon an absorption rate of 95% is used. Using the above values the amount of power per unit area absorbed by the 3 μm and 30 μm silicon is 4.33E6 w/m^2 and 1.37E7 W/m^2 respectively. The laser pulse is applied for a total time of 3 msec. The heat loss to the ambient air is taken to be 50 W/m^2K.

The results of the FEA simulation are shown in figure 81. The FEA results suggest that under the chosen conditions the temperature rise in the silicon is sufficiently large to heat up the Silicon polymer interface beyond its glass transition temperature. The FEA results predict a temperature rise up to 175 ^oC and 300 ^oC for the 3 μm and 30 μm thick silicon respectively. The FEA results show that the temperature achieved is large enough to heat the interface up to and beyond the glass transition temperature of the SU-8 polymer. Thus the process of melting the polymer locally at the silicon/polymer interface using laser irradiation is potentially viable.

6.1.3 Experimental demonstration

To test and demonstrate the process a set of experiments were conducted. Silicon beams were fabricated with thicknesses of 3 μm and 30 μm. Two types of beams are fabricated. The beams are 3 mm long. The silicon beams were fabricated using an SOI wafer. The image of one of the donor wafers with the beams is shown in figure 82. These beams are used to demonstrate the assembly and in-situ bonding process.

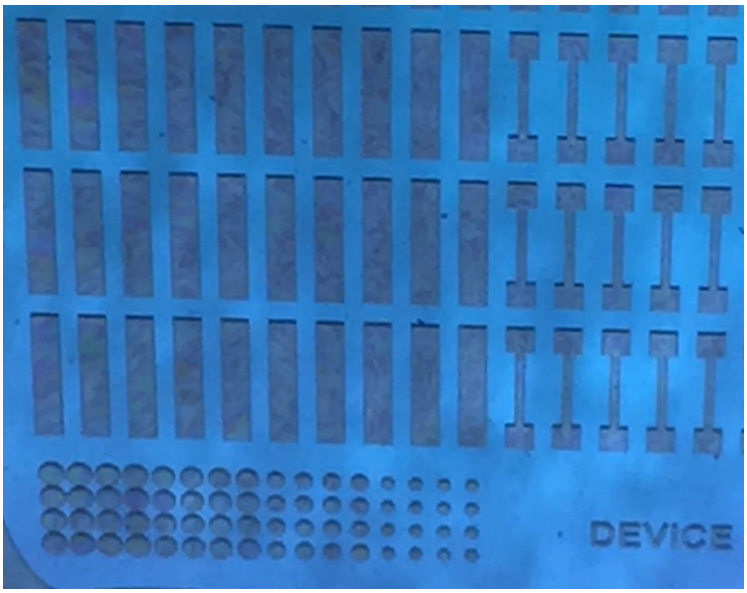

Figure 82: Image showing the silicon beams fabricated to test the integrated assembly and bonding process. The different beam shapes have been fabricated.

A target substrate consisting of an array of SU-8 columns was fabricated. The silicon beams would be picked up from their donor substrates and bonded to the SU-8 columns. The SU-8 columns are fabricated on a silicon substrate using standard photolithography techniques. The SU-8 pillars are 600 µm x 600 µm, 150 µm tall. Figure 83 shows the image of the SU-8 columns fabricated onto the silicon substrate

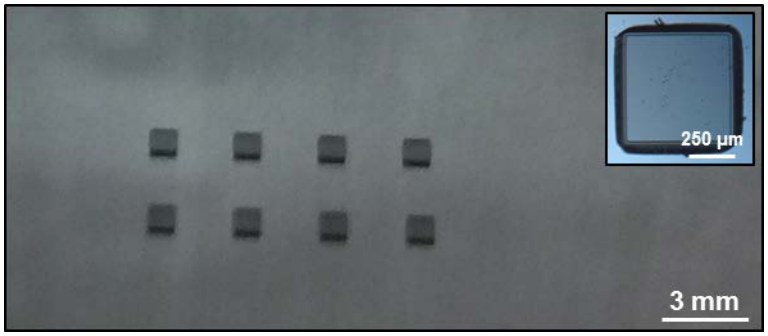

Figure 83: Image of an array of SU-8 columns fabricated onto a silicon wafer. The insert shows the top view of a single column captured using a microscope.

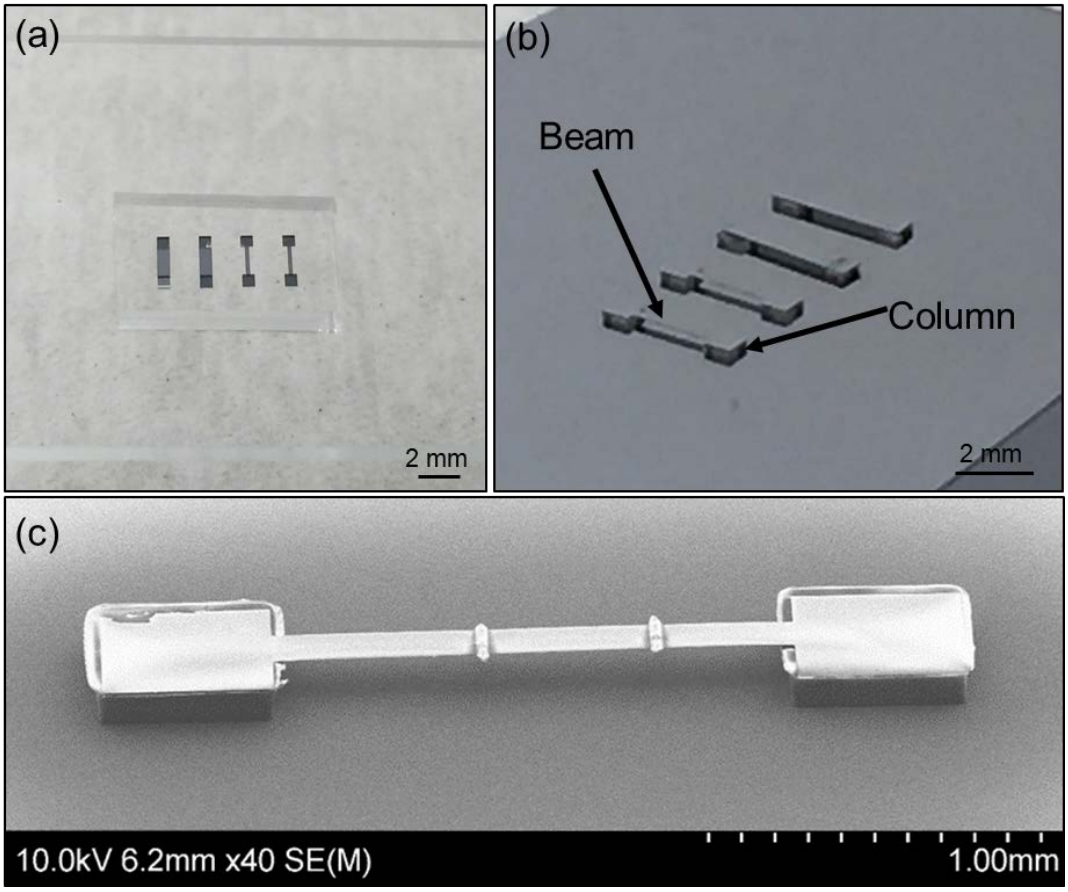

Figure 84: Image of silicon beam manipulation and assembly. (a) Image of four beams picked up from a donor wafer attached to a PDMS stamp. (b) Image of the beams attached ontoSU-8 columns. (c) SEM image of a 3 µm thick, 3mm long suspended silicon beam assembled using the process.

After fabrication, the donor substrate with the beams and the acceptor substrate with the columns were mounted onto the transfer printer. Using a PDMS stamp four beams were picked up from the donor. The beams were aligned to the columns and using short laser pulses the ends of the beam were heated to bond the silicon and the SU-8 together. The least incident laser energy required and pulse time required to bond the beams was experimentally determined. The incident laser energy was determined to be 1.23E7 W/m^2 and the pulse time was 10 msec for 3 µm thick beams and 50 msec for the 30 µm thick beams. The increased pulse times can be attributed to greater heat loss in the actual system, thus requiring more energy to heat up the silicon/SU-8 interface to reach the desired temperature. Figure 84 (a) shows an image of four beams picked up

and attached to a PDMS post. Figure 84 (b) shows an array of 30 µm thick beams assembled and bonded onto the SU-8 columns. Figure 84 (c) shows a scanning electron microscope image of a 3 µm thick beam bonded onto SU-8 columns. The heating processes causes the Silicon/SU-8 interface to heat up and reflow. To check this, a set of silicon beams were removed using mechanical force from their bonded columns. Using SEM imaging the shape of the SU-8 column was studied. The SEM analysis shows that the region of SU-8 in the immediate vicinity of the silicon/SU-8 interface goes through a reflow process when heated. Under the application of pressure and heating a slight mushrooming of the interface takes place as shown in the SEM images of figure 85.

One application area where this process can be employed is the manufacturing of out of plane, three dimensional MEMS. Individual planar structures can be assembled to form three dimensional devices using micro transfer printing based assembly and in-situ bonding. To experimentally verify that the process can be implemented using such structures, a test donor and acceptor substrate were created. The acceptor substrate was patterned with features to represent a mockup of a planar MEMS device structure. 50 µm tall features emulating a planar MEMS

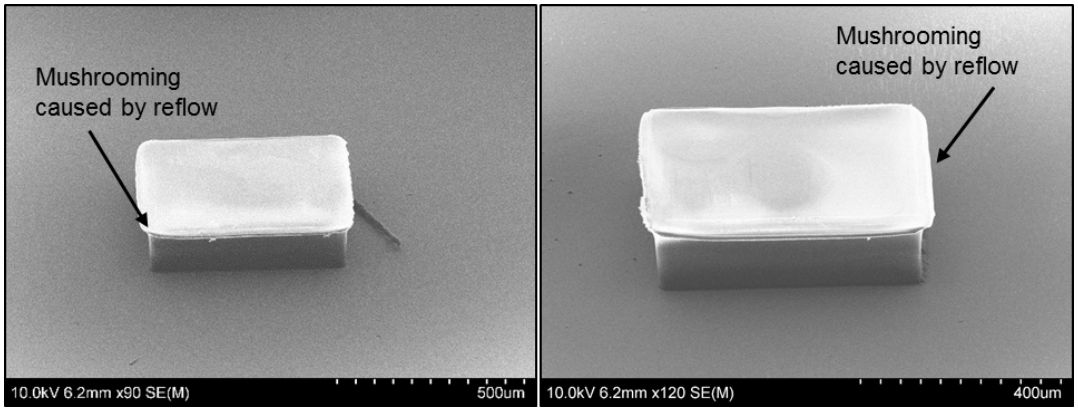

Figure 85: SEM images of two SU-8 columns with their beams removed after the assembly and bonding process. The top of the columns show a slight mushrooming effect from SU-8 reflow caused by the application of pressure and heat.

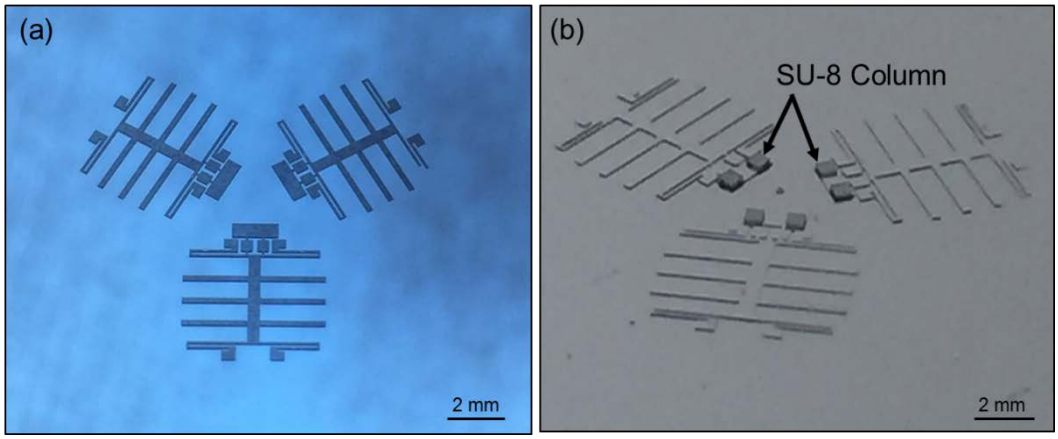

Figure 86: Image of an acceptor substrate with features patterned onto in to represent a MEMS planar actuator structure. (a) Image of the acceptor substrate after formation of the structure after DRIE process. (b) Image of the acceptor substrate after patterning of the SU-8 columns to which an end effector would be bonded.

actuator were etched onto a silicon acceptor substrate using DRIE. An array of 150 µm tall SU-8 columns were patterned using photolithography on top of the structure. These columns would serve as locations where an end effector would be bonded later using the assembly and bonding process. The acceptor substrate with its patterned features and SU-8 bonding columns is shown in figure 86.

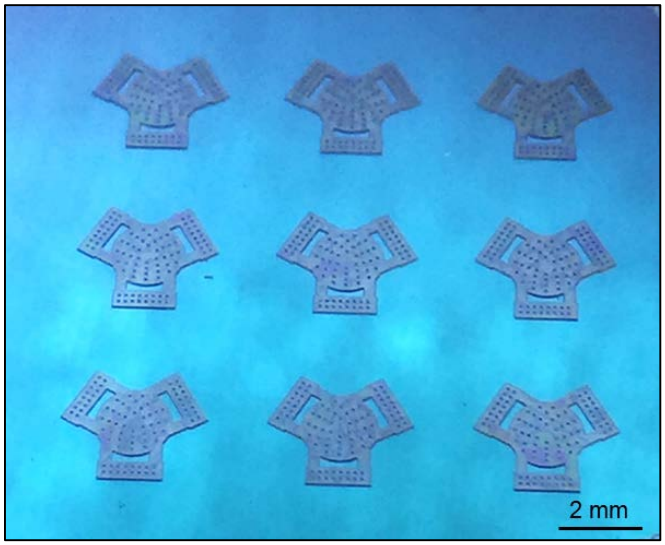

Figure 87: Image of the donor wafer with silicon structures fabricated to represent an end effector to be assembled onto a MEMS stage.

A donor wafer with 30 µm thick silicon structures was fabricated using DRIE on an SOI wafer. The silicon structures were representative of a simulated end effector that would be bonded onto the acceptor substrate prepared earlier. Figure 87 shows an image of the donor wafer prepared with an array of 9 structures representing an end effector to be assembled.

Using the micro transfer printer the end effector structure was picked up from the donor substrate using a PDMS stamp. Figure 88 (a) shows the image of the simulated end effector attached onto the PDMS stamp. After retrieval of the end effector it was aligned to the SU-8 columns on the acceptor substrate structure. Using laser pulses the end effector structure was bonded to each of the six SU-8 columns. The image of the completed structure is shown in Figure 88 (b) and an SEM image of the same structure is shown in figure 88 (c). The end effector structure can be clearly seen suspended and bonded to the SU-8 columns.

These pilot experiments proved that micro transfer printing based assembly and in-situ bonding can be used effectively to create three dimensional silicon/polymer hybrid microstructures. Using test structures we experimentally determined that the process can successfully bond silicon and SU-8 structures. Millimeter scale suspended silicon structures were

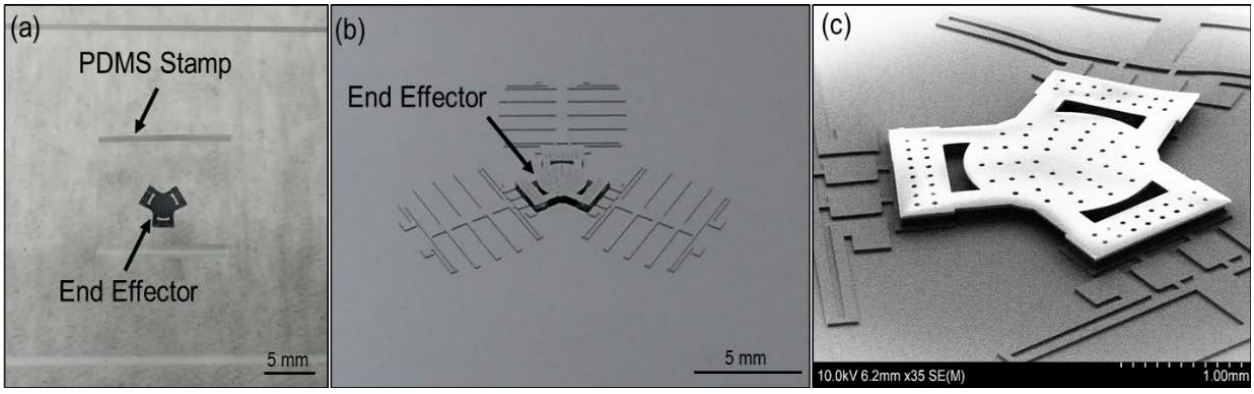

Figure 88: Image of a representative three dimensional out of place MEMS structure fabricated using planar units using the micro transfer printing based assembly and bonding process. (a) Image of the representative end effector structure attached to a PDMS stamp after retrieval from the donor substrate. (b) Image of the fully assembly structure with a fully suspended out of plane end effector. (c) SEM image of the representative MEMS structure.

fabricated using the process with different silicon thickness. Specially patterned acceptor and donor substrates were created to simulate MEMS structures. A representative silicon end effector was successfully assembled and bonded onto a mock MEMS planar stage structure. These experiments helped define the bonding process protocols that can be used as the starting point for more detailed studies in the future.

6.1.4 Application of active composite stamps

This pilot study was conducted using a bulk PDMS stamp, however the process mechanics do not prohibit the use of active composite stamps for the process. The active composite stamps are designed to have a clear optical path behind each post. Cross linked SU-8 does not show any significant absorption for light beyond a wavelength of 400 nm [64]. Thus the active composite material will not offer any significant absorption of the laser energy used to heat and bond the silicon/SU-8 interface and will not deteriorate the process. The active composite stamps offer a significant advantage over a bulk stamp in this application area. With the ability to sense contact the process can adjust for local variations in the acceptor substrate geometry. For the test structures used in this study, a 5% variation in the height of the SU-8 columns would result in a height difference of 7.5 μm. The ability to sense coupled with local actuation can allow for the compensation of such errors. Moreover with the ability to control contact force, uniform pressure can be applied to each SU-8 column thus ensuring that the bonding is uniform.

6.2 Transfer printing of Silicon Fabric

Development of flexible electronics is a promising new area that is likely to broaden the application of both digital and analog electronics. Conventional flexible and/or organic electronics are built using polymeric or plastic materials as the substrate [65]. These materials are unattractive

from a performance and functionality point of view with slow transport characteristics, low thermal budgets and limited lithographic resolution [66]. The performance problems associated with organic materials for flexible electronics can be remedied by using devices made from unconventional substrates such as silicon-on-insulator (SOI), silicon (111) and ultra-thin body SOI; however these substrates tend to be expensive.

One method recently developed by Jhonathan *et al* [67] can be used to convert low cost conventional bulk silicon substrates into thin and flexible formats. Their method provides a cost effective approach without sacrificing performance. The process begins by fabricating devices on top of a bulk silicon (100) wafer following standard very large scale integration (VLSI) processes. After active device fabrication an insulator layer is grown on the surface. Following insulator growth, using deep reactive ion etching (DRIE), holes are etched in the inactive regions of the surface going into the bulk silicon. The sidewall of the etched holes are passivated using an oxide. Finally using XeF_2 the bulk silicon is isotropically etched creating voids within the bulk silicon. This etching processes detached the top surface of the silicon wafer from the bulk. This leaves a thin silicon film on the top with the active devices which can be removed later. A simplified schematic of the process is shown in figure 89.

The advantage of the silicon fabric process is that it allows for the manufacturing of thin flexible silicon substrates using low cost bulk silicon (100) wafers offering all the performance advantages and is compatible with standard VLSI techniques.

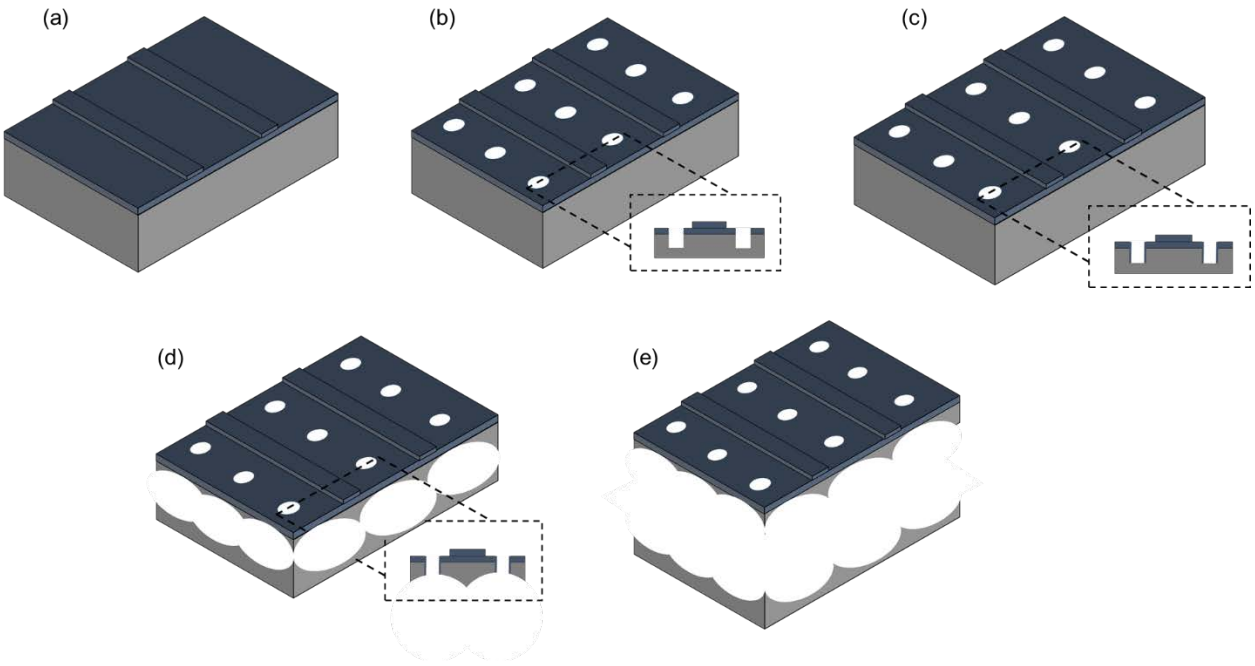

Figure 89: Schematic of silicon fabric fabrication process. (a) Formation of active devices and growth of dielectric layer. (b) Patterning and etching of holes in the inactive region going into the bulk silicon. (c) Passivation of the hold sidewalls. (d) Isotropic etching of the bulk silicon underneath the device layer using XeF_2. (e) Release of the thin silicon fabric substrate from the bulk silicon wafer.

6.2.1 Experimental results

The goal of this pilot study is to utilize micro transfer printing for retrieval and assembly of silicon fabric with active devices onto nonnative substrates. This work was done in collaboration with the Integrated Nanotechnology Laboratory at King Abdullah University of Science and Technology (KAUST), Saudi Arabia. The silicon fabric substrates with active devices were prepared at KAUST and brought to Ferreira Researcg Group at UIUC. The acceptor substrates along with the processing techniques to perform micro transfer printing were developed at UIUC. Two acceptor substrates were used for testing the assembly process, glass and polyimide. One of the most challenging aspect of this study was to achieve successful release of the silicon fabric after retrieval. Due to the highly structured nature of the bottom surface owing to the unique fabrication process, during release the total contact area between the bottom surface and the

receiving substrate is very small. To cater for this, we developed a process that relies on a thin adhesive layer to promote the adhesion between the silicon fabric and the receiving substrate. Even with the use of adhesive we experimentally determined that the contact area between the stamp and silicon fabric should be no greater than 1% of the silicon fabric area for successful release. A thin layer of spin coated polyimide was used as the adhesive layer to promote the release of the silicon fabric and its eventual bonding to the acceptor substrate.

For the first experiment a set of silicon fabric substrates with CMOS transistor arrays patterned onto them were retrieved from their native bulk silicon substrate and transferred onto a glass substrate. The glass substrate is first coated with a thin layer of polyimide. The polyimide is

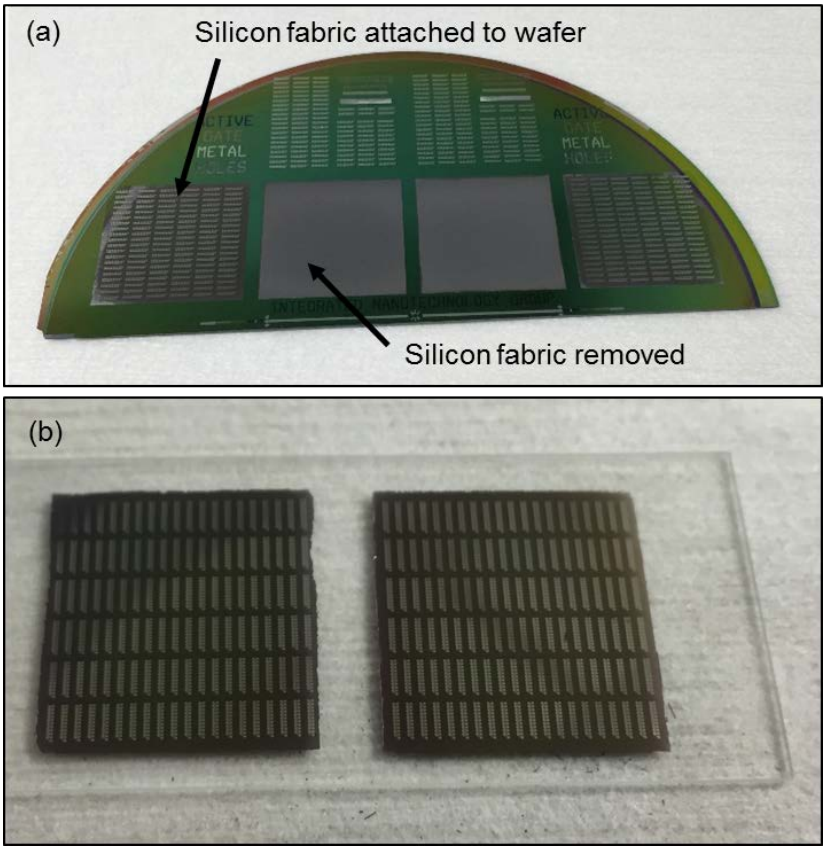

Figure 90: Image of transfer printing of silicon fabric substrates. (a) Image of the donor substrate after remoal of two silicon fabric substrates. (b) Image of the silicon fabric substrates bonded onto a glass substrate following transfer printing.

spin coated onto the glass substrate at a speed of 5000 rpm for 60 sec. After spin coating the polyimide is soft baked at a temperature of 65^{o}C for 5 minutes to remove the solvents while still retaining its adhesive properties.. After preparation of the acceptor substrate, the donor and acceptor substrates were mounted onto the transfer printer and the silicon fabric was transfer printed onto the glass acceptor substrate. After transfer printing the glass substrate is cured at a temperature of 130 ^{o}C for 30 minutes. The image of the donor and acceptor substrate after the transfer printing is shown in figure 90. Figure 90 (a) shows the image of the donor substrate after transfer printing of two of the silicon fabric regions. Figure 90 (b) shows the image of silicon fabric with active transistors transferred and bonded onto a glass substrate. After the transfer printing the sample were sent back to KAUST for measurement and analysis.

The second experiment was to demonstrate wafer level transfer of the silicon fabric onto a flexible substrate. The donor substrate consisted for a 4" wafer with a single silicon fabric substrate patterned on top of it. For the acceptor substrate a 100 µm thick polyimide film was first adhered onto a four inch wafer. After the polyimide film was attached to the wafer, a thin layer of polyimide was spun coated onto the polyimide film using the process described previously. To perform transfer printing first the donor substrate was mounted onto the machine tool and the silicon fabric was retrieved. The image of the silicon fabric wafer mounted onto the transfer printing tool is shown in figure 91(a). Figure 91 (b) shows the image of the wafer scale silicon fabric retrieved from the donor wafer using a PDMS stamp. Afterwards the native bulk silicon substrate was replaced by the acceptor substrate and the silicon fabric was brought into contact and released onto the acceptor substrate. Figure 91 (c) shows the image of the wafer scale silicon fabric being

released onto the polyimide substrate. After transfer printing the polyimide adhesion layer was cured and the polyimide film along with the transferred silicon fabric was peeled off of the temporary mounting wafer. The final polyimide layer with the silicon fabric is shown in figure 91 (d).

These pilot experiments have proven that micro transfer printing is an efficient process to perform manipulation and assembly of silicon fabric substrates of various sizes onto a variety of substrates. Successful transfer of centimeter scale substrates to wafer scale substrates of silicon fabric was conducted using transfer printing. Two different acceptor substrates (glass and

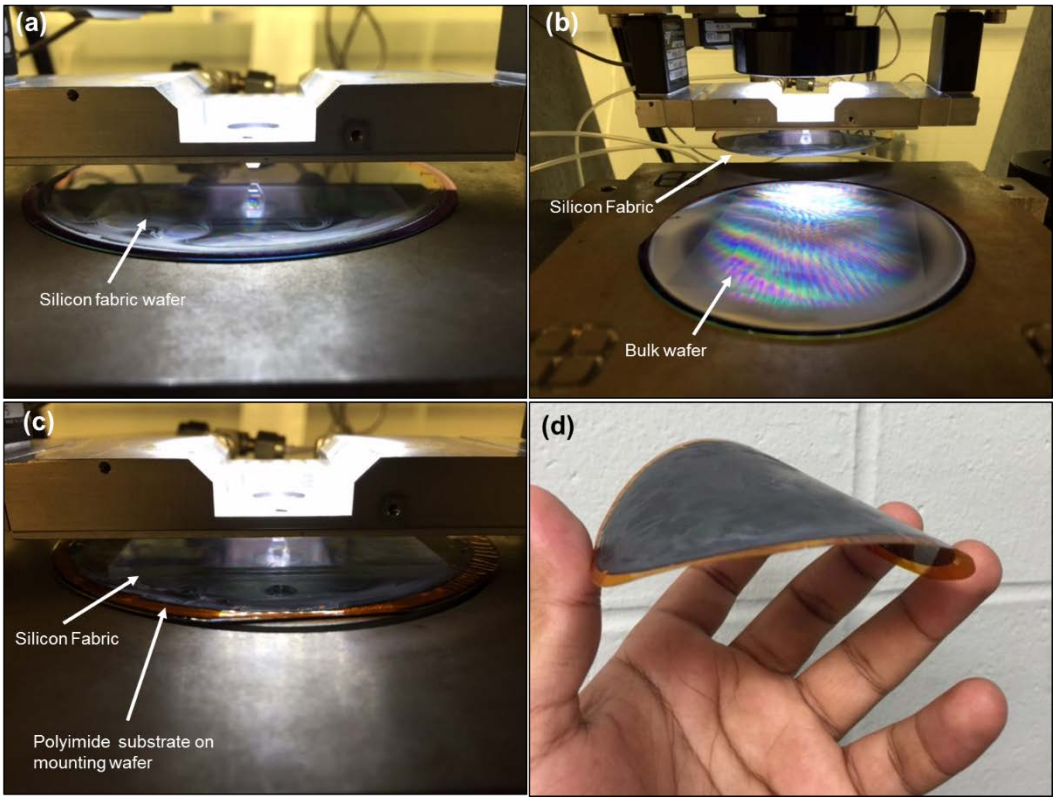

Figure 91: Images captured during transfer printing of wafer scale silicon fabric. (a) Image of the silicon fabric donor wafer mounted onto the transfer printing tool. (b) Image showing the wafer scale silicon fabric picked up using a PDMS substrate and the silicon bulk wafer. (c) Image of the acceptor substrate mounted onto the transfer printing tool and silicon fabric being printed onto it. (d) Image of the polyimide substrate with the wafer scale silicon fabric bonded onto it after removal of the polyimide substrate from the mounting wafer.

polyimide) were used and successful transfer printing based assembly of silicon fabric on both substrates was shown. The use of transfer printing for silicon fabric assembly and integration is a very promising area for realizing the potential of transfer printing in manipulating ultra-thin substrates to perform heterogeneous integration and can open many potential application areas utilizing silicon fabric based heterogeneously integrated systems.

6.2.2 Application of active composite stamps

This pilot study used a bulk PDMS stamp to perform transfer printing however the process is easily transferrable to the active composite stamp since it emulates a bulk stamp very closely. The requirement of controlling the area of contact between the stamp and the silicon fabric is more favorable toward the uses of the active composite stamps. Being able to selectively engage individual posts to the silicon fabric during retrieval allows to control the contact area between the stamp and the silicon fabric. This has the potential to allow the use of a single active composite stamp for a large variety of silicon fabric sizes.

CHAPTER 7: CONCLUSION

This thesis presented the advancement of the micro transfer printing process through the integration of novel functionality into the micro transfer printing stamp. First by analyzing the operation of the stamp within the process, areas of opportunities were identified that can enhance the performance of the process. Functional requirements for the stamp were determined to meet some of the opportunities identified for advancing the micro transfer printing process. These included the integration of sensing to detect important process events and methods to perform in-situ process monitoring and the need for modulating stamp geometry. Modulation of the stamp geometry was identified as the mechanism to aid in selective device retrieval and release as well as transition from a pick and place process to a collect and place process.

Starting with the concept of a novel active composite material composed of multiple functional layers a stamp architecture was developed. The active composite material allowed the integration and distribution of functions such as sensing, actuation and compliance tuning. The active composite materials provides a facile means of adding distributed sensing, actuation and compliance tuning to a material using standard microfabrication techniques. This versatile material can find many potential application in areas such a tactile sensors, micro fluidics, micro scale probing, etc. To demonstrate a device composed of the active composite material a generic stamp architecture was introduced. The local compliance tuning replaced the compliance of the PDMS in a bulk stamp. This resulted in a system that from a process point of view is very similar to a bulk PDMS stamp but contains additional functionality supported by the active composite material.

After a general architecture of the active composite stamps was developed, finite element analysis based design of the stamps was presented. Following the design process a facile and scalable fabrication process employing traditional microfabrication in conjunction with micro transfer printing was developed to manufacture the newly designed stamps. Following manufacturing the stamps were integrated into the micro transfer printing process using custom instrumentation and software. The integrated stamps were characterized and their performance was compared to design goals, good agreement was observed between the design and the actual stamp performance.

Using the sensing functionality the ability of the stamps to successfully detect important process events was demonstrated. Using event detection the process was reprogrammed in which instead of using stage position, event detection was used to control the process. Successful transfer printing operation was shown using the event driven process. Finally a demonstration of in-situ process monitoring was made. Using the sensory feedback the force measured during the retrieval and release of individual inks was measured. The measured force was then used to detect success and failure of ink retrieval and release using a statistical discriminant function. A classification rate of greater than 99% was experimentally observed for successful ink retrieval and release.

After demonstrating the advantage of sensory feedback from the stamp, process enhancements from stamp geometry modulation through the added actuation functionality were experimentally exhibited. The active composite material based stamps had two actuation modes. The first actuation mode was based on piezoelectric actuation where the integrated piezoelectric layer provided the actuation force. This mode allowed for a 6 μm deflection of the stamp post. Using stamp geometry manipulation selective transfer printing was demonstrated. Finally closed

loop control of position and contact force for the individual stamp posts was shown. Good tracking performance was observed in both position and contact force. The stamps were shown to achieve a position resolution of 100 nm and a contact force resolution of 50μN.

After demonstrating the first piezoelectric actuation mode the second actuation of the active composite stamp was experimentally tested. The second actuation mode of the active composite stamp is termed as thermo-mechanical actuation. In this actuation mode the integrated strain gage acts as a resistive heater and the SU-8/PZT bi-material polymer/ceramic composite provides the actuation. This actuation mode was experimentally shown to provide up to 18 μm of motion of the stamp post. System identification experiments was performed to determine a model for the system. Following system identification a closed loop control system was designed. Closed loop control was implemented to control the motion of the stamp posts. Good tracking performance was experimentally observed. After closed loop control, new transfer printing modes such as collect and place, and selective printing were successfully implemented.

Finally a set of pilot experiments were done to explore new application areas for the micro transfer printing process. The first area that was explored was to use micro transfer printing to perform three dimensional out of plane MEMS assembly. The concept behind the process was to use localized heating to bond silicon and polymer structural elements together. The local heating was to be provided by localized absorption of laser light by silicon. For this purpose a specially designed transfer printing tool head was used. The tool head integrated a laser, fiber optic cable, optics for visual feedback and three axis stage. Using this method test structures composed of silicon beams of different thicknesses were bonded onto SU-8 columns. Finally to demonstrate three dimensional MEMS assembly a mockup of a MEMS translation stage was fabricated onto a

silicon wafer. An array of SU-8 structural columns were fabricated on the simulated MEMS structure. Finally a mock end effector, fabricated on an SOI wafer, was assembled and bonded onto the simulated MEMS stage to demonstrate the assembly process. The second set of exploratory studies were done to assess the feasibility of using micro transfer printing for heterogeneous integration using silicon fabrics. This work was done in collaboration with the Integrated Nanotechnology Laboratory at King Abdullah University of Science and Technology (KAUST), Saudi Arabia. The silicon fabric donor substrates were prepared at KAUST and transported to UIUC. The process to using transfer printing for integrating the silicon fabric onto nonnative substrates was developed at UIUC. Using transfer printing die scale and wafer scale silicon fabric substrates were successfully transfer printed onto glass and polymer substrates.

The functionality introduced in this work and the new modes of transfer printing shown as a result of the functional integration can help make micro transfer printing a very robust and flexible process. Further development with regards to improving error detection capabilities and making large area active composite stamps can make micro transfer printing really potent. Moreover the generic architecture of the active composite material along with the scalable manufacturing processes presented can allow the creation of many novel heterogeneously integration microelectromechanical system with usage in fields well beyond micro transfer printing.

BIBLIOGRAPHY

[1] A. N. Das, R. Murthy, D. O. Popa and H. E. Stephenou, "A Multiscale Assembly and Packaging System for Manufacturing of Complex Micro-Nano Devices," *IEEE Transactions on Automation Science and Engineering,* vol. 9, no. 1, pp. 160-170, 2012.

[2] K. F. Böhringer, R. S. Fearing and K. Y. Goldberg, "Microassembly," in *Handbook of Industrial Robotics,* vol. 1, New York, Wiley & Sons, 1999, p. 1045.

[3] P. Estevez, S. Khan, P. Lambert, M. Porta, I. Polat, C. Scherer, M. Tichem, U. Staufer, H. H. Langen and R. M. Schmidt, "A Haptic Tele-operated System for Microassembly," in *Precision Assembly Technologies and Systems,* vol. 315, S. Ratchev, Ed., Berlin, Springer, 2010, pp. 12-30.

[4] Q. Zhou, A. Aurelian, C. del Corral and P. J. Esteban, P. Kallio, B. Chang, H. N. Kiovo"Microassembly Station with Controlled Environment," in *Proc. SPIE 4568, Microrobotics and Microassembly III,* 252, 2001.

[5] E. D. Kunt, K. Cakir and A. Sabanovic, "A workstation for microassembly," in *Mediterranean Conference on Control & Automation*, 2007.

[6] L. Ren, L. Wang, J. K. Mills and D. Sun, "Vision-based 2-D automatic micrograsping using coarse-to-fine grasping strategy," *IEEE Transactions on Industrial Electronics,* vol. 55, no. 9, pp. 3324-3331, 2008.

[7] L. Ren, L. Wang, J. Mills and D. Sun, "2-D Automatic Micrograsping Tasks Performed by Visual Servo Control," in *IEEE International Symposioum on Industrial Electronics,* Vigo, 2007.

[8] L. Wang, L. Ren, J. K. Mills and W. L. Cleghorn, "Automated 3-D Micrograsping Tasks Performed by Vision-Based Control," *IEEE Transaction on Automation Science and Engineering,* vol. 7, no. 3, pp. 417-426, 2010.

[9] J. A. Thompson and R. S. Fearing, "Automating microassembly with ortho-tweezers and force sensing," in *IEEE/RSJ International Conference on Intelligent Robotics and Systems*, Maui, 2001.

[10] Z. Lu, P. C. Y. Chen, A. Ganapathy, G. Zhao, J. Nam, G. Yang, E. Burdet, C. Teo, Q. Meng and W. Lin, "A force-feedback control system for micro-assembly," *Journal of Micromechanics and Microengineering,* vol. 16, no. 9, pp. 1861-1868, 2006.

[11] H. Xie, W. Rong, L. Sun and L. Chen, "A Flexible Microassembly System for Automated Fabrication of MEMS Sensors," in *9th Internation Conference on Control, Automation, Robotics and Vision*, 2006.

[12] D. J. Cappelleri, M. Fatovic and U. Shah, "Caging Micromanipulation for Automated Microassembly," in *IEEE Internatiional Conference on Robotics and Automation*, Shanghai, 2011.

[13] T. Kasaya, H. Miyazaki, S. Saito and T. Sato, "Micro object handling under SEM by vision-based automatic control," in *IEEE International Conference on Robotics and Automation*, Detroit, 1999.

[14] J. Alex, B. Vikramaditya and B. J. Nelson, "A virtual reality teleoperator interface for assembly of hybrid MEMS prototypes," in *ASME Engineering Technical Conference*, Atlanta, 1998.

[15] C. Keller, "Microgrippers with integrated actuator and force sensors," in *Proceedings of the World Automation Congress*, 1998.

[16] J. Cecil and N. Gobinath, "Development of a virtual and physical cell to assemble micro devices," *Robotics and Coumputer-Integrated Manufacturing,* vol. 21, no. 4-5, pp. 431-441, 2005.

[17] J. Feddema, P. Xavier and R. Brown, "Micro-assembly planning with van der Waals force," in *Proceedings of the IEEE International Symposium on Assembly and Task Planning*, 1999.

[18] A. Singh, D. A. Horsley, M. B. Cohn, A. P. Pisano and R. T. Howe, "Batch Transfer of Microstructures using Flip-Chip Solder Bump Bonding," in *Proceedings of International Conference on Solid-State Sensors and Actuators*, 1997.

[19] K. F. Harsh, W. Zhang, V. M. Bright and Y. C. Lee, "Flip-Chip Assembly for Si-Based RF MEMS," in *Twelfth IEEE International Conference on Micro Electro Mechanical Systems*, Orlando, pp273-278, 1999.

[20] H. C. Lin, C. C. Wang and K. Wang, "Deterministic Three-Dimensional Micro-Assembly in Parallel," in *Proceesing of the 2011 6th IEEE International Conference on Nano/Micro Engineered and Molecular Systems,* Kaohsiung, Taiwan, 2011.

[21] H. K. Chu, J. K. Mills and W. L. Cleghorn, "Fabrication of a Microcoil Through Parallel Microassembly," in *2012 IEEE International Conference on Robotics and Automation*, Saint Paul, Minnesota, USA, 2012.

[22] B. Nelson, Y. Zhou and B. Vikramaditya, "Sensor-Based Microassembly of Hybrid MEMS Devices," *IEEE Control Systems*, vol. 18, no. 6, pp. 35-45, 1998.

[23] E. Kuran and M. Tichem, "Magnetic Self-Assembly of Ultra-Thin Chips to Polymer Foils," *IEEE Transactions on Automation Science and Engineering,* vol. 10, no. 3, pp. 536-544, 2013.

[24] E. Kuran, M. Tichem and U. Staufer, "Magnetic force driven self-assembly of ultra-thin chips," in *4th Electronic System-Integration Technology Conference (ESTC)*, 2012.

[25] A. Winkleman, L. McCarty, T. Zhu, D. Weibel, Z. Suo and G. M. Whitesides, "Templated Self-Assembly Over Patterned Electrodes by an Applied Electric Field: Geometric Constraints and Diversity of Materials," *Journal of Microelectromechanical Systems,* vol. 17, no. 4, pp. 900-910, 2008.

[26] S. Stauth and B. Parviz, "Integration of silicon circuit components onto plastic substrates using fluidic self-assembly," in *International Conference on MEMS, NANO and Smart Systems,* 2005.

[27] U. Srinivasan, M. Helmbrecht, C. Rembe, R. Muller and R. Howe, "Fluidic self-assembly of micromirrors onto microactuators using capillary forces," *IEEE Journal of Selected Topics in Quantum Electronics,* vol. 8, no. 1, pp. 4-11, 2002.

[28] A. Carlson, A. M. Bowen, Y. Huang, R. G. Nuzzo and J. A. Rogers, "Transfer Printing Techniques for Material Assembly and Micro/Nanodevice Fabrication," *Advanced Materials,* vol. 24, no. 39, pp. 5284-5318, October 2012.

[29] N. Ahmed, A. Carlson, J. A. Rogers and P. M. Ferreira, "Automated micro-transfer printing with cantileverd stamps," *Journal of Manufacturing Processes,* vol. 14, no. 2, pp. 90-97, 2012.

[30] R. H. Kim, D. H. Kim, J. Xiao, B. H. Kim, S. I. Park, B. Panilaitis, R. Ghaffari, J. Yao, M. Li, Z. Liu, V. Malyarchuk, D. G. Kim, A. P. Le, R. G. Nuzzo, D. L. Kaplan, F. G. Omenetto, Y. Huang, Z. Kang and J. A. Rogers, "Waterproof ALInGaP optoelectrinics on stretchable substrates with applications in biomedicine and robotics," *Nature Materials,* vol. 9, pp. 929-937q, 2010.

[31] F. N. Ishikawa, H. K. Chang, K. Ryu, P. C. Chen, A. Badmaev, L. G. De Arco, G. Shen and C. Zhou, "Transparent Electronics Based on Transfer Printed Alignmed Carbon Nanotubes on Rigid and Flexible Substrates," *ACS Nano,* vol. 3, pp. 73-79, 2009.

[32] C. A. Bower, E. Menard, S. Bonafede, J. W. Hamer and R. S. Cok, "Transfer-Printed Microscale Integrated Cuircuits for High Performance Display Backplanes," *IEEE Transactions on Componenets, Packaging and Manufacturing Technology,* vol. 1, no. 12, pp. 1916-1922, 2011.

[33] K. J. Lee, M. A. Meitl, J. H. Ahn, J. A. Rogers, R. G. Nuzzo, V. Kumar and I. Adesida, "Bendable GaN High Electron Mobility Transistors on Plastic Substrates," *Journal of Applied Physics,* vol. 100, no. 12, p. 124507, 2006.

[34] J. Yoon, A. J. Baca, A. I. Park, P. Elvikis, J. B. Geddes, L. Li, R. H. Kim, J. Xiao, S. Wang, T. H. Kim, M. J. Motala, B. Y. Ahn, E. B. Duoss, J. A. Lewis, R. G. Nuzzo, P. M. Ferreira, Y. Huang, A. Rockett and J. A. and Rogers, "Ultrathin Silicon Solcar Microcells for Semitransparent, Mechanically Flexible Microconcentrator Module Designs," *Nature Materials,* vol. 7, pp. 907-915, 2008.

[35] H. C. Ko, M. P. Stoykovich, J. Song, V. Malyarchuk, W. M. Choi, C. J. Yu, J. B. Geddes, J. Xiao, S. Wang, Y. Huang and J. A. and Rogers, "A Hemispherical Electronic Eye Camera Based on Compressible Silicon Optoelectronics," *Nature,* vol. 454, pp. 748-753, 2008.

[36] B. Furman, E. Menard, A. Gray, M. Meitl, S. Bonafede, D. Kneeburg, K. Ghosal, R. Bukovnik, W. Wagner, J. Gabriel, S. Seel and S. Burroughs, "A high concentration photovoltaic module utilizing micro-transfer printing and surface mount technology," in *35th IEEE Photovoltaic Specialists Conference (PVSC)*, 2010.

[37] X. Feng, M. A. Meitl, A. M. Bowen, Y. Huang, R. G. Nuzzo and J. A. Rogers, "Competing fracutre in kinetically controlled transfer printing," *Langmuir,* vol. 23, pp. 12555-12560, 2007.

[38] E. Menard, K. J. Lee, D.-Y. Khang, R. G. Nuzzo and J. A. Rogers, "A printable form of silicon for high performance thin film transistors on plastic substrates," *Applied Physics Letters* , vol. 84, no. 26, pp. 5398-5400, 2004.

[39] M. A. Meitl, Z. T. Zhu, V. Kumar, K. J. Lee, X. Feng, Y. Huang, I. Adesida, R. G. Nuzzo and J. A. Rogers, "Transfer printing by kinetic control of adhesion to an elastomeric stamp," *Nature Materials,* vol. 5, pp. 33-38, December 2006.

[40] S. Kim, J. Wu, A. Carlson, S. H. Jin, A. Kovalsky, P. Glass, Z. Liu, N. Ahmed, S. L. Elgan, W. Chen, P. M. Ferreira, M. Sitti, Y. Huang and J. A. Rogers, "Microstructured elastimeric surfaces with reversible adhesion and examples of their use in deterministic assembly by transfer printing," *Proceedings of the National Academy of Sciences,* vol. 107, no. 40, pp. 17095-17100, 2010.

[41] J. Wu, S. Kim, W. Chen, A. Carlson, K. C. Hwang, Y. Huang and J. A. Rogers, "Mechanics of reversible adhesion," *Soft Matter,* vol. 7, no. 18, pp. 8657-8662, 2011.

[42] A. Carlson, S. Wang, P. Elvikis, P. M. Ferreira, Y. Huang and J. A. Rogers, "Active, Programmable Elastomeric Surfaces with Tunable Adhesion for Deterministic Assembly by Transfer Printing," *Advanced Functional Materials,* vol. 22, pp. 4476-4484, 2012.

[43] J. Eisenhaure, S. I. Rhee, A. Al-okaily, A. Carlson, P. M. Ferreira and S. Kim, "The Use of Shape Memory Polymers for Microassembly by Transfer Printing," *IEEE/ASME Journal of Microelectromechanical Systems Letters,* 2014.

[44] A. Carlson, H. J. K. Lee, J. Wu, P. Elvikis, H. Cheng, A. Kovalsky, S. Elgan, Q. Yu, P. M. Ferreira, Y. Huang, K. T. Turner and J. A. Rogers, "Shear-enhanced adhesiveless transfer printing for use in deterministic materials assembly," *Applied Physics Letters,* vol. 98, no. 26, pp. 264104-3, 2011.

[45] R. Saeidpourazar, M. D. Sangid, J. A. Rogers and P. M. Ferreira, "A prototype printer for laster driven micro-transfer printing," *Journal of Manufacturing Processes,* vol. 14, no. 4, pp. 416-424, 2012.

[46] R. Li, Y. L. Li, J. Song, R. Saeidpouraza, B. Fang, Y. Zhong, P. M. Ferreira, J. A. Rogers and Y. Huang, "Thermo-mechanical modeling of laser-driven non-contact transfer printing: two-dimensional analysis," *Soft Matter,* vol. 8, pp. 7122-7127, 2012.

[47] R. Li, Y. Li, C. Lü, J. Song, R. Saeidpourazar, B. Fang, Y. Zhong, P. M. Ferreira, J. A. Rogers and Y. Huang, "Axisymmetric thermo-mechanical analysis of laser-driven non-contact transfer printing," *International Journal of Fracture,* vol. 176, no. 2, pp. 189-194, 2012.

[48] A. Al-okaily and P. M. Ferreira, "Characterization of Delamination in Laser Micro Transfer Printing," in *ASME 2013 International Mechanical Engineering Congress and Exposition*, San Diego, 2013.

[49] A. Al-okaily and P. M. Ferreira, "Multi-physics modeling for laser micro-transfer printing delamination," *Journal of Manufacturing Processes,* 2014.

[50] K. J. Hsia, Y. Huang, E. Menard, J. Park, W. Zhou, J. A. Rogers and J. M. Fulton, "Collapse of stamps for soft lithography due to interfacial adhesion," *Applioed Physics Letters,* vol. 86, no. 15, p. 1900303, 2005.

[51] Y. Y. Huang, W. Zhou, H. K. J, E. Menard, J. U. Park, J. A. Rogers and A. G. Alleyne, "Stamp collapse in soft lithography," *Langmuir,* vol. 21, no. 17, pp. 8058-8068, 2005.

[52] Z. Zhang, P. Zhao, G. Xiao, B. R. Watts and C. Xu, "Sealing SU-8 microfluidic channels using PDMS," *Biomicrofluidics,* vol. 5, no. 4, pp. 046503-1, 2011.

[53] K. Fukunaga, Introduction to Statistical Pattern Recognition, Academic Press, 1990.

[54] S. J. Gross, Q. Q. Zhang, S. Trolier-McKinstry, S. Tadigadapa and T. N. Jackson, "RF MEMS piezoelectric switch," in *IEEE Device Research Conference*, Salt Lake City, UT, USA, 2003.

[55] S. J. Gross, S. Tadigadapa, T. N. Jackson, S. Troller-McKinstry and Q. Q. Zhang, "Lead-zirconate-titanate-based piezoelectric micromachined switch," *Applied Physics Letters*, vol. 83, no. 1, pp. 174-176, 2003.

[56] Q. Q. Zhang, S. J. Gross, S. Tadigadpa, T. N. Jackson, F. T. Djuth and S. Trolier-McKinstry, "Lead zirconate titanate films for d33 mode cantilever actuators," *Sensors and Actuators A*, vol. 105, pp. 91-97, 2003.

[57] H. Lorenz, M. Despont, N. Fahrni, N. LaBiance, P. Renaud and P. Vettiger, "SU-8: a low-cost negative resist for MEMS," *Journal of Micromechanics and Microengineering*, vol. 7, no. 121, pp. 121-124, 1997.

[58] "Piezo Data: PZT-8," efunda, [Online]. Available: http://www.efunda.com/materials/piezo/material_data/matdata_output.cfm?Material_ID=PZT-8. [Accessed 20 April 2013].

[59] L. Bo, L. Miao and C. Quanfang, "Low-stress ultra thick SU-8 UV photolithography process for MEMS," *Journal of Microlithography, Microfabrication and Microsystems*, vol. 4, no. 4, p. 043008, 2005.

[60] C. Dagdeviren, B. D. Yang, Y. Su, P. L. Tran, P. Joe, E. Anderson, J. Xia, V. Doraiswamy, B. Dehdashti, X. Feng, B. Lu, R. Poston, Z. Khalpey, R. Ghaffari, Y. Huang, M. J. Slepian and J. A. Rogers, "Conformal piezoelectric energy harvesting and storage from motions of the heart, lung, and diaphragm," *Proceedings of the National Academy of Sciences of the United States of America*, vol. 5, pp. 1927-1932, 2014.

[61] N. Ahmed and P. Ferreira, "Transfer Printing with Microfabricated Instrumented Stamps," *7th International Conference on MicroManufacturing*, pp. 354-359, 2012.

[62] Q. M. Wang and E. L. Cross, "Performance analysis of piezoelectric cantilever bending actuators," *Ferroelectrics*, vol. 215, no. 1, pp. 187-213, 1998.

[63] R. Feng and R. J. Farris, "Influence of processing conditions on the thermal and mechanical properties of SU8 negative photoresist coatings," *Journal of Micromechanics and Microengineering*, vol. 13, pp. 80-88, 2003.

[64] O. P. Parida and N. Bhat, " Characterization of optical properties of SU-8 and fabrication of optical components," *International Conference on Optics and Photonics*, 2009.

[65] N. D. Sankir, Flexible Electronics: Materials and Device Fabrication, Blacksburn, Virginia, 2005.

[66] M. Hussain, J. P. Rojas and G. A. S. Sevilla, "Flexible transparent devices from bulk silicon (100)," *SPIE Newsroom*, 18 Novemeber 2013.

[67] J. P. Rojas and M. M. Hussain, "Flexible semi-transparent silicon (100) fabric with high-k/metal gate devices," *Physica status solidi (RRL) - Rapis Research Letters,* vol. 7, no. 3, pp. 187-191, 2013.

APPENDIX A: DYNAMIC OF THE CANTILEVERED STAMP

Consider the cantilevered stamp architecture shown in Figure A.1. Let *X1* define the position of the base of the cantilever which is connected rigidly to the stamp holder on the transfer printer. Let *X2* define the position of the post on the stamp. Let *Kc* and *m* represent the stiffness and the mass of the cantilever.

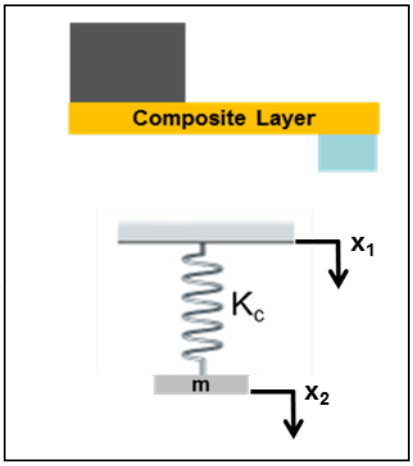

Figure A.1: Schematic illustration of the cantilevered stamp.

The equation of motion of this system is given by,

$$m\ddot{x}_2 = k(x_1 - x_2) \tag{A1.1}$$

Solving through eq. A1.1 we arrive at the post displacement as a function of the stage displacement,

$$m\ddot{x}_2 + kx_2 = kx_1 \tag{A1.2}$$

$$ms^2X_2 + kX_2 = kX_1 \tag{A1.3}$$

$$X_2 = \frac{k}{ms^2 + k}X_1 \tag{A1.4}$$

$$X_2 = \frac{k/m}{s^2 + k/m} X_1 \tag{A1.5}$$

Defining a dummy variable

$$\tau = \sqrt{k/m} \tag{A1.6}$$

We get

$$X_2 = \frac{\tau^2}{s^2 + \tau^2} X_1 \tag{A1.7}$$

Taking the inverse Laplace transform for eq. A1.7 we get

$$x_2 = \tau \sin(\tau t)\, x_1 \tag{A1.8}$$

Taking the derivative we arrive as the velocity of the post as a function of the stage velocity

$$\dot{x_2} = \tau^2 \cos(\tau t)\, \dot{x_1} \tag{A1.9}$$

Or,

$$\dot{x_2} = \frac{k}{m} \cos\left(\sqrt{\frac{k}{m}}\, t\right) \dot{x_1} \tag{A1.10}$$

As can be seen from eq. A.1.10, the delamination velocity at the stamp post has a strong dependence on the stiffness of the stamp. Since during experimentation we have no direct way of measuring the true delamination velocity, the rate dependent adhesion is measured as a function of the stage velocity, i.e. the velocity of the Z-stage of the transfer printer.

From eq. A1.10, if the stamp stiffness decreases the delamination velocity decreases, which in turn effects the adhesion of the PDMS stamp. This explains the reduction of force seen in the rate dependent adhesion effect measurements.

APPENDIX B: TRANSFER PRINTING INK FABRICATION PROCESS

This section presents the basic ink fabrication process used to create ink for micro transfer printing. The typical donor wafer used for making inks for micro transfer printing consists of three layers, namely, a device layer, a sacrificial layer to release devices and a handle layer, the substrate is shown schematically in Figure B.1

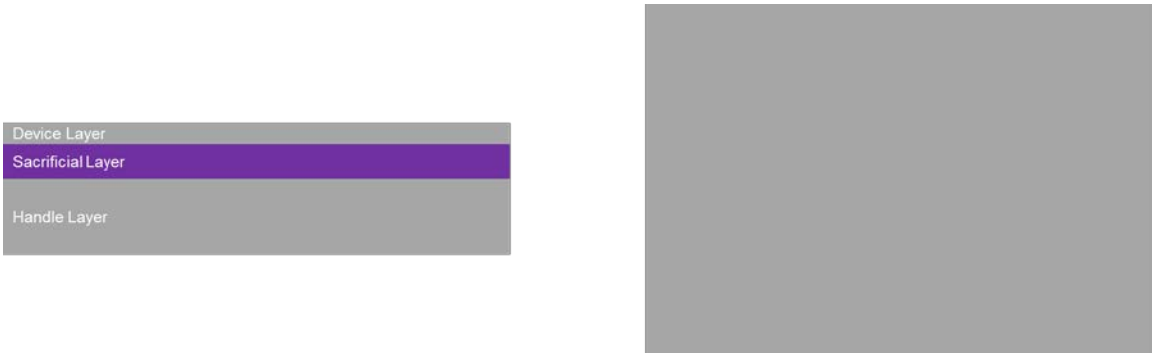

Figure B.1: Schematic representation of a typical donor wafer used for fabricating ink for micro transfer printing.

The typical fabrication process starts by patterning the device layer to form the active devices. The device layer can be composed of a single bulk material or multiple active layers. First using photolithography a photoresist is patterned in the desired device patter as shown in figure B.2.

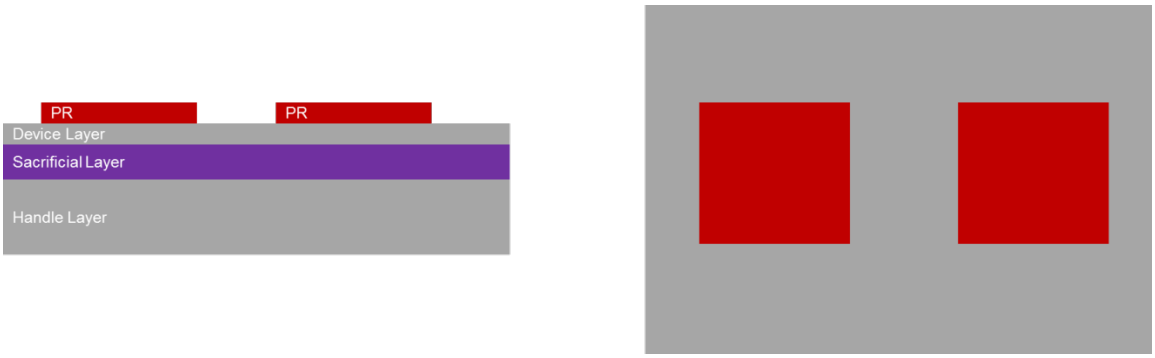

Figure B.2: Defining photoresist pattern on top of the device layer

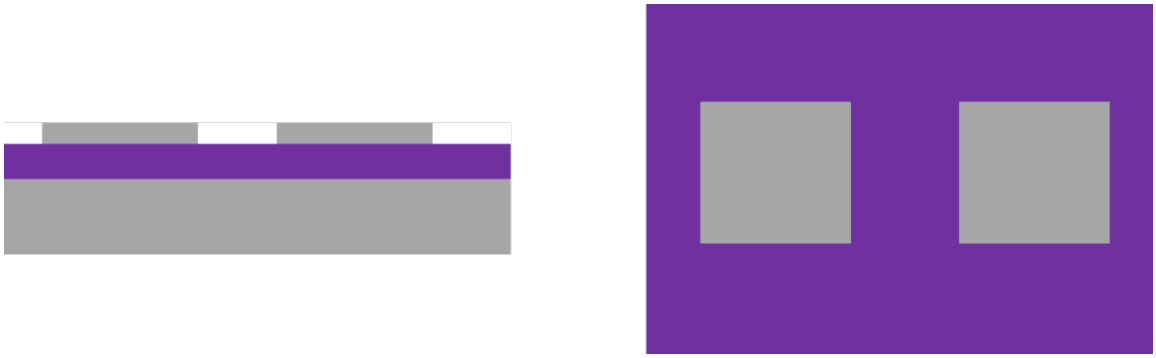

Figure B.3: Etching of the device layer to define the ink structure.

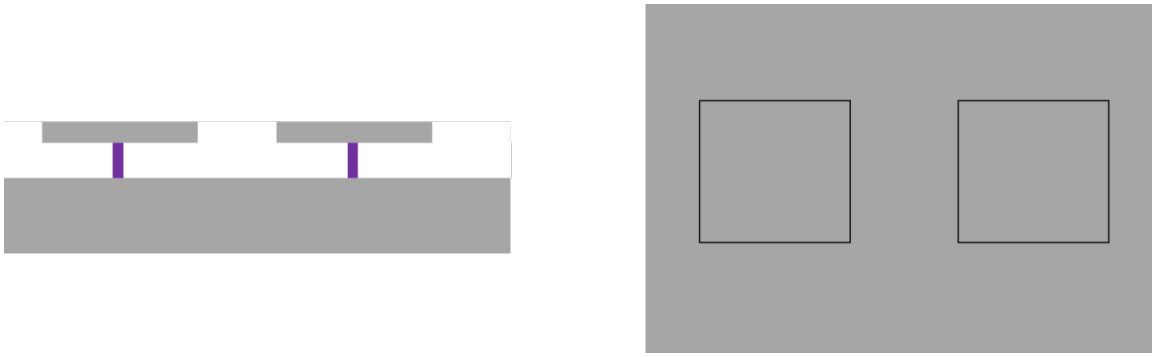

Figure B.4: Fully undercut devices lightly tethered to the donor wafer.

After performing the photolithography to define the device pattern, the device layer is etched using the appropriate etching process to form the ink and the photoresist is stripped away, shown in figure B.3.

After defining the ink, the sacrificial layer is undercut etched using an appropriate etching process to release the devices as shown in figure B.4. The aim of the process is to release the devices while keeping them lightly tethered to the donor wafer to preserve the alignment. Many different schemes exist for anchoring the devices, addressing them is beyond the scope of this work.

APPENDIX C: MATERIAL FOR MICRO-SCALE ACTUATION

Magnetostrictive materials

Magnetostriction is the effect of change in shape of a material when it is subjected to an external magnetic field. The change in shape is caused by rotation and re-orientation of small magnetic domains [1]. Examples of magnetostrictive thin film based micro-actuators include film/substrate bilayer bender actuators most often in cantilever beam arrangements [2]. Common magnetostrictive materials include Ni, amorphous rare earth (Fe,Co) and alloys of iron/gallium generally referred to as Galfenol. State of the art magnetostrictive actuators are often composed of a single rod of an active material surrounded by conductive coils to provide the magnetic field for actuation and are typically centimeter scale. [3] These materials can be easily machined through conventional techniques at the large scale, however their reliable manufacturing at the micro scale is still less developed. Methods for forming thin layers of these materials include DC sputtering and electrochemical disposition [2, 4, 5]. Magnetostrictive materials offer larger energy density compared to ferroelectric materials and ability for remote actuation.

Magnetostrictive materials also can also be used as sensors by using inverse magnetostriction for mechanical as well as magnetic sensing. However the inverse magnetostrictive effect is combined with other effects such as magnetoresistance, magnetoimpedance, etc. Thus their use for sensing requires the consideration of many related secondary effects [2].

One of the most important considerations for active composite material based stamps is selective actuation. The embedded actuators need to be individually addressable for the full potential of the architecture to be realized. To do this with a magnetostrictive material requires the

need for creating highly localized magnetic fields at the scale of an individual actuator. This would entail the creation of coils surrounding the actuators, coupled with unfavorable scaling of magnetic fields at the micro scale. These complexities make the use of a magnetostrictive material as the actuation layer in the active composite stamp difficult. However in application where individually addressable actuation is not a requirement magnetostrictive actuation can be employed.

Shape memory materials

Shape memory materials (SMM) are materials capable of changing their shape upon the application of external stimuli like magnetic field, light, heat, etc. They can be divided into two main groups, namely: metallic shape memory alloys (SMA) and shape memory polymers (SMP).

SMA operation is described by a transformation between two different phases (crystal structures) martensite and austenite phase, based on a change of temperature. Below an established temperature M_f (martensite finished temperature) the SMA is ductile and soft can san be formed into an arbitrary shape easily capable of handling strains greater than 5% [6]. When the SMA in the martensite phase is headed beyond a temperature A_g (austenite start temperature) it begins to transform to the austenite phase, which is finished at a temperature A_f (austenite finish temperature). During the transformation the SMA material becomes hard and returns to the pre-deformed shape. Two of the most commonly used SMA materials for micro scale application are thin films of Ni-Ti and copper alloys. Ni-Ti alloys are attractive for micro scale applications due to their interesting characteristics such as having one of the highest work density at 10 Jcm^{-3} [7]. Physical vapor deposition via sputtering remains the prime manufacturing process for Ni-Ti thin films. One important challenge for their fabrication remains their sensitivity to the composition. For Ni rich Ni-Ti composites, a shift in composition by 1% from the nominal has been shown to

change the transition temperature by 150^{o}C [8]. To fix the pre deformed or "parent shape" the alloy needs to be held into position and heated to about 500^{o}C. The operational frequency for SMA is low due to their high heat capacity and density, thus limiting the heat transfer to and from the material. Rapid heating using large amounts of heat to increase heating rate [9] is possible but without proper monitoring and control this may damage the material. The performance of SMAs is highly dependent upon the surrounding temperature and heat conditions, strain levels in the material along with prior training, cycling and strain history [10].

The second important group of SMM are shape memory polymers (SMP). As in the case of SMA, SMP also exhibit a change in shape under external stimuli which includes thermal [11], magnetic [12], light [13], etc. Due to their relatively easier manufacturing, lower cost and better strain rates SMP are claimed to be superior to SMA [14]. However despite their advantages, SMA are still preferred over SMP in areas that need fast response and high actuation force [6].

Electro-active polymers

Electro active polymers (EAP) are a novel class of materials typically divided into to subclasses: electronic EAP and ionic EAP. Ionic EAP include polymer gels, ionic polymer-metal composites, conjugated polymers and carbon nanotubes [15]. A fundamental requirement of Ionic EAPs is an ionic source typically in the form of an electrolyte solution. Due to this requirement the discussion on EAPs is limited to electronics EAPs.

Electronic EAP comprise of piezoelectric polymers, electrostrictive polymers, dielectric elastomers, liquid crystal elastomers and carbon nanotube aerogels [15]. These materials respond to an applied electric field. Piezoelectric polymers; typically poly(vinylidene fluoride-trifluoroethylene) (PVDF) based electronic EAPs can produce strain up to 5% and have energy

density greater than the best piezoelectric ceramic [16]. They also exhibit piezoelectric behavior when poled and have the potential for use as transduces. In dielectric elastomers a soft polymer dielectric layers between two electrodes is used. Application of voltage across the electrodes squeezes or expands the dielectric film. Typical dielectric materials used include commercially available silicone rubber (PDMS) and acrylic elastomers [17]. Dielectric elastomer based EAPs typically require compliant electrodes to accommodate for the large strains typically ~100% [18]. Electronic EAPs based on liquid crystal elastomers consist of liquid crystal groups attached to each other through a polymer network. The material changes shape by exploiting the reorientation of the liquid crystals in an electric field [19]. The final class of electronic EAPs are CNT aerogels that consist of highly ordered forests of CNT. EAP based actuation represent a promising field of scientific study, although several materials and their properties have recognized for years, limited application have been found. Moreover reliable manufacturing of EAP based actuators and devices at the microscale and thin film fabrication processes are not well established.

Piezoelectric ceramics

Piezoelectric ceramics such as lead zironate titanate (PZT) are of considerable importance in the field of MEMS as sensors and actuators because of their superior piezoelectric, pyroelectric and dielectric properties [20]. Thin films of PZT can be fabricated from a variety of stable microfabrication processes including spin coating of sol-gel, physical vapor deposition techniques [21, 22], chemical methods such as MOCVD [23], etc. These process have been studies extensively and are well understood. In addition PZT based ceramics are available commercialy in a variety of formats from PZT substrates of different shapes and sizes to thin film PZT deposited onto wafers. A variety of diverse applications of PZT thin film transduction exist including

ultrasonic transducers, ultrasonic motors, micropumps, cantilever actuators and uncooled thermal imagers [24, 25, 26, 27, 28]. PZT ceramics offer a lot of advantages for MEMS applications including high efficiency, high energy density, large force, fast response, as well as high sensitivity, low power requirements for sensing applications. They are actuated by using electric fields which makes scaling them easy without the need to special electrode materials.

Some of the disadvantage of PZT ceramics include the strong dependence of their properties on the composition, relatively small strains, high processing temperatures for manufacturing & poling, and polling loss over time (ageing). To address these disadvantages considerable progress has been made. Large deflections can be achieved from PZT actuation by employing amplification mechanisms [29]. The polling loss over time can be accommodated by poling the PZT thin film in-situ [30]. The high fabrication and poling temperature constraint for fabrication onto polymeric substrates can be addressed by fabricating the PZT onto a suitable substrate and then its final assembly onto the polymer later. These solution couples with the advantages of PZT thin films and the breadth of research available for their integration and application into microscale systems makes PZT an excellent candidate material for the active composite material.

Appendix C references

[1] A. Grunwald and A. G. Olabi, "Design of a magnetostrictive (MS) actuator," *Sensor and Actuations A: Physical,* vol. 144, no. 1, pp. 161-175, 2008.

[2] E. Quandt and A. Ludwig, "Magnetostrictive actuation in microsystems," *Sensors and Actuators A,* vol. 81, pp. 275-280, 2000.

[3] H. Steiner, M. Stifter, W. Hortschitz and F. Keplinger, "Planar Magnetostrictive Micromechanical Actuator," *IEEE Transactions on Magnetics,* vol. 51, no. 1, pp. 1-4, 2015.

[4] G. Schiavone, J. Ng, P. Record, X. Shang, K. Wlodarczyk, D. Hand, G. Cummins and M. Desmulliez, "Electrodeposited magnetostrictive Fe-Ga alloys for miniaturised actuators," in *9th International Microsystems, Packaging, Assembly and Circuits Technology Conference* , 2014.

[5] X. Wang, L. Hoffmann, J. Cao, M. Ulmer, M. Graham, J. Savoie and S. Vaynman, "Deflection for a magnetostrictive thin film bimorph in a magnetic field," in *Transactions of the North American Manufacturing Research Institution of SME,* 2012.

[6] J. M. Jani, M. Leary, A. Subic and M. A. Gibson, "A review of shape memory alloy research, applications and opportunities," *Materials & Design,* vol. 56, pp. 1078-1113, 2014.

[7] L. Lederie, "Issues in the design of shape memory alloy actuators," Massachusetts Institute of Technology, 2002.

[8] K. Otsuka and X. Ren, "Physical metallury of Ti-Ni based shape memory alloys," *Progress in Materials Science,* vol. 50, pp. 511-678, 2005.

[9] R. Featherstone and Y. Teh, "Improving the speed of shape memory alloy actuators by faster electrical heating," in *Experimental robotics IX*, Berlin Heidelberg, Springer, 2006, pp. 67-76.

[10] R. G. Gilbertson and J. D. Busch, "A survery of micro-actuator technologies for future spacecraft missions," *The journal of The British Interplanetary Society,* vol. 49, pp. 129-138, 1996.

[11] W. W. Huang, Y. Zhao, C. C. Wang, Z. Ding, H. Purnawali, C. Tang and J. L. Zhang, "Thermo/chemo-responsive shape memory effect in polymers: a sketch of working mechanisms, fundamentals and optimization," *Journal of Polymer Research,* 2012.

[12] R. Mohr, K. Kratz, T. Weigel, M. Lucka-Gabor, M. Moneke and A. Lendlein, "Initiation of shape-memory effect by inductive heating of magnetic nanoparticles in thermoplastic

polymers," *Proceedings of the National Academy of Sciences of the United States of America,* vol. 103, no. 10, 2006.

[13] A. Lendlein, H. Jiang, O. Jünger and R. Langer, "Light-induced shape-memory polymers," *Nature,* Vols. 879-882, p. 434, 2005.

[14] C. Liu, H. Qin and P. T. Mather, "Review of progress in shape-memory polymers," *Journal of Materials Chemistry,* vol. 17, pp. 1543-1558, 2007.

[15] F. Carpi, R. Kornbluh, P. Sommer-Larsen and G. Alici, "Electroactive polymer actuators as artificial muscles: are they ready for bioinspired," *Bioinspiration & Biomimetics,* vol. 6, pp. 1-10, 2011.

[16] Z.-Y. Cheng, V. Bharti, T.-B. Xu, H. Xu, T. Mai and Q. Zhang, "Electrostrictive poly(vinylidene fluoride-trifluoroethylene) copolymers," *Sensors and Actuation A: Physical,* vol. 90, no. 1-2, pp. 138-147, 2001.

[17] R. Kornbluh and R. Pelrine, "High-performance acrylic and silicone elastomers,," in *Dielectric Elastomers as Electromechanical Transducers* , Amsterdam, Elsevier, 2008, pp. 33-42.

[18] S. Rosset and H. R. Shea, "Flexible and stretchable electrodes for dielectric elastomer actuators," *Applied Physics A,* vol. 110, no. 2, pp. 281-307, 2013.

[19] W. Lehmann, H. Skupin, C. Tolksdorf, E. Gebhard, R. Zentel, P. M. Krüger and F. Kremer, "Giant lateral electrostriction in ferroelectric liquid-crystalline elastomers," *Nature,* vol. 410, pp. 447-450, 2001.

[20] C. E. Borroni-Bird, "Smarter vehicles," in *mart Structures and Materials 1997: Industrial and Commercial Applications of Smart Structures Technologies,* San Diego, 1997.

[21] S. Hiboux and P. Murlat, "Piezoelectric and dielectric properties of sputter deposited (111), (100) and random-textured Pb(ZrxTi1-x)O3 (PZT) thin films," *Ferroelectrics,* vol. 224, no. 1, pp. 315-322, 1999.

[22] K. Sreenivas, M. Sayer and P. Garrett, "Properties of D.C. magnetron-sputtered lead zirconate titanate thin films," *Thin Colid Films,* vol. 172, no. 2, pp. 251-267, 1989.

[23] S. L. Swartz, D. A. Seifert, G. T. Noel and T. R. Shrout, "Characterization of MOCVD PbTiO3 thin films," *Ferroelectrics,* vol. 93, no. 1, pp. 37-43, 1989.

[24] P. Murlat and J. Baborowski, "Micromachined Ultrasonic Transducers and Acoustic Sensors Based on Piezoelectric Thin Films," *Journal of Electroceramics,* vol. 12, no. 1, pp. 101-108, 2004.

[25] M. Koch, N. Harris, R. Maas, A. G. R. Evans, N. M. White and A. Brunnschweiler, "A novel micropump design with thick-film piezoelectric actuation," *Measurement Science and Technology,* vol. 8, no. 1, 1997.

[26] Y. Miyahara, T. Fujii, S. Watanabe, A. Tonoli, S. Carabelli, H. Yamada and H. Bleuler, "Lead zirconate titanate cantilever for noncontact atomic force microscopy," *Applied Surface Science,* vol. 140, no. 3-4, pp. 428-431, 1999.

[27] L. Sun, W. Liu, O. Tan and W. Zhu, "Effect of annealing temperature on the sol-gel derived Pb(Zr0.3Ti0.7)O3 thin films for pyroelectric application," *Materials Science and Engineering B: Solid-State Materials for Advanced Technology,* vol. 99, no. 1-3, pp. 173-178, 2003.

[28] P. Muralt, K. M. T. Maeder, A. Kholkin, K. Brooks, N. Setter and R. Luthier, "Fabrication and characterization of PZT thin-film vibrators for micromotors," *Sensors and Actuators: A. Physical,* vol. 48, no. 2, pp. 157-165, 1995.

[29] A. Chigullapalli and J. V. Clark, "Extremely Large Deflection Actuators for Translation or Rotation," in *ASME 2012 International Mechanical Engineering Congress and Exposition,* Houston, 2012.

[30] M. D. Nguyen, E. Houwman, M. Dekkers, H. N. Vu and G. Rijnders, "A Fast Room-Temperature Poling Process of Piezoelectric Pb(Zr0 .45Ti0 .55)O3 Thin Films," *Science of Advanced Materials,* vol. 6, no. 2, pp. 243-251, 2014.